UTS UNIVERSITY OF TECHNOLOGY SYDNEY

Synthesis, Analysis and Development of Three-Port DC/DC Converters

by

Hamzeh Aljarajreh

Thesis submitted in fulfillment of the requirements

for the degree of

Doctor of Philosophy

Faculty of Engineering and Information Technology

School of Electrical and Data Engineering

August, 2021

CERTIFICATE OF ORIGINAL AUTHORSHIP

I, Hamzeh Aljarajreh declare that this thesis, is submitted in fulfillment of the requirements for the award of Doctor of Philosophy, in the School of Electrical and Data Engineering/Faculty of Engineering and Information Technology at the University of Technology Sydney.

This thesis is wholly my own work unless otherwise referenced or acknowledged. In addition, I certify that all information sources and literature used are indicated in the thesis. This document has not been submitted for qualifications at any other academic institution. This research is supported by the Australian Government Research Training Program.

Signature: Production Note:
Signature removed prior to publication.

Date: 07/08/2021

Abstract

The increasing adoption of renewable energy sources such as solar energy, wind energy, and fuel cells has made higher demands on power electronic converters. These converters serve as an electrical interface among various renewable energy sources, energy storage units, and output loads to perform efficient power conversion, effective power conditioning, and fast control whilst complying with the safety and reliability requirements of the system.

Using many single-input, single-output (SISO) converters to connect different sources and loads is a straightforward approach widely adopted in the industry. Although this approach offers apparently easier control and modularity, it leads to relatively complex configuration, high cost, and lower conversion efficiency. Multiple-input, multiple-output converters (MIMO) are capable of converting power from multiple power sources to multiple loads individually or simultaneously by using simplified circuitry and an appropriate control strategy.

The main goal of this thesis is to conduct a systematic topological study to derive all possible basic and non-isolated three-port converters (TPCs), using power flow diagrams that could be used for the future development of DC distribution systems. Unlike most reported TPCs with one bidirectional port, this thesis considers up to two bidirectional ports. It provides an analytical tool and framework for all power flow combinations and corresponding converter configurations, including selection and design. After eliminating the impractical configurations due to indirect connection to some ports and multiple conversion stages, suitable converter configu-

rations are identified and corresponding circuit realizations are demonstrated. The significance of this work is to show which configuration has fewer power conversion stages between any two ports. Furthermore, it shows whether all ports are fully or partially controlled, and it presents the appropriate configuration for specific applications. Three of the investigated configurations are taken as an example to analyse further and verify the principles of operation and working conditions experimentally. The proposed circuits are able to work in seven different modes for a PV-battery-powered DC bus system where smooth and fast transitions between different modes are achieved. Furthermore, a decision flowchart is presented to demonstrate how to select different modes practically.

List of Publications

- **H. Aljarajreh,** D. D. -C. Lu, Y. P. Siwakoti, and C. K. Tse, "A Non-isolated Three-Port DC/DC Converter with Two Bidirectional Ports and Fewer Components," in *IEEE Transactions on Power Electronics.*

- **H. Aljarajreh,** D. D.-C. Lu, Y. P. Siwakoti, C. K. Tse, and K. W. See, "Synthesis and Analysis of Three-Port DC/DC Converters with Two Bidirectional Ports Based on Power Flow Graph Technique," *Energies,* vol. 14, no. 18, p. 5751, Sep. 2021.

- **H. Aljarajreh,** D. D. -C. Lu, Y. P. Siwakoti, R. P. Aguilera and C. K. Tse, "A Method of Seamless Transitions Between Different Operating Modes for Three-Port DC-DC Converters," in *IEEE Access,* vol. 9, pp. 59184-59195, 2021.

- **H. Aljarajreh,** D. D. Lu and C. K. Tse, "Synthesis of Dual-Input Single-Output DC/DC Converters," *2019 IEEE International Symposium on Circuits and Systems (ISCAS),* 2019, pp. 1-5.

- M. R. Al-Soeidat, **H. Aljarajreh,** H. A. Khawaldeh, D. D. -C. Lu and J. Zhu, "A Reconfigurable Three-Port DCDC Converter for Integrated PV-Battery System," in *IEEE Journal of Emerging and Selected Topics in Power Electronics,* vol. 8, no. 4, pp. 3423-3433, Dec. 2020.

Acknowledgments

First of all, I praise God, the almighty, merciful and passionate, for providing me with this opportunity and granting me the capability to proceed successfully. The thesis appears in its current form due to the assistance and guidance of several people. I would like to express my gratitude to:

- My parents, wife and children.
- My supervisor: Prof. Dylan Lu.
- My Co-supervisor: Prof. Tse and Dr. Yam Siwakoti.

Contents

List of Tables

List of Figures

Chapter 1

Introduction

1.1 Research Background

From the beginning of human existence, a need for energy has been essential for the human survival. With the ongoing development of civilization, electrification, automation and digitalization, humans are continuously extracting vast amounts of energy from various sources to meet their demands. Together with the impact of climate change, population growth, and energy crisis, it becomes vital to find alternatives to traditional energy sources, such as sun, wind and water [1–4]. Power electronics plays a major role in interfacing with the energy sources and loads through power conditioning, power conversion, and control [5–9]. It uses power semiconductors and passive devices to convert and control electrical energy. It has been applied in many fields such as high voltage DC systems, hybrid and electric vehicles, elevators, home electric appliances, transportation, robotics and renewable energy applications. With the advances in semiconductors and passive devices, power electronics has high potential to reduce energy production cost effectively. Nowadays, reliability and conversion efficiency are key challenges of power electronics systems as reported in [10–14].

1.2 Motivation and Research Problem

With the increase in the number of sources and loads to manage, it becomes inefficient and costly to have many SISO only power converters to interface with the energy sources and loads. Therefore, in recent decades, much research is contributing to developing MIMO converters at lower cost and improved conversion efficiency [15–17]. This thesis focuses on TPCs because this is the basic unit of a power electronics system, namely, a source, a load and an energy storage element.

The main goal of this research project is to conduct a topological study on all possible power flow combinations and corresponding converter topologies selection, specifically with a bidirectional output port. The benefit of using a bidirectional output port is to make the design readily adaptable to wider applications, such as motor load with regenerative energy and DC grids, in addition to unidirectional output applications. Although there is a small number of TPCs with bidirectional output, to the best knowledge of the author, no previous systematic topological study has been conducted to derive all possible TPCs with two bidirectional ports. Furthermore, it is observed that existing TPCs experience significant voltage overshoot (or undershoot), long settling time and delay during transition of operating modes. In addition, TPCs that have full control of seven modes require many switches. On the other hand, having fewer switches could limit the control dimension, i.e., there could be fewer control variables compared with SISOs. A systematic study has been carried out for some practical configurations, and, based on the required application, a specific configuration is recommended. Power flow graph technique plays a very important role in deciding on a specific configuration for a required application.

1.3 Objectives

The main goal of this research project is to explore practical power electronic converter topologies for energy harvesting and development of DC distribution systems.

The work presented in this thesis contains theoretical study and experimental verification. The theoretical work is verified by using computer simulations such as LTspice© circuit simulator wherever it is necessary. To develop TPCs converters, many aspects should be taken in consideration such as managing different energy sources, dealing with multiple outputs at different voltage levels and achieving maximum power point tracking (MPPT) with high efficiency. The objectives are as follows:

1. To derive all possible power flow graphs for TPCs with two bidirectional ports.
2. To study and analyse TPCs in terms of conversion stages.
3. Model the proposed topologies in a free-available software, such as LTspice©.
4. To identify the optimal power flow configurations based on power flow graph tool.
5. To improve the converter dynamics.
6. To design laboratory hardware prototypes and validate TPCs with seven modes of operation using the minimum number of switches.

1.4 Organization of the Thesis

In Chapter 2, a brief review of power electronic DC/DC converters is carried out. They are classified as isolated, partially isolated and non-isolated converters. In Chapter 3, a review of power flow graphs is studied and, based on that, power flow graphs are proposed and presented for one bidirectional input port and one bidirectional output port. In Chapter 4, two viable converter configurations are identified and selected for further analysis and design of PV-battery systems. In addition, a new method of seamless transitions between different operating modes for three-port DC/DC converters is presented. In Chapter 5, all useful power flow configurations

and their circuit realization are proposed after a brief comparison. This comparison provides a guideline for selecting the right configuration for a specific requirement. In Chapter 6, a new topology of TPC is proposed based on power flow graph configurations. Finally, a conclusion is drawn and future work is explained in Chapter 7.

Chapter 2

Literature Review of Three-Port DC/DC Converters

2.1 Overview

The development of renewable energy systems has attracted research from many disciplines and is still an ongoing process. The main components of any renewable energy system consist of one or more energy sources, storage units and outputs. A straightforward approach widely adopted in the industry is to connect multiple SISO converters to interface with different sources and loads, as depicted in Fig. 2.1. Although this approach offers easier control and modularity, it leads to a relatively bulky, high cost, and less efficient system as there exist at least two power conversions between two of the three ports. On the other hand, TPCs integrate these SISO converters to minimise cost and size as well as deliver better controllability, as shown in Fig. 2.2. In this chapter, the purpose is to review different types of TPCs and show the advantages and disadvantages of each. Studying different types of TPCs can assist in choosing the appropriate converter in a specific application.

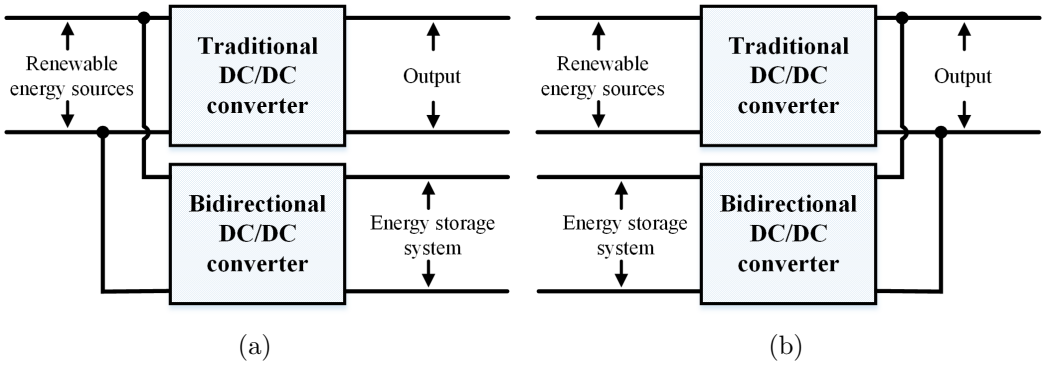

Fig 2.1: Traditional power electronic systems in renewable energy system [24].

2.2 Power Converters

Power electronic converters have been used to resolve the intermittent nature of renewable energy sources by incorporating storage devices and implementing intelligent control strategies. For example, the power converter can use ramp rate control of PV sources and energy storage devices as a buffer to stabilise a weak grid and improve its power quality. In this research, TPCs are studied. Traditionally, two DC/DC converters are separately used, one connects the energy source with the load, and the second is a bidirectional DC/DC converter to connect the energy storage unit with either input or output, as shown in Fig. 2.1 [18–21]. These configurations used two stages of DC/DC converters; the overall efficiency is relatively low as there exists at least one double power processing between two of the three ports. Hence it decreases power density and increases cost [22, 23].

TPCs are widely employed in various applications such as electric vehicles [25–27], hybrid photovoltaic systems [28, 29], and hybrid fuel-cell power systems [30, 31], as shown in Fig. 2.2. TPCs are divided into isolated, partly-isolated and non-

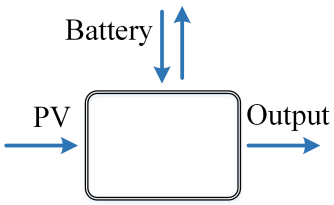

Fig 2.2: TPC with bidirectional input port (energy storage system).

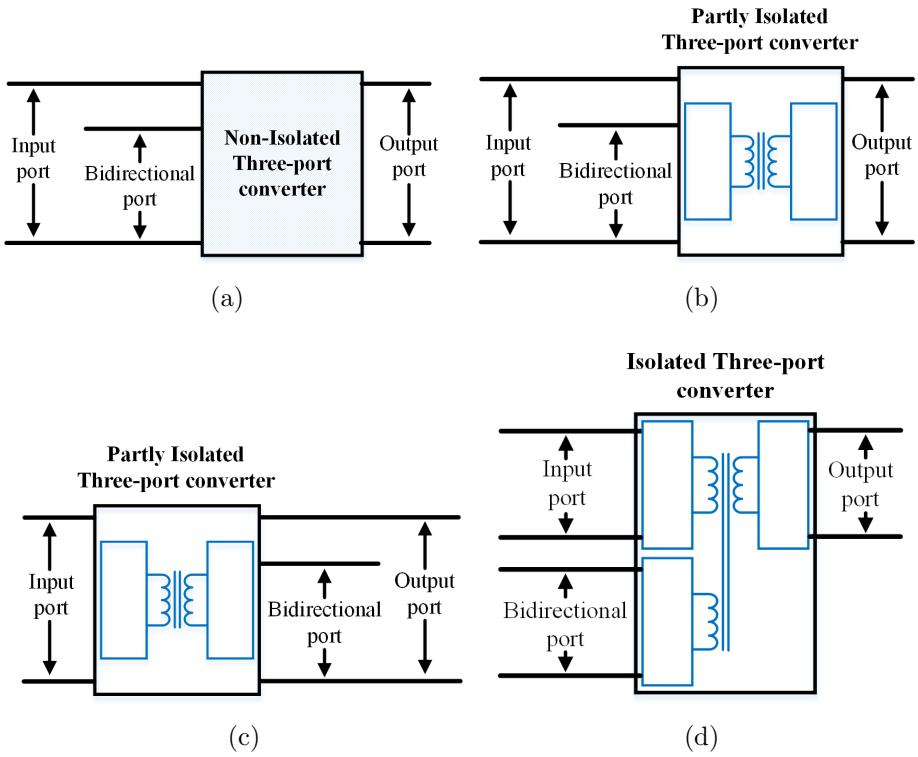

Fig 2.3: TPCs structure. a) Non-isolated TPC converter. b) & c) Partly-isolated TPC converter. d) Isolated TPC converter [24].

isolated types. These types of converters have been reviewed previously [24, 32, 33]. Fig. 2.3 shows their general structures. Isolated TPCs can achieve high-voltage gain and voltage matching where galvanic isolation between any two ports is obtained. However, using a multi-winding transformer and many active switches increases the converter cost and size [34, 35]. Partly-isolated TPCs can achieve a relatively higher voltage gain than non-isolated TPCs, and the isolation is set up between only two of the three available ports [36]. In contrast, non-isolated TPCs are compact and cost-effective, but they can only be used where galvanic isolation is not required [37–39]. However, designers should be aware of high power and safety requirements.

2.2.1 Isolated DC/DC Converters

In isolated TPCs, all ports are isolated from each other. These converters are constructed based on conventional half-bridge or full-bridge converters. As discussed earlier, the main advantages are isolation and high voltage gain, which is achieved

via transformer turns ratio. In [40], an isolated half-bridge TPC is presented, which consists of three half-bridges and a high-frequency multi-winding transformer, as depicted in Fig. 2.4. Bidirectional power flow is achieved by adjusting the phase-shift angles of the voltages across the two sides of the transformer. In [41], an isolated full-bridge TPC with bidirectional power flow is presented. Similar to [40], this topology consists of three full-bridges instead of three half-bridges, as shown in

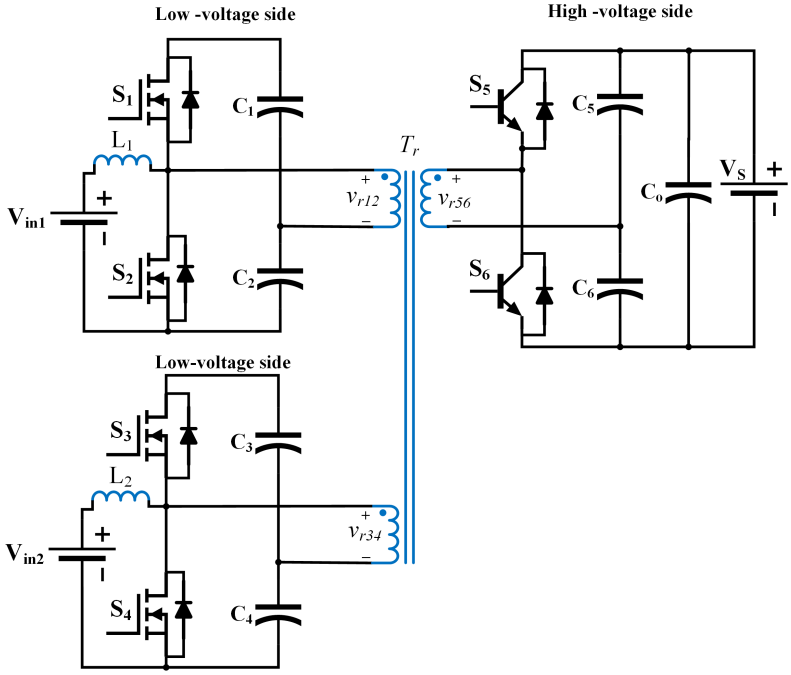

Fig 2.4: Isolated half-bridge three-port bidirectional converter [40].

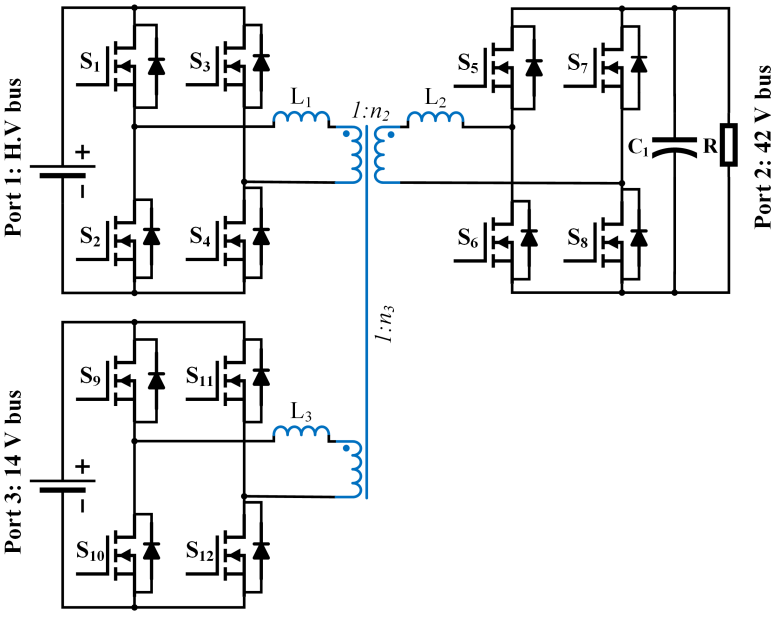

Fig 2.5: Isolated full-bridge three-port bidirectional converter [41].

Fig. 2.5. It has decoupled the power flow management for all ports. The advantage is ensuring zero circulating power within the converter when the duty cycle variation at each port, reduces the switching losses for voltage variations.

2.2.2 Partly-Isolated DC/DC Converters

In partly-isolated DC/DC converters, at least one port is isolated using a high-frequency transformer, as shown in Figs. 2.3(b) and 2.3(c). This offers galvanic isolation for that port and high voltage gain. These converters are classified based on the topology structure of full-bridge and half-bridge converters [42]. A full-bridge TPC is presented in [43]. The proposed topology integrates two buck-boost converters into the primary side of the full-bridge topology, as shown in Fig. 2.6. The advantages of this topology are single-stage power conversion between any two ports and ZVS for all the primary switches. However, due to the freewheeling operation, the conduction loss is high. In [44], the authors proposed a TPC using an interleaved-boost integrated full-bridge converter for hybrid renewable energy sources, as shown in Fig. 2.7. The converter can achieve dual-input, dual-output and two SISO modes.

On the other hand, some researchers studied half-bridge converters to reduce the cost and size. In [45], an interleaved half-bridge TPC is presented similar to [42], where the conduction loss problem is resolved. In [46], a TPC was derived by integrating a bidirectional converter and series-resonant converter, as shown in

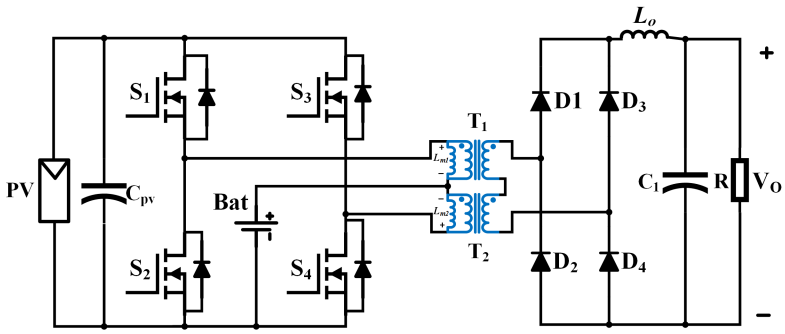

Fig 2.6: Two buck-boost full-bridge converter [43].

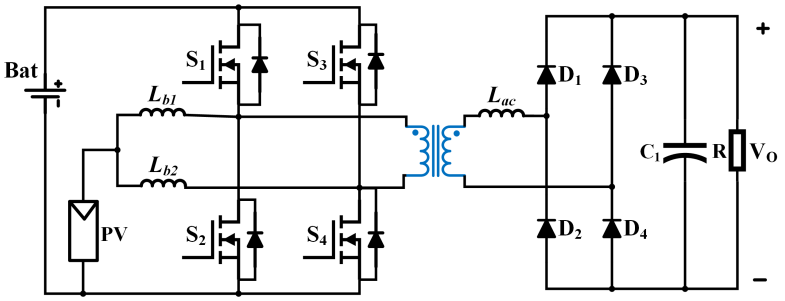

Fig 2.7: Interleaved-boost full-bridge converter for hybrid energy sources applications [44].

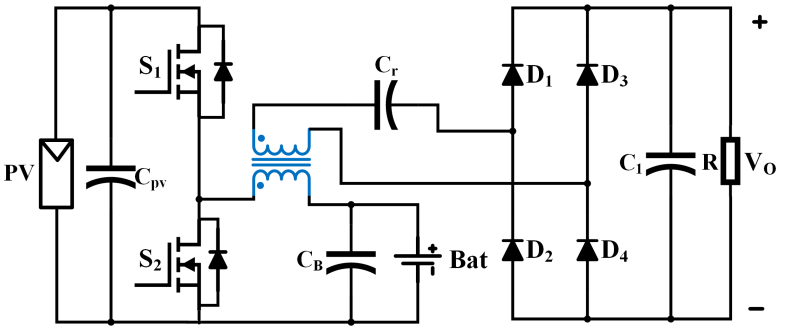

Fig 2.8: Partly-isolated half-bridge TPC with single-magnetic [46].

Fig. 2.8. It reduced the size and circuit complexity since only a single magnetic component was used. However, the voltage regulation range was narrow.

2.2.3 Non-Isolated DC/DC Converters

In non-isolated converters, all ports are connected to each other directly without isolation. This topology is useful in applications such as PV-battery systems where isolation is not necessary. The advantages of this topology are better efficiency, lower cost, and compact size. However, it has a limited voltage regulation ratio according to the duty cycle of the converter, and it is difficult to achieve ZVS. To achieve high voltage gain, multiple stages should be used as in [47]. Some proposed circuits with high step-up converters are presented in [48] and [49]. The conventional non-isolated DC/DC converters are buck, boost, boost/buck, SEPIC, Ćuk, or ZETA converter [50].

In [9,51], single-switch TPCs are proposed. It has many advantages over other

TPCs. Firstly, only one switch is used so it is compact. Secondly, the control circuit is simple. Thirdly, the redundant path of the battery for charging and discharging is eliminated, as in Fig. 2.9. Each branch could be a buck, boost or a buck-boost converter. However, a lower number of switches could limit the control dimension.

In [52], the authors proposed a non-isolated TPC with a high voltage gain for standalone renewable power applications. In the proposed circuit, three controlled switches are used to achieve the power flow control, as in Fig. 2.10. These converters can operate in three different modes: SISO, double-input, single-output (DISO), and single-input, double-output (SIDO). However, many power devices are used in that topology, and only three modes are considered.

In [53], the authors proposed a TPC for hybrid PV, fuel cell, and battery systems, as shown in Fig. 2.11. The proposed circuit involved a boost and buck-boost converter. Four power switches and four diodes were used to provide two unidirectional power flows for the PV module and FC and one bidirectional power flow for the battery. The battery is used to smooth the output power, startup transition, and supply more power for various load conditions. In [54], a modified non-isolated TPC with variable structures is presented. Non-isolated TPCs suffer from port voltage restrictions. However, the proposed variable structure TPC overcomes this issue and extends the voltage restrictions of these ports by appropriate switch control. In addition, the topology uses only one inductor; therefore, it is easy to achieve

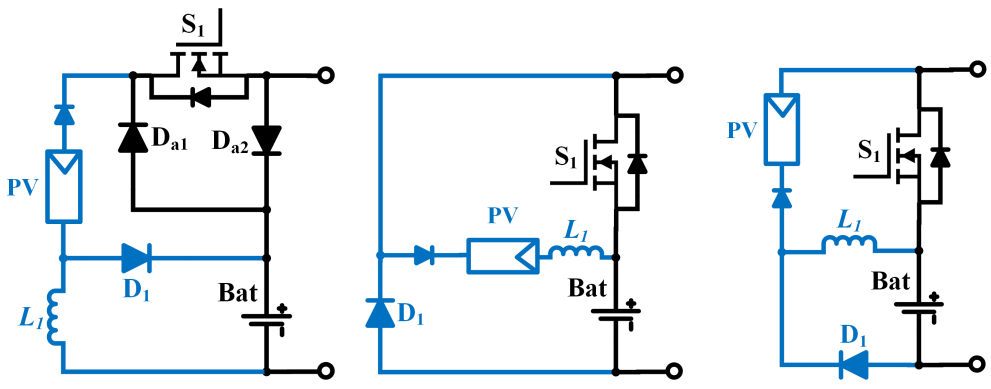

(a) Buck (b) Boost (c) Buck-boost

Fig 2.9: All possible configurations of branch1 and branch2 [51].

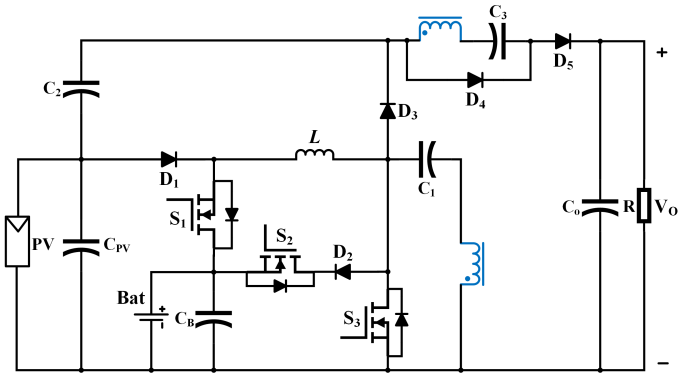

Fig 2.10: The proposed circuit in [52].

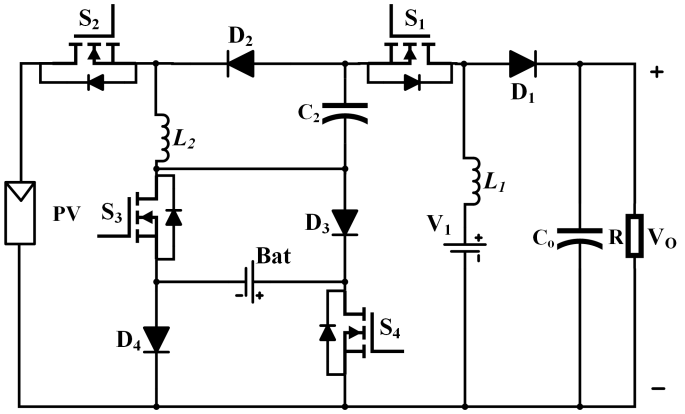

Fig 2.11: The proposed circuit in [53].

compact size. The structures between the ports could be buck, boost or buck-boost features, as in Fig. 2.12. One of these variable structures was analysed in detail. Eight operational modes of this TPC are designed to obtain five different power management requirements and three-port voltage restrictions.

In [55], a non-isolated TPC with one bidirectional port is presented. This work presents a compact design of TPC and a single power processing feature, as shown in Fig. 2.13. However, the control dimension is inevitably limited as MPPT; voltage regulation cannot be achieved simultaneously.

In [56], a TPC with two bidirectional ports is presented. It can work in seven different modes of operation. In [57], a non-isolated single-inductor DC/DC converter with a fully reconfigurable structure for renewable energy applications as in Fig. 2.14 is presented. It has a single power conversion between any two ports, a single inductor topology, and a simple control strategy. In addition, seven modes of

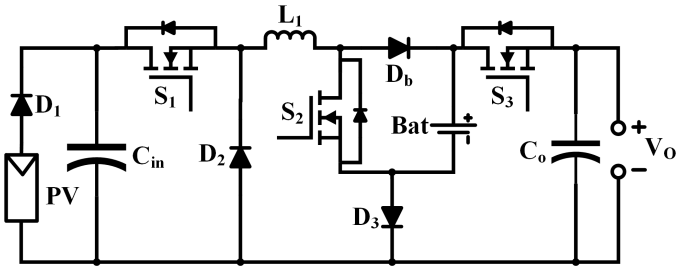

Fig 2.12: Variable structure TPCs based on the buck-boost converter and SSD cell [54].

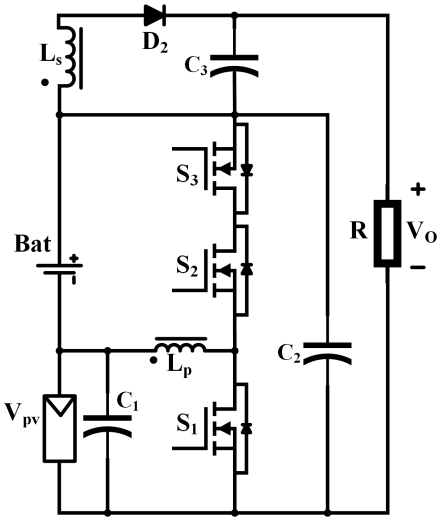

Fig 2.13: A TPC using voltage stacking technique to increase output voltage [55].

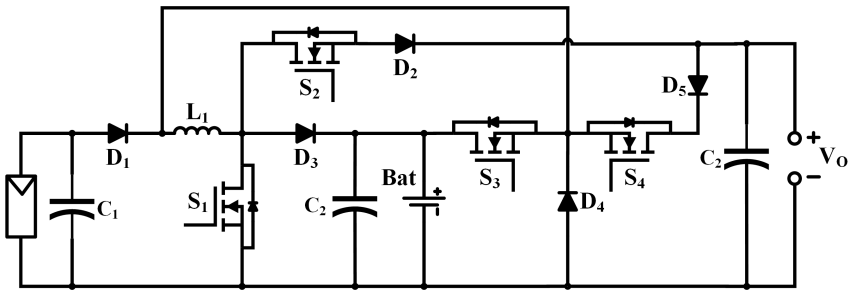

Fig 2.14: A schematic of the presented TPC design example with soft-switching cells [57].

operation have been achieved at the expense of using four switches and five diodes. In [58], an integrated magnetic three-port converter (IMTPC) with current ripple cancellation for all ports and high power density is presented. Magnetic integration is added to achieve power conversion, ripple cancellation and switch driver simultaneously, and only two magnetic devices are needed.

2.3 Summary

TPCs are widely employed in various applications and show better performance than traditional multiple SISO. TPCs are divided into isolated, partly-isolated and non-isolated types. These types of converter have been reviewed in this chapter. Isolated TPCs can achieve high voltage gain and voltage matching where galvanic isolation between any two ports is obtained. However, using a multi-winding transformer and many active switches increases the converter cost and size. Partly-isolated TPCs can achieve a relatively higher voltage gain than non-isolated TPCs, and the isolation is between two ports only. In contrast, non-isolated TPCs are compact and cost-effective but can only be used where galvanic isolation is not required. However, designers should be aware of high power and safety requirements. In the next chapter, the power flow graphs tool will be used to derive different TPC configurations, where any type of these converters can be applied. However, this thesis focuses on non-isolated TPCs as it is the most appropriate type for PV-battery systems.

Chapter 3

Power Flow Graphs of Three-Port Converters and Derivations

3.1 Introduction

TPCs may consist of a unidirectional port, such as a PV source, or a bidirectional port, such as a battery [59–61]. Therefore, the arrangement of converters and controllers for the power flow distribution in a TPC plays a vital role in the overall performance and efficiency. Recently, a systematic analytical technique for different configurations has been proposed [62–64]. the power flow graphs technique was first presented in [65] and [66] for power factor correction (PFC) converters. Power flow graphs provide a systematic approach to analyse power processing stages and direction among the power ports. The technique is extended in [62] to derive all possible three-port DC/DC converters with a unidirectional output port and extended in [67]. However, for some applications, such as electric vehicles, a bidirectional output port is required to handle regenerative braking [68, 69]. Therefore, this chapter focuses on providing a systematic topological study to derive all possible configurations of TPC with two bidirectional ports. The significance of this work is to show which configuration has fewer power conversion stages between any two ports.

Furthermore, it shows if all ports are fully or partially controlled and presents the appropriate configuration for specific applications.

This chapter is organised as follows: In Section 3.2, a literature review of power flow graphs is presented. Two examples of DISO are studied in this literature where in the first example, all ports are unidirectional and in the second example, only one bidirectional port is constructed. In Section 3.3, based on the power flow graph explained in the literature review, power flow graphs are derived and proposed for two bidirectional ports, followed by conclusion in Section 3.4.

3.2 Literature Review

Based on the power flow graph technique, there are three types of power flow subgraphs: (1) In Type I, the power is transferred separately from one port to another, as shown in Fig. 3.1(a); (2) Type II, the power is transferred simultaneously from two ports to one, as shown in Fig. 3.1(b); (3) In Type III, the power is transferred simultaneously from one port to two ports, as shown in Fig. 3.1(c). There are two examples of DISO converters, which are studied in this literature review. The first example is a DISO converter where all the ports are unidirectional ports using Type-I and Type-II power flow subgraphs. The second example is a DISO converter which has one bidirectional port (battery) while the other two ports are unidirectional using all the three power flow subgraphs.

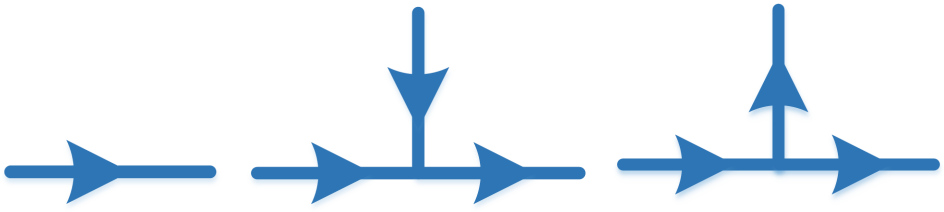

(a) Type I (b) Type II (c) Type III

Fig 3.1: Power flow subgraphs of TPCs [62].

3.2.1 DISO Converters with Unidirectional Input and Output Ports

As all ports are unidirectional in this configuration, only Type I and Type II are required. Based on the power flow subgraphs as in Fig. 3.1, complete power flow graphs for all DISO converters were constructed and are shown in Fig. 3.2. All possible converters connections are explained in four different power flow graphs. A Type I-I graph involves two Type I subgraphs. Then, a Type I-II graph involves one Type I subgraph and one Type II subgraph, which has two subtypes inside, namely, Type I-IIA and I-IIB. Finally, the Type II-II power flow graph involves two Type II subgraphs. One important point is that Types I-IIA and I-IIB are identical due to the spatial symmetry between inputs I and II.

As in Fig. 3.2, two power flow subgraphs are used. Therefore, two converters will be placed in appropriate paths of the power flow graphs to build all possible DISO converters. Thirteen configurations of DISO are obtained and shown in Fig. 3.3. Square boxes on the arrows denote a simple converter. All configurations are namely I-I, I-IIA, I-IIB, I-IIC, II-IIA, II-IIB, II-IIC, II-IID, II-IIE, II-IIF, II-IIG,

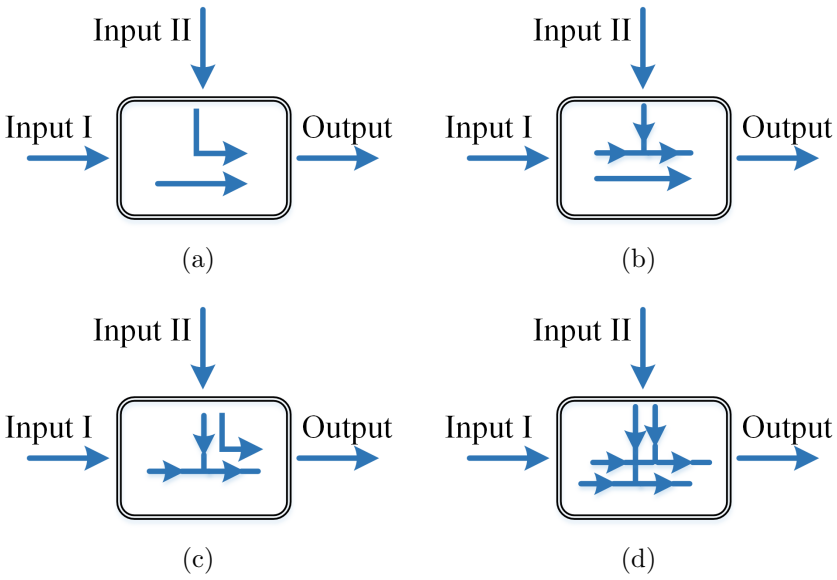

Fig 3.2: Power flow graphs of DISO converters with unidirectional input and output ports. (a) Type I-I. (b) Type I-IIA. (c) Type I-IIB. (d) Type II-II [62].

II-IIH, and II-II I. Due to spatial symmetry, II-IIA configuration is equivalent to II-IIH configuration, II-IIB configuration is equivalent to II-IIG configuration, and II-IIC configuration is equivalent to II-IID, II-IIE, and II-III configurations. Finally, only eight unique configurations exist for DISO converters, namely, I-I, I-IIA, I-IIB, I-IIC, II-IIA, II-IIB, II-IIC, and II-IIF configurations.

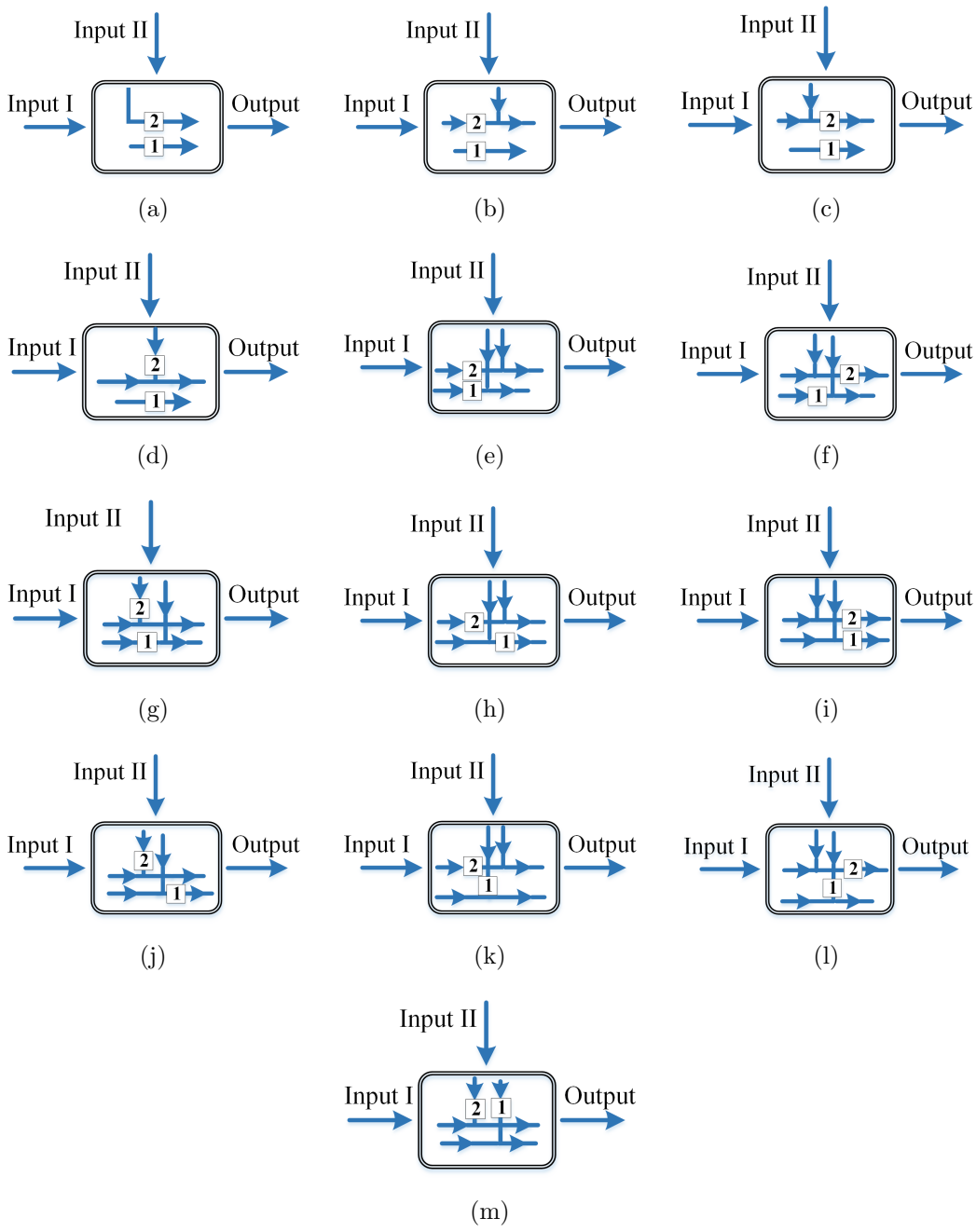

Fig 3.3: All possible configurations of DISO with unidirectional input and output ports. (a) I-I. (b) I-IIA. (c) I-IIB. (d) I-IIC. (e) II-IIA. (f) II-IIB. (g) II-IIC. (h) II-IID. (i) II-IIE. (j) II-IIF. (k) II-IIG. (l) II-IIH. (m) II-III [62].

3.2.2 DISO Converters with One of the Input Ports Being Bidirectional

One of the input ports is bidirectional (for battery application, for example) and one unidirectional output port. It contains all three types of power flow subgraphs, as shown in Fig. 3.1. Based on the power flow subgraphs as in Fig. 3.1. Complete power flow graphs for all DISO converters were constructed in Fig. 3.4. All possible converters connections are explained in four different power flow graphs. Type I-I graph, which involves two Type I subgraphs. Then, a Type I-II graph involves one Type I subgraph and one Type II subgraph. Then, a Type I-III graph involves one Type I subgraph and one Type III subgraph. Finally, a Type II-III power flow graph involves one Type II subgraph and one Type III subgraph. One important point is that Type II-II and III-III are not acceptable because one battery input or output will not be connected.

According to the theory in [65], the minimum number of converters to construct two subgraphs together is two. Therefore, a pair of converters will be placed in appropriate paths of the power flow graphs to build all possible DISO converters. Sixteen configurations of DISO are obtained as in [66]. All configurations are namely I-I, I-IIA, I-IIB, I-IIC, I-IIIA, I-IIIB, I-IIIC IIA-IIIA, IIA-IIIB, IIA-IIIC, IIB-IIIA, IIB-IIIB, IIB-IIIC, IIC-IIIA, IIC-IIIB, and IIC-IIIC. According to [66], out of these 16 configurations, only five have been used for practical implementation because of the usefulness, namely I-I, I-IIA, I-IIB, I-IIIA, and I-IIIB. It was rearranged in 2015 by [62] to be four configurations as in Fig. 3.5.

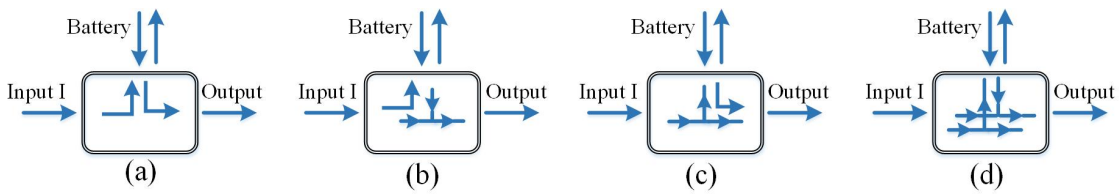

Fig 3.4: Power flow graphs of a DISO converter with one of the input ports is connected to the battery as a bidirectional port. (a) Type I-I. (b) Type I-II. (c) Type I-III. (d) Type II-III [62].

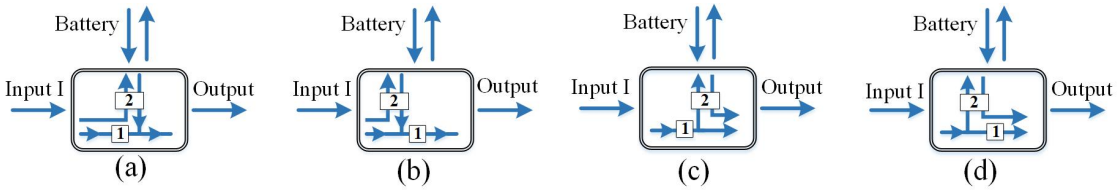

Fig 3.5: Selected four configurations of DISO with one of the input ports connected to the battery as a bidirectional port. (a) I-IIA. (b) I-IIB. (c) I-IIIA. (d) I-IIIB [62].

3.3 Proposed Power Flow Graphs

In addition to the battery, a bidirectional output port is useful in other applications such as electric vehicles (regenerative/braking mode) and DC microgrids. The block diagram of a bidirectional battery input port with a bidirectional output port is shown in Fig. 3.6. Power flow subgraphs of TPC with a bidirectional output port are the same as the unidirectional output port as in Fig. 3.1. PV is considered one of the renewable energy sources for the input port, and a DC bus is the bidirectional output port.

All possible power flow graphs of Type I are presented in Fig. 3.7. Then, all possible power flow graphs of two of Type I are presented in Fig. 3.8. However, a minimum of three of Type I are required to ensure that all ports are connected. Therefore, three power flow graphs illustrating three Type-I configurations are shown in Figs. 3.9(a) and 3.9(b) utilising all ports. However, one power flow path is not considered, such as in Fig. 3.9(a), PV to battery or in Fig. 3.9(b), PV to DC bus. Therefore, four of Type I is constructed in Fig. 3.9(c). These configurations are separated and require three or Four individual converters, which is less efficient and

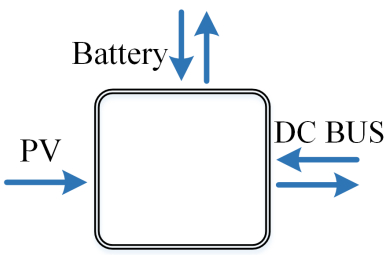

Fig 3.6: The block diagram of a bidirectional battery input port with a bidirectional output port.

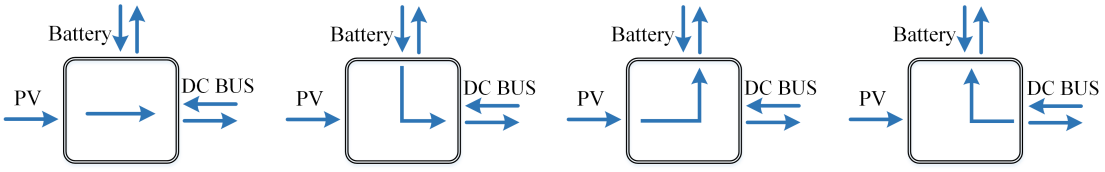

(a) PV to DC bus (b) Battery to DC bus (c) PV to Battery (d) DC bus to Battery

Fig 3.7: All possible power flow graphs of Type I.

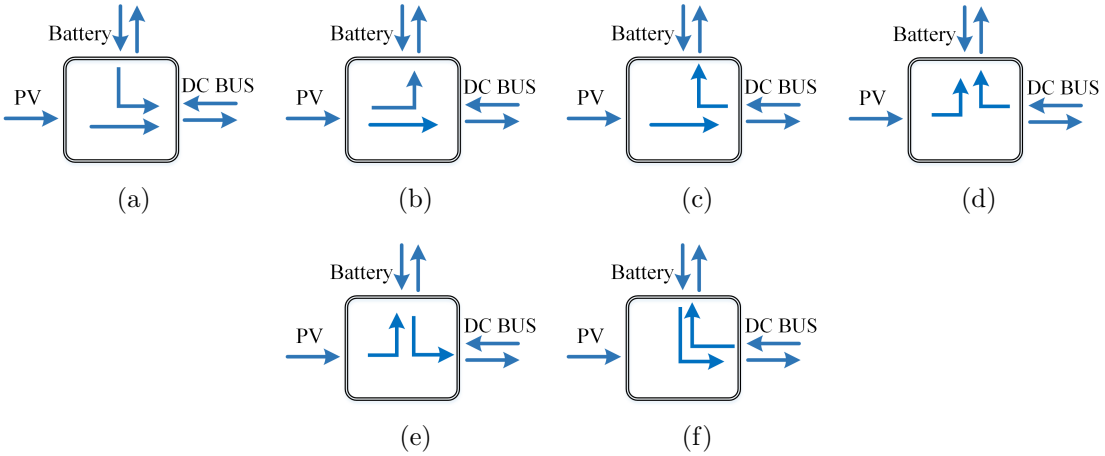

(a) (b) (c) (d) (e) (f)

Fig 3.8: All possible power flow graphs of two of Type I. a) PV to DC bus & battery to DC bus. b) PV to DC bus & PV to battery. c) PV to DC bus & DC bus to battery. d) PV to battery & DC bus to battery. e) PV to battery & battery to DC bus. f) battery to DC bus & DC bus to battery.

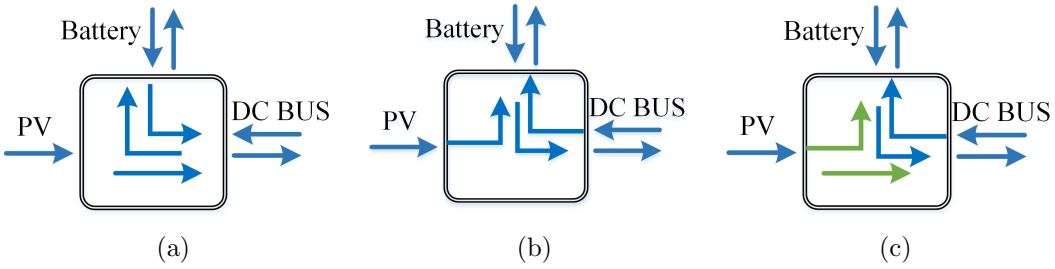

(a) (b) (c)

Fig 3.9: All possible power flow graphs of three or more Type I configurations. a) Battery to DC bus, DC bus to battery & PV to DC bus. b) Battery to DC bus, DC bus to battery & PV to battery. c) Battery to DC bus, DC bus to battery, PV to DC bus & PV to battery.

costly.

As a result, power flow graphs of Type I and Type II are mixed, the resulting configurations are shown in Fig. 3.10(a), and 3.10(b). However, no direct connection between PV to the battery, as shown in Fig. 3.10(a), and no direct connection between PV to DC bus as shown in Fig. 3.10(b) exists. To overcome this issue,

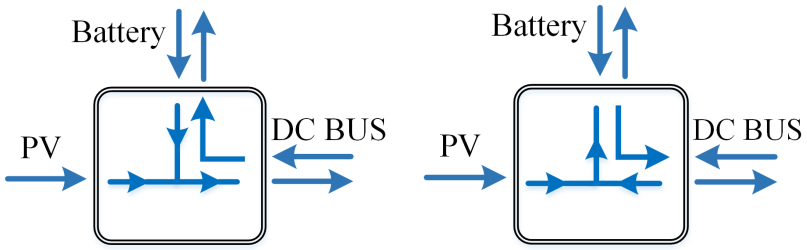

(a) No direct connection between PV to Battery

(b) No direct connection between PV to DC bus

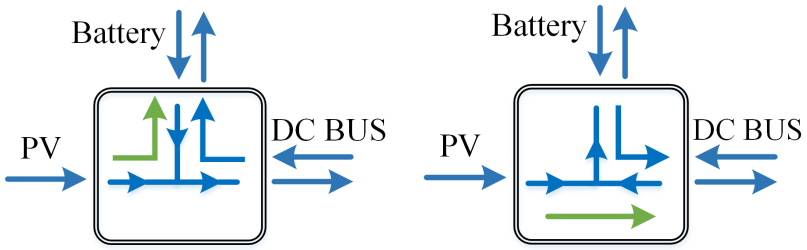

(c) TypeI-II-IA

(d) TypeI-II-IB

Fig 3.10: Mixture of Type I and Type II configurations.

Type I-II-IA and Type I-II-IB are presented in Fig. 3.10(c) and Fig. 3.10(d), respectively. However, the last two configurations increase the number of switches. Another possible combination is one power flow graph of two of Type II as shown in Fig. 3.11(a). The last possible combination is two of Type I with Type III as shown in Fig 3.11(b). The advantage of this configuration is in using the Type III configuration, which has one input (PV) and two outputs (battery and DC bus), with a bidirectional converter connected between the battery and DC bus. It is worth noting that there are no possible configurations of Type II-III and Type III-III as one direction of the bidirectional port will not be connected in this power flow configuration. As clearly displayed in Figs. 3.9, 3.10, and 3.11, there are significant changes in the power flow graphs compared to a single bidirectional port in [62] and presented in Fig. 3.4.

According to the circuit theory [65], to construct two subgraphs together, a minimum of two separate and basic converters are required. Therefore, two converters are placed on the power flow graphs in proper paths to build all possible TPCs, as in Fig. 3.12. In Fig. 3.12(a), one unidirectional converter connects PV to the

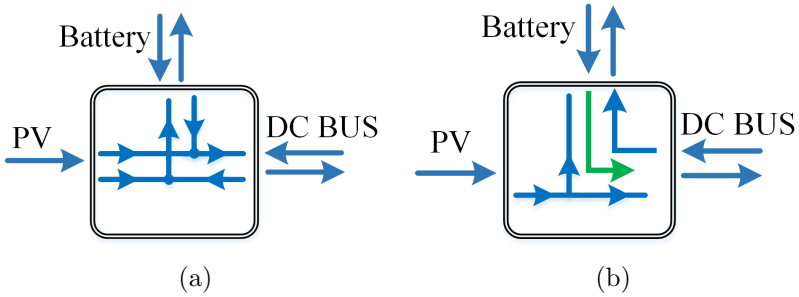

(a) (b)

Fig 3.11: A mixture of different subgraphs. a) Mixture of 2 of Type II configurations. b) Mixture of 2 of Type I and Type III configurations.

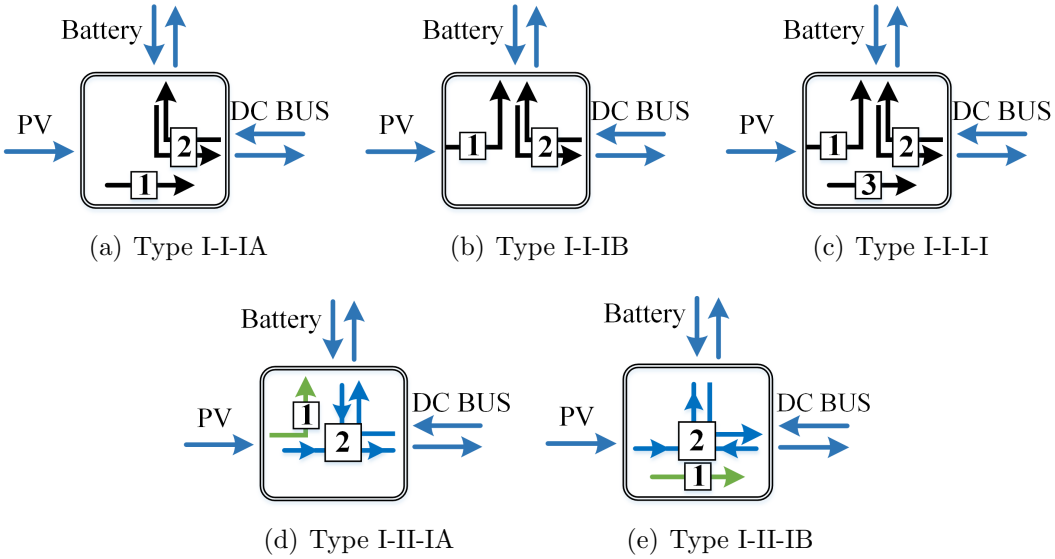

(a) Type I-I-IA (b) Type I-I-IB (c) Type I-I-I

(d) Type I-II-IA (e) Type I-II-IB

Fig 3.12: Some possible power flow graphs configurations based on Figs. 3.9 and 3.10.

DC bus, and a bidirectional converter is connected between the battery and the DC bus. The difference between Fig. 3.12(a) and Fig.3.12(b) is the connection of the PV source with the battery instead of the DC bus. In Fig. 3.12(c), two unidirectional converters and one bidirectional converter have been used. Fig. 3.12(d) and Fig. 3.12(e) have a central converter with a bidirectional port from the DC bus and the battery. The only difference is the connection of the unidirectional converter.

For Type II-II, two converters are placed on the power flow graphs in their proper paths to build all possible TPCs using only unidirectional SISO converters, as in Fig. 3.13. Upon further inspection of each configuration, one of the ports is connected directly without a converter, leaving it out of control. Therefore, there is

a trade-off between controllability and the number of converters. As the direction of this work is towards full control, only three configurations, where all ports are controlled, are useful, as in Fig. 3.14. In Chapter 4, these configurations are studied in detail.

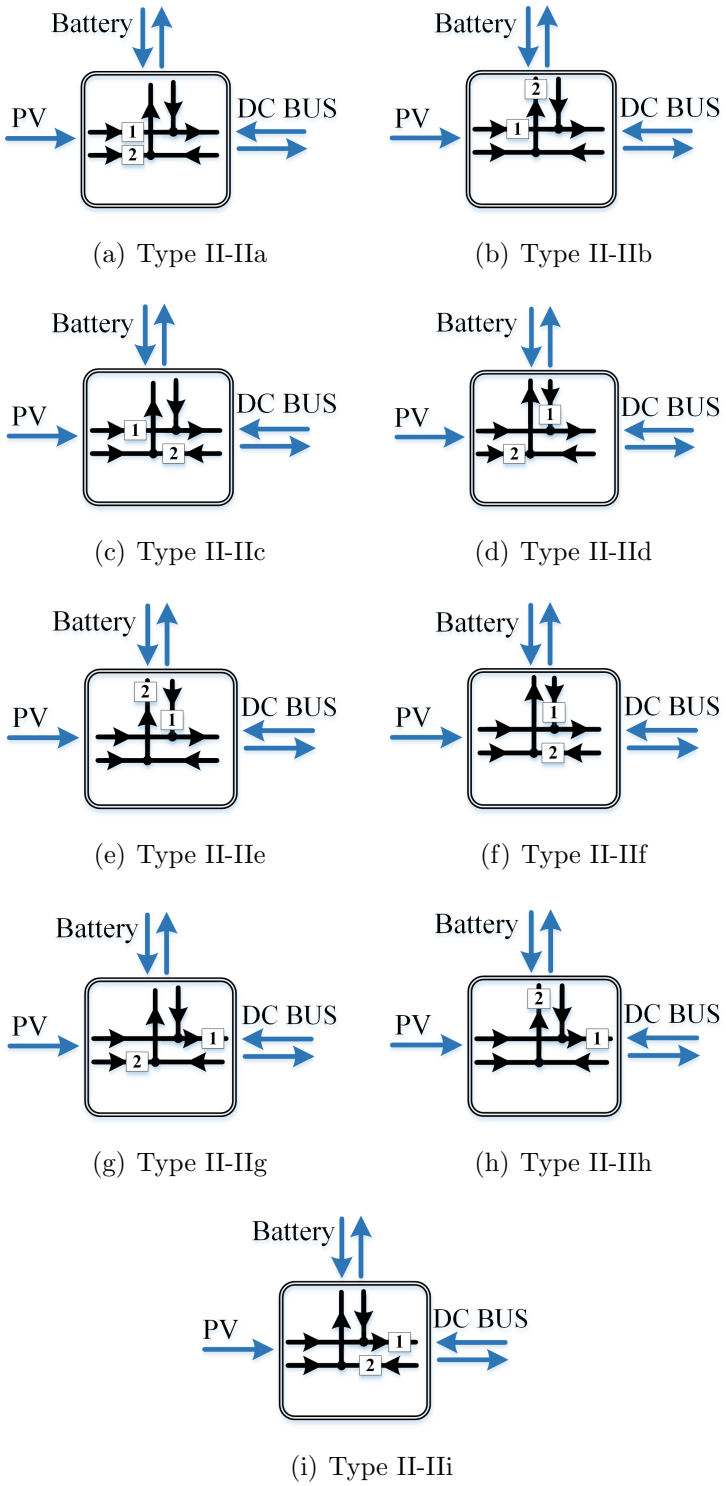

(a) Type II-IIa (b) Type II-IIb

(c) Type II-IIc (d) Type II-IId

(e) Type II-IIe (f) Type II-IIf

(g) Type II-IIg (h) Type II-IIh

(i) Type II-IIi

Fig 3.13: All possible configurations of Power flow graph of 2 of Type II.

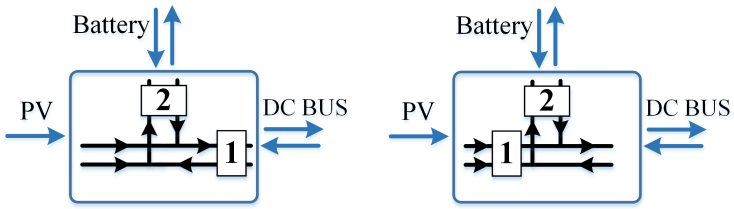

(a) Type II-IIA (b) Type II-IIB

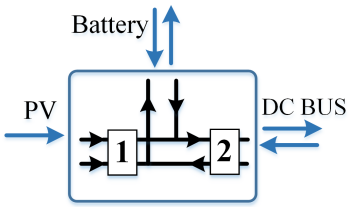

(c) Type II-IIC

Fig 3.14: Modified configurations of the TPC with one bidirectional input port and bidirectional output port.

Similarly, Type I-III-I configurations are proposed in Fig. 3.15. All of these configurations have a bidirectional converter between the battery and the DC bus. In Fig. 3.15(a), the PV source is connected directly to the DC bus and to the battery through a unidirectional converter. In Fig. 3.15(b), the PV is connected directly to the battery. In Fig. 3.15(c), the PV source is connected to the DC bus and the battery through a converter. In Fig. 3.15(d), the PV source is connected

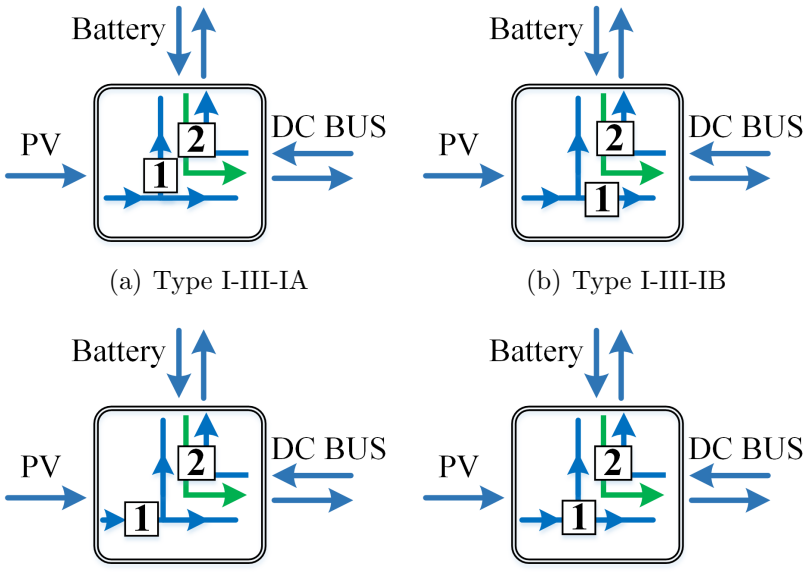

(a) Type I-III-IA (b) Type I-III-IB

(c) Type I-III-IC (d) Type I-III-ID

Fig 3.15: All possible arrangements of Type I-III-I configuration.

Table 3.1: Possible combinations of proposed converter structures based on non-isolated basic DC/DC converters.

Configuration	Converter 1	Converter 2	Condition
Type I-I-IA	Any	Any	–
Type I-I-IB	Any	Any	–
Type II-IIA	Boost	Boost	$V_{Bat}<V_{PV}<V_{DC}$
		Buck	$V_{PV}<V_{Bat}$ & $V_{PV}<V_{DC}$
	Buck	Boost	$V_{Bat}<V_{PV}$ & $V_{DC}<V_{PV}$
		Buck	$V_{DC}<V_{PV}<V_{Bat}$
	Buck-boost	Boost	$V_{Bat}<V_{PV}$
		Buck	$V_{PV} < V_{Bat}$
Type II-IIB	Boost	Boost	$V_{Bat}<V_{DC}$ & $V_{PV}<V_{DC}$
		Buck	$V_{PV}<V_{DC}<V_{Bat}$
	Buck	Boost	$V_{Bat}<V_{DC}<V_{PV}$
		Buck	$V_{DC}<V_{Bat}$ & $V_{DC}<V_{PV}$
	Buck-boost	Buck-boost	
Type II-IIC	Boost	Boost	$V_{PV}<V_{Bat}<V_{DC}$
		Buck	$V_{PV}<V_{Bat}$ & $V_{DC}<V_{Bat}$
	Buck	Boost	$V_{Bat}<V_{PV}$ & $V_{Bat}<V_{DC}$
		Buck	$V_{DC}<V_{Bat}<V_{PV}$
Type I-III-IA	Boost	Buck-boost	$V_{DC}<V_{PV}$
	Buck	Buck-boost	$V_{Bat}<V_{PV}$ & $V_{DC}<V_{PV}$
Type I-III-IC	Boost	Buck-boost	–
	Buck	Buck-boost	$V_{Bat}<V_{PV}$ & $V_{DC}<V_{PV}$
Type I-III-ID	Boost	Buck-boost	$V_{PV}<V_{Bat}$ & $V_{PV}<V_{DC}$
	Buck	Buck-boost	$V_{Bat}<V_{PV}$ & $V_{DC}<V_{PV}$

to the battery and DC bus through a central converter. In Figs. 3.12, 3.14, and 3.15, converters 1 and 2 could be transformer-based, bridge-based, Ćuk, ZETA, SEPIC, or basic converters such as buck, boost, or buck-boost converters. Therefore, for simplicity, only basic converters will be considered, as shown in Table. 3.1. Type I-III-IA and Type I-III-IB are identical due to spatial symmetry between the two bidirectional ports. Therefore, both of them have the same combinations. In Chapter 5, all possible power flow graphs, more specifically those converters having three power flow subgraphs such as Type I-III-I and Type I-II-I, will be presented. Each of these configurations has been studied, and circuit realisation undertaken. Finally, one of the most appropriate power flow configurations, namely, Type I-III-IA, will be studied in detail, and the experimental validation will be carried out in Chapter 6.

3.4 Summary

This chapter presents a topological study to derive all possible TPCs by using power flow graphs. Based on two conventional DISO converters, a TPC with a bidirectional output port is discussed in detail. The number of possible converter candidates is minimised to select the best topology with the necessary desired performance. Due to their indirect connection, impractical configurations violating the circuit rules and multiple conversion stages have been eliminated.

Chapter 4

A Method of Seamless Transitions Between Different Operating Modes for TPCs

.

4.1 Introduction

All possible power flow combinations for two bidirectional ports have been constructed previously in Chapter 3, which cover cases with all ports fully or partially controlled as well as selected configuration for specific applications. This chapter focuses on two of the most appropriate power flow configurations, namely, Type II-IIA and Type II-IIB. These configurations offer a single-stage converter to increase the efficiency and a full control of the ports. In contrast, Type II-IIC is eliminated as two-stage converter is needed in the primary path (PV-DC bus). A first proposed circuit of Type II-IIA is presented in Fig. 4.1(a) with a bidirectional buck-boost converter between PV and DC bus and a boost-buck converter connected to the battery. Then, a second proposed circuit of Type II-IIB is presented in Fig. 4.1(b) with a

synchronous buck converter between PV and DC bus and a boost-buck converter connected between the battery and DC bus.

Most of the reported works aim to achieve MPPT, battery voltage regulation and output voltage regulation (OVR). However, not all control objectives are achieved simultaneously [55, 70]. Although it is integrated and has single power processing feature for all ports, the control dimension is inevitably limited. In addition, the PV to load transfer mode can not be activated without physically disconnecting the battery [71]. Other TPCs are presented in [56] and [72], where the battery regulation is achieved by estimating the state-of-charge from the terminal voltage, and mode transition is activated and restricted to only after a specific period of time. In [73], the transition between modes occurs after a delay of 0.3 s and the PV array is emulated by dc voltage source. In [74] & [75], three-port bidirectional DC/DC converters are proposed with new control strategy. However, transition between modes is not considered. A two-stage solar PV based TPC is proposed in [76]. This converter has a balanced control in selecting between MPPT and battery voltage regulation. However, it does not allow for no load and full PV power scenarios. There is also an overshoot and a delay in the transition between modes. TPCs with two bidirectional ports is presented in [77, 78]. However, mode transition is achieved by assigning specific switching patterns periodically, which causes a delay in the response and unavoidable noise in the circuit. Also, the errors in sensors may lead to inaccurate response.

Based on Table 4.1 and motivated by all these challenges, this chapter presents two typical TPCs with two bidirectional ports and a simple switching pattern control for all the switches so that the system can move from one mode to another according to the power of each port. MPPT, output voltage regulation and battery voltage regulation can be achieved simultaneously. The following advantages are summarizing the contributions of this work:

- Only 4 sensors are used as compared to 6 sensors in the conventional method.

Table 4.1: Comparison between the proposed method and others.

Reference	Modes	Delay	Overshoot	Settling time	Complex control	Selection Conditions	Modes Transition	Sensors
[79]	3	-	-	-	Mid	3	Simulation results	6
[80]	3	-	-	-	-	Not shown	Simulation results	5
[81]	3	-	-	-	Mid	3	Simulation results	Not considered
[82]	3	-	-	-	Mid	3	Simulation results	6
[83]	4	-	-	-	Mid	4	Not considered	5
[84]	4	-	-	-	Mid	3	One case only	5
[85]	4	-	-	-	-	3	Not considered	4
[70]	4	-	-	-	Mid	3	Not considered	6
[55]	5	No	10%	0.4 s	High	5	Experimental	6
[71]	4	No	40%	0.2 s	Mid	4	Experimental	6
[56]	7	Yes	20%	1 s	High	4	Experimental	5
[72]	7	Yes	No	1 s	High	4	Experimental	5
[76]	4	No	50%	0.6 s	Mid	4	Experimental	6
[77]	6	-	-	-	Mid	3	Simulation results	5
[78]	6	Yes	-	-	Mid	4	Experimental	6
[86]	3	No	10%	0.2 s	Mid	3	Experimental	6
[87]	3	No	10%	0.2 s	Low	2	Experimental	6
[88]	3	No	30%	0.3 s	Mid	3	Experimental	6
Proposed	7	No	10%	0.1 s	Low	2	Experimental	4

- Only two selection conditions are required as compared to 4 or 5 in prior works.
- This work considers two bidirectional ports as compared with only one bidirectional port in most reported topologies. This enables both standalone and DC grid-connected applications.
- 7 modes of operation with seamless and smooth transition between mode is achieved.
- Fast response where maximum settling time is 100ms or less.

This chapter is organized as follows: In Section 4.2, the circuit design, principles of operation and working conditions of Type II-IIA and Type II-IIB configurations are studied. In Section 4.3, the control structure and mode selection are explained. In Section 4.4, the experimental setup and measured waveforms are presented, followed by summary in Section 4.5.

4.2 Operation of Types II-IIA and II-IIB Converters

This section discusses the circuit operation of Type II-IIA and Type II-IIB converters, which is applied to a PV-battery powered DC system. In these circuits,

a PV source is connected to a unidirectional input port, whereas the battery and DC bus are connected to bidirectional ports. In the Type II-IIA converter, the first converter that connects the PV to the DC bus is a bidirectional buck-boost converter and the second converter is a bidirectional buck-boost converter connecting the PV to the battery, as shown in Fig. 4.1(a). Type II-IIA circuit has a single power processing in PV to DC bus, PV to battery, and PV to battery and DC bus modes. In addition, it is easy to implement and control. However, battery to DC bus mode has multi-power processing stages. In the Type II-IIB converter, the first converter that connects the PV to the DC bus is a synchronous buck converter and the second converter is a bidirectional buck-boost converter connecting the battery to the DC bus as shown in Fig. 4.1(b). It has a single power processing in PV to DC bus, battery to DC bus, and PV to battery and DC bus modes. Furthermore, it is easy to implement and control. However, the disadvantage of this circuit is having multi-power processing stages in PV to battery mode. The principle of operation of all modes is first studied, followed by a steady state analysis. The converters are assumed to operate in continuous conduction mode (CCM).

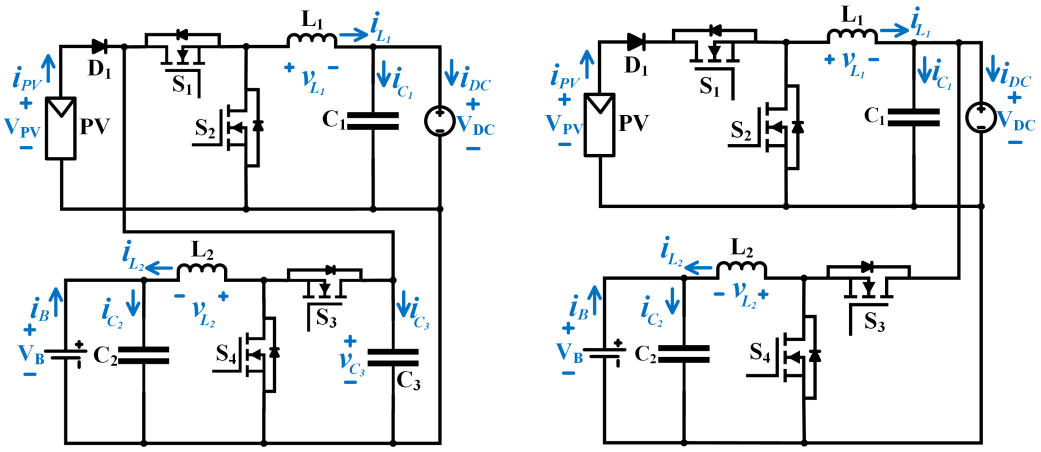

(a) Type II-IIA. (b) Type II-IIB.

Fig 4.1: The TPC circuits.

4.2.1 Principles of Operation and Modes Analysis

The presented TPC has seven modes of operation. These modes are shown in Fig. 4.2 and discussed in detail as below:

1. **PV to DC bus:** This mode is activated when the PV power supplies the DC bus only as the battery is fully charged or preset maximum State of Charge (SoC).

2. **PV to battery:** This mode is activated when the battery is charged by the PV source at no load condition.

3. **PV to DC bus and battery:** This mode is activated when the PV has sufficient power to supply the DC bus and the battery. The system now operates as a SIDO converter.

4. **PV and battery to DC bus:** This mode is activated when the DC bus requires more power than the PV source can generate. Therefore, the battery should provide the remaining power to the DC bus. The converter is working as a DISO converter.

5. **PV and DC bus to battery:** This mode is activated when the battery is low in SoC but the PV source alone is not sufficient to charge the battery at the rated current. Therefore, The converter is working as a DISO converter.

6. **Battery to DC bus:** This mode is activated when the PV source is unable to supply power to the DC bus during night time or under heavily shaded condition.

7. **DC bus to Battery:** This mode is activated when the PV is unable to supply power to the load during night time or under heavily shaded condition. In addition, the battery is low in SoC and would require charging from the DC Bus.

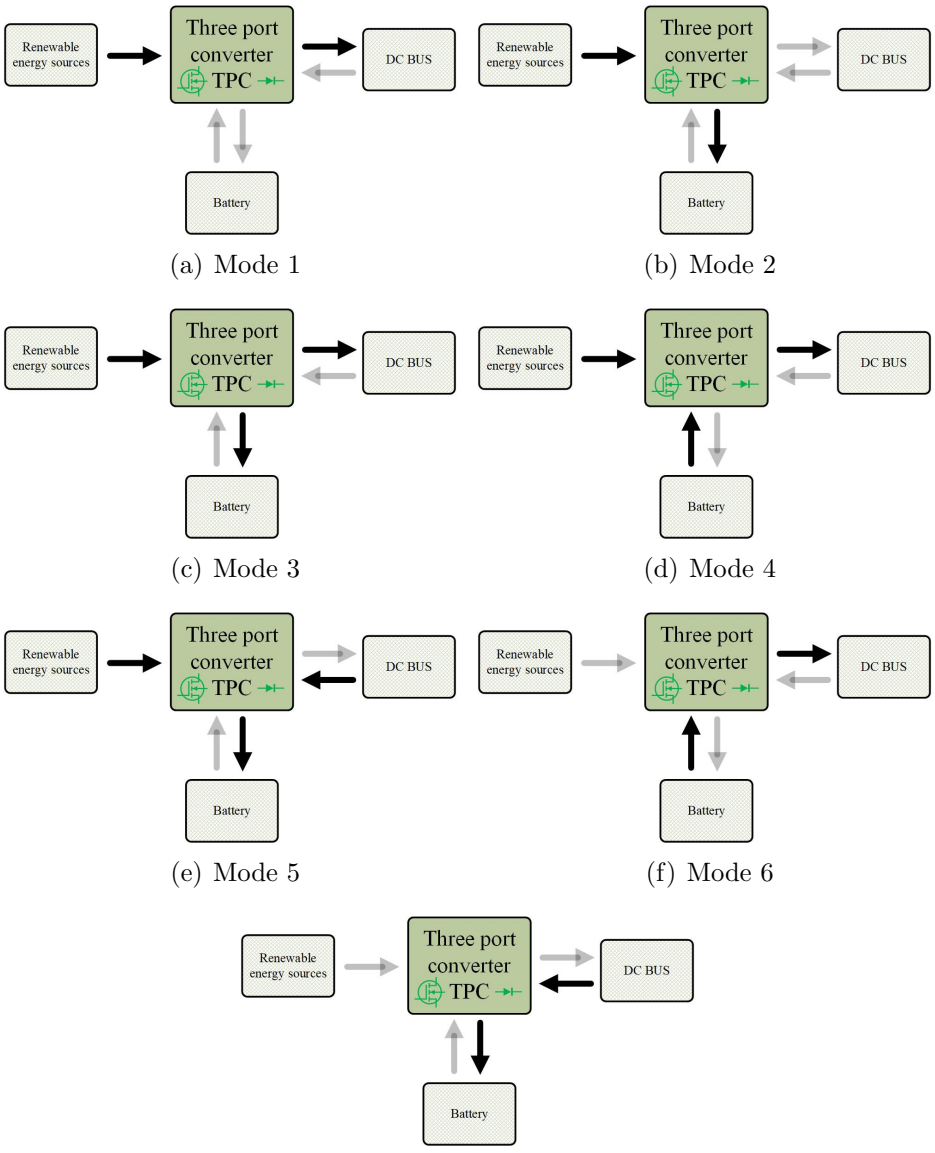

(a) Mode 1 (b) Mode 2

(c) Mode 3 (d) Mode 4

(e) Mode 5 (f) Mode 6

(g) Mode 7

Fig 4.2: Power flow diagram of all modes.

4.2.2 Type II-IIA Steady-State Analysis

Here, S_1 and S_2 are working as one pair and S_3 and S_4 as another pair. The duty ratio between S_1 and S_3 is depending on the voltage ratio between the DC bus and the battery. When S_1 is turned ON while S_2 is OFF, L_1 starts to charge from the PV source and when S_1 is turned OFF, L_1 starts to discharge. Similarly, when S_3 is turned ON while S_4 is OFF, L_2 starts to charge and vice versa.

1. **PV to DC bus:** The TPC is working as a SISO operation between the PV

source and the DC bus where the battery is idle in this case. S_1 and S_2 are working in a complementary manner while S_3 and S_4 are OFF. This operating mode has two switching states, as shown in Fig. 4.3 and discussed below:

State I $[t_0 < t < t_1]$: S_1 is turned ON while S_2 is OFF, L_1 starts to charge from the PV source and C_3 is discharging. D_1 is forward biased as shown in Fig. 4.3(a). The voltage across L_1 is given by $v_{L_1} = V_{PV} - V_{DC}$. This mode ends when S_1 turns OFF at $t = t_1$.

State II $[t_1 < t < t_2]$: S_1 is OFF and S_2 is ON where L_1 starts to discharge into the DC bus via S_2, as shown in Fig. 4.3(b). The voltage across L_1 is given by $v_{L_1} = -V_{DC}$. The current from the PV source is charging the capacitor C_3. This mode ends when S_2 turns OFF at $t = t_2$.

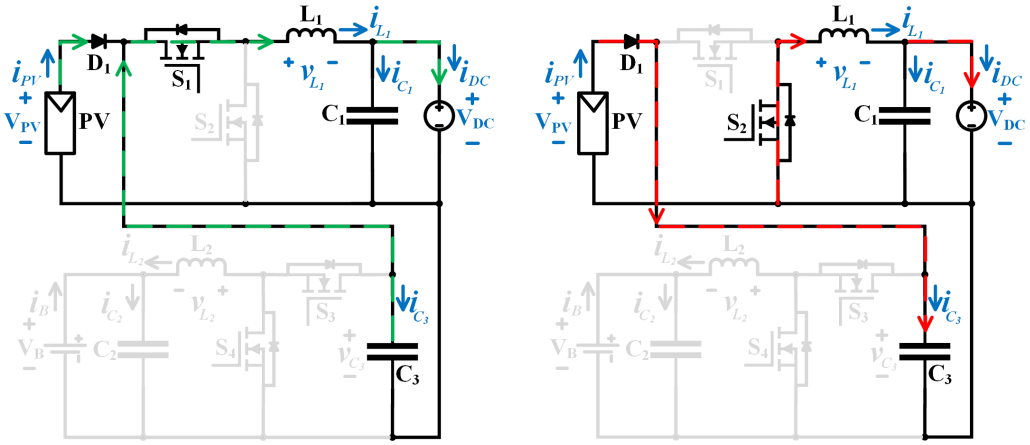

(a) State I (b) State II

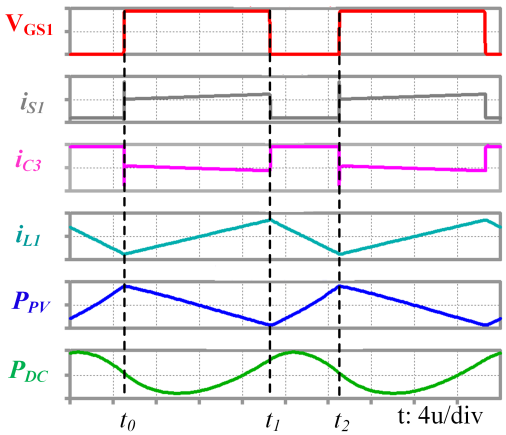

(c) Waveforms

Fig 4.3: Type II-IIA circuit Mode 1 SISO when no battery is connected.

2. **PV to battery:** The TPC is working as a SISO converter where the DC bus is idle. S_3 and S_4 are receiving PWM signal and working in a complementary manner while S_1 and S_2 are OFF. This operating mode has two switching states, as shown in Fig. 4.4 and discussed below:

   State I $[t_0 < t < t_1]$: S_3 is turned ON while S_4 is OFF, L_2 starts to charge from the PV source and C_3 is discharging. D_1 is forward biased as shown in Fig. 4.4(a). The voltage across L_2 is given by $v_{L_2} = V_{PV} - V_B$. This mode ends when S_3 turns OFF at $t = t_1$.

   State II $[t_1 < t < t_2]$: S_3 is OFF and S_4 is ON where L_2 starts to discharge into the battery via S_4, as shown in Fig. 4.4(b). The voltage across L_2 is given

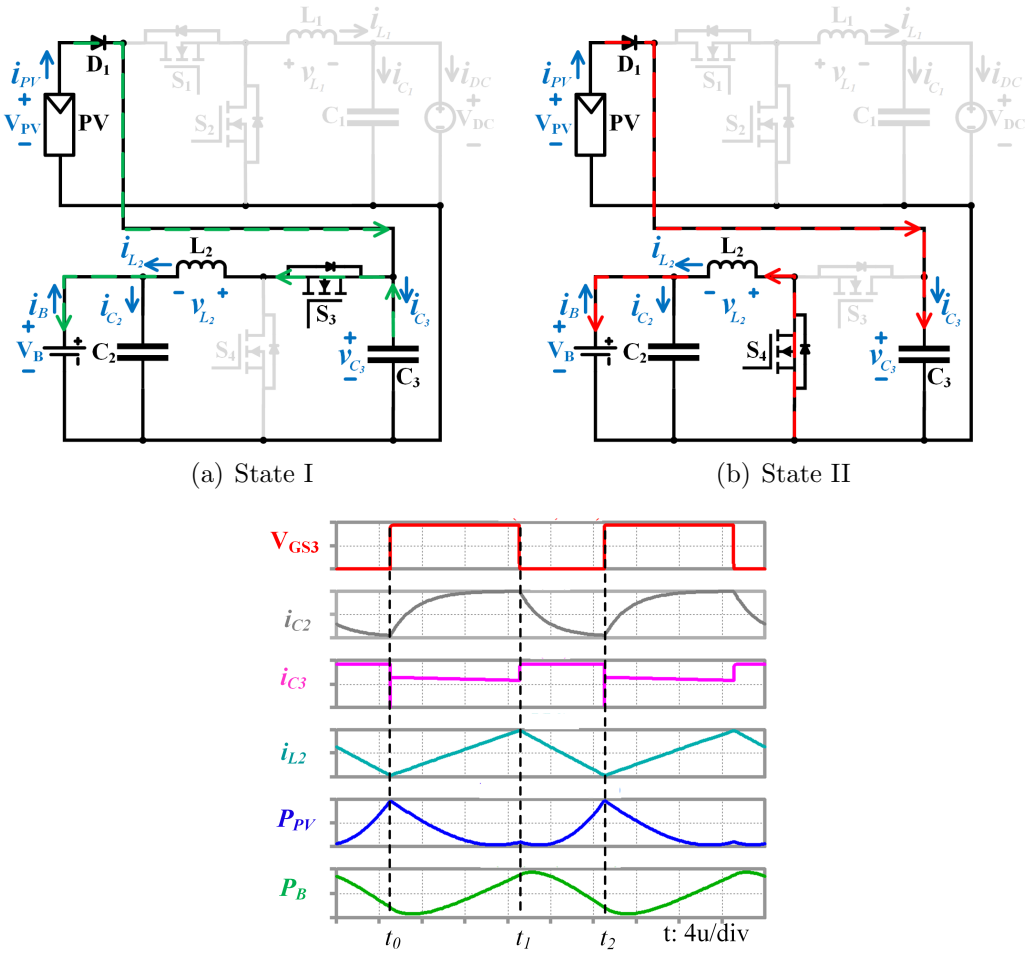

(a) State I (b) State II

(c) Waveforms

Fig 4.4: Type II-IIA circuit Mode 2 SISO when no DC bus is connected.

by $v_{L_2} = -V_B$. The current of PV source is charging the capacitor C_3. This mode ends when S_4 turns OFF at $t = t_2$.

3. **PV to DC bus and battery:** The system now operates as a SIDO converter. The duty ratio between S_1 and S_3 is depending on the voltage ratio between the DC bus and the battery given in (4.3). This operating mode has four switching states, as shown in Fig. 4.5 and discussed below:

   State I $[t_0 < t < t_1]$: S_1 and S_4 are turned ON while S_2, S_3 are OFF. PV starts to charge L_1 and C_3. In addition, L_2 starts to discharge into the battery via S_4, as shown in Fig. 4.5(a). The voltage across L_1 is given by $v_{L_1} = V_{PV} - V_{DC}$ and that across L_2 is given by $v_{L_2} = -V_B$. This mode ends when S_3 turns ON at $t = t_1$.

   State II $[t_1 < t < t_2]$: S_1 and S_3 are turned ON while S_2, S_4 are OFF, PV continues to charge L_1. In addition, L_2 starts to charge from the PV source and C_3, as shown in Fig. 4.5(b). The voltage across L_1 is given by $v_{L_1} = V_{PV} - V_{DC}$ and across L_2 is given by $v_{L_2} = V_{PV} - V_B$. This mode ends when S_1 turns OFF at $t = t_2$.

   State III $[t_2 < t < t_3]$: S_2 and S_3 are turned ON while S_1, S_4 are OFF, L_1 starts to discharge to the DC bus via S_2. In addition, the PV source starts to charge L_2 and C_3, as shown in Fig. 4.5(c). The voltage across L_1 is given by $v_{L_1} = -V_{DC}$ and across L_2 is given by $v_{L_2} = V_{PV} - V_B$. This mode ends when S_3 turns OFF at $t = t_3$.

   State IV $[t_3 < t < t_4]$: S_2 and S_4 are turned ON while S_1, S_3 are OFF. L_1 continues to discharge into the DC bus. In addition, L_2 start to discharge into the battery and the PV source starts to charge C_3, as shown in Fig. 4.5(d). The voltage across L_1 is given by $v_{L_1} = -V_{DC}$ and across L_2 is given by $v_{L_2} = -V_B$. This mode ends when S_1 turns ON at $t = t_4$. The relevant steady-state equations are:

$$V_{DC} = V_{PV} d_1 \tag{4.1}$$

$$V_B = V_{PV} d_3 \tag{4.2}$$

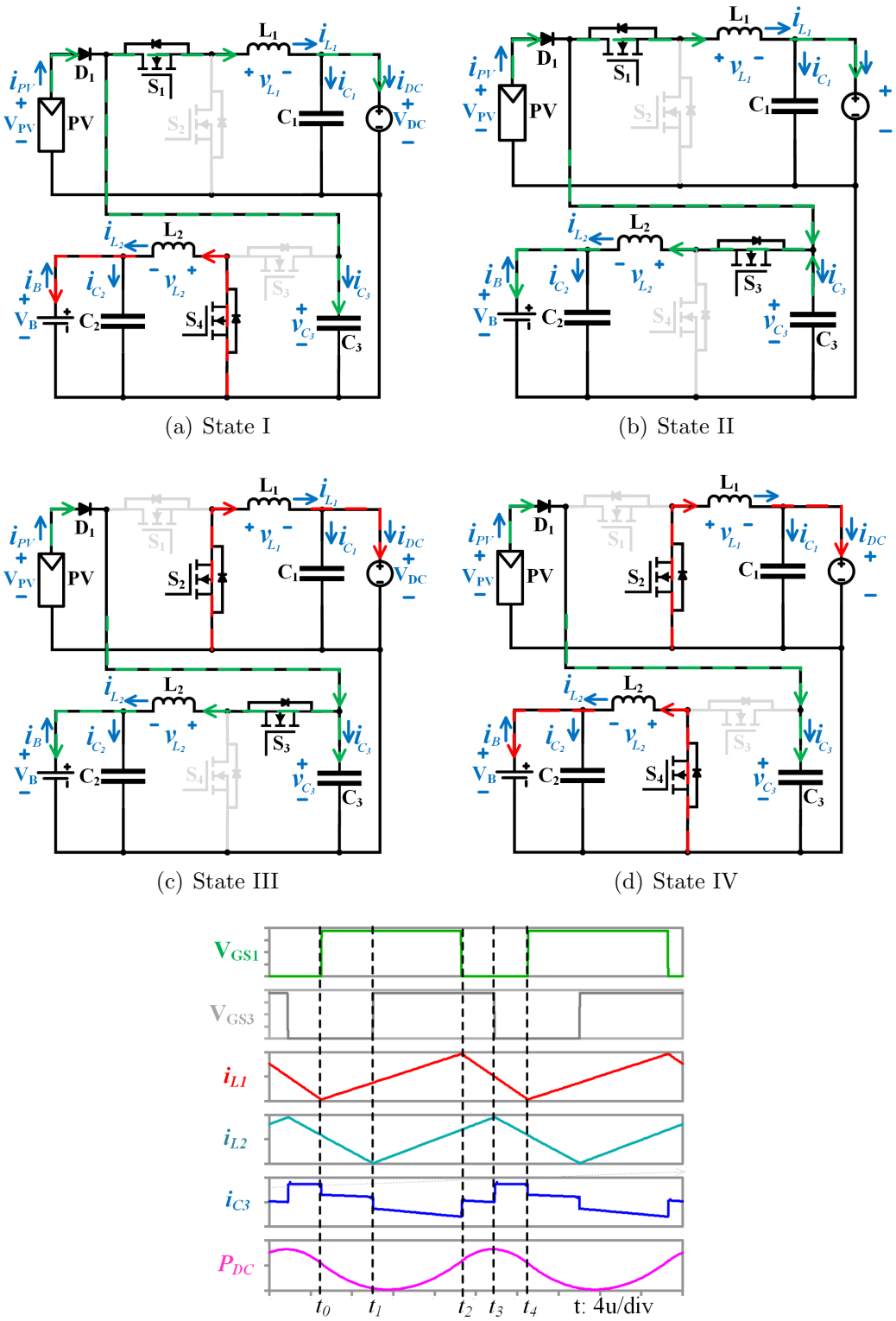

(a) State I

(b) State II

(c) State III

(d) State IV

(e) LTspice waveforms

Fig 4.5: Type II-IIA circuit Mode 3 SIDO.

$$\frac{V_{DC}}{V_B} = \frac{d_1}{d_3} \tag{4.3}$$

$$I_{PV} = d_1 I_{DC} + d_3 I_B \tag{4.4}$$

4. **PV and battery to DC bus**: The TPC is working as a DISO converter. All switches are working in this mode. However, the duty ratio will be higher than Mode 3. This operating mode has four switching states, as shown in Fig. 4.6 and discussed below:

   State I $[t_0 < t < t_1]$: S_1 and S_4 are turned ON while S_2, S_3 are OFF, PV source and C_3 starts to charge L_1. In addition, L_2 starts to charge from battery via S_4 as shown in Fig. 4.6(a). The voltage across L_1 is given by $v_{L_1} = V_{PV} - V_{DC}$ and across L_2 is given by $v_{L_2} = -V_B$. This mode ends when S_3 turns ON at $t = t_1$.

   State II $[t_1 < t < t_2]$: S_1 and S_3 are turned ON while S_2, S_4 are OFF, L_1 continues to charge from the PV source and the remains current from charging C_3. In addition, L_2 starts to discharge as shown in Fig. 4.6(b). The voltage across L_1 is given by $v_{L_1} = V_{PV} - V_{DC}$ and across L_2 is given by $v_{L_2} = V_{PV} - V_B$. This mode ends when S_1 turns OFF at $t = t_2$.

   State III $[t_2 < t < t_3]$: S_2 and S_3 are turned ON while S_1, S_4 are OFF, L_1 starts to discharge into DC bus via S_2. In addition, PV source and battery start to charge C_3 as shown in Fig. 4.6(c). The voltage across L_1 is given by $v_{L_1} = -V_{DC}$ and across L_2 is given by $v_{L_2} = V_{PV} - V_B$. This mode ends when S_3 turns OFF at $t = t_3$.

   State IV $[t_3 < t < t_4]$: S_2 and S_4 are turned ON while S_1, S_3 are OFF, L_1 continues to discharge to the DC bus. In addition, L_2 start to charge again from the battery and PV source start to charge C_3 only as shown in Fig. 4.6(d). The voltage across L_1 is given by $v_{L_1} = -V_{DC}$ and across L_2 is given by $v_{L_2} = -V_B$. This mode ends when S_1 turns ON at $t = t_4$. The relevant steady-state equations are:

$$V_{DC} = V_{PV} d_1 \tag{4.5}$$

$$V_B = V_{PV} d_3 \tag{4.6}$$

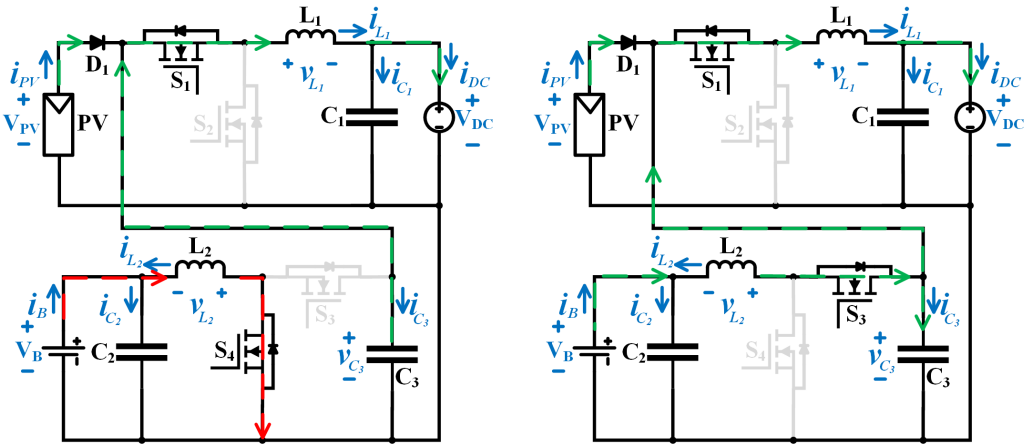

(a) State I (b) State II

(c) State III (d) State IV

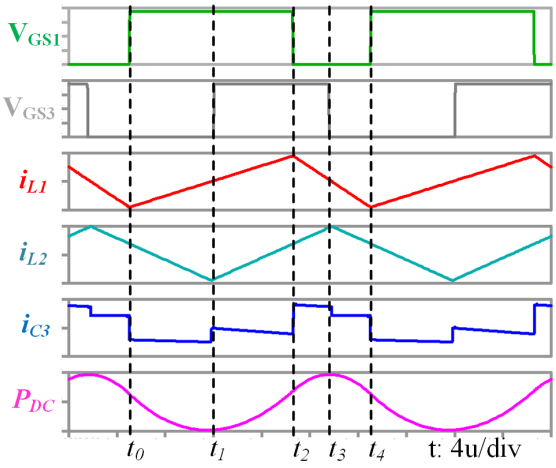

(e) LTspice waveforms

Fig 4.6: Type II-IIA circuit Mode 4 DISO.

$$I_{DC} = \frac{I_{PV}}{d_1} + \frac{d_3}{d_1} I_B \tag{4.7}$$

5. **PV and DC bus to battery**: The TPC is working as a DISO converter. All switches are active. However, the duty ratio will be lower than in Mode 3. This operating mode has four switching states, as shown in Fig. 4.7 and discussed below:

   State I $[t_0 < t < t_1]$: S_1 and S_4 are turned ON while S_2, S_3 are OFF, PV source and DC bus starts to charge C_3. In addition, L_2 starts to discharge to the battery via S_4 as shown in Fig. 4.7(a). This mode ends when S_3 turns ON at $t = t_1$.

   State II $[t_1 < t < t_2]$: S_1 and S_3 are turned ON while S_2, S_4 are OFF, L_1 continues to discharge with the PV source into the battery. In addition, L_2 starts to charge as shown in Fig. 4.7(b). This mode ends when S_1 turns OFF at $t = t_2$.

   State III $[t_2 < t < t_3]$: S_2 and S_3 are turned ON while S_1, S_4 are OFF, L_1 starts to charge from the DC bus via S_2. In addition, PV source and C_3 start to charge L_2 as shown in Fig. 4.7(c). This mode ends when S_3 turns OFF at $t = t_3$.

   State IV $[t_3 < t < t_4]$: S_2 and S_4 are turned ON while S_1, S_3 are OFF, L_1 continues to charge from the DC bus. In addition, L_2 starts to discharge again to the battery and the PV source start to charge C_3, as shown in Fig. 4.7(d). This mode ends when S_1 turns ON at $t = t_4$. The relevant steady-state equations are:

$$V_{PV} = \frac{V_{DC}}{d_1} \tag{4.8}$$

$$V_B = V_{PV} d_3 \tag{4.9}$$

$$I_B = \frac{I_{PV}}{d_3} + \frac{d_1}{d_3} I_{DC} \tag{4.10}$$

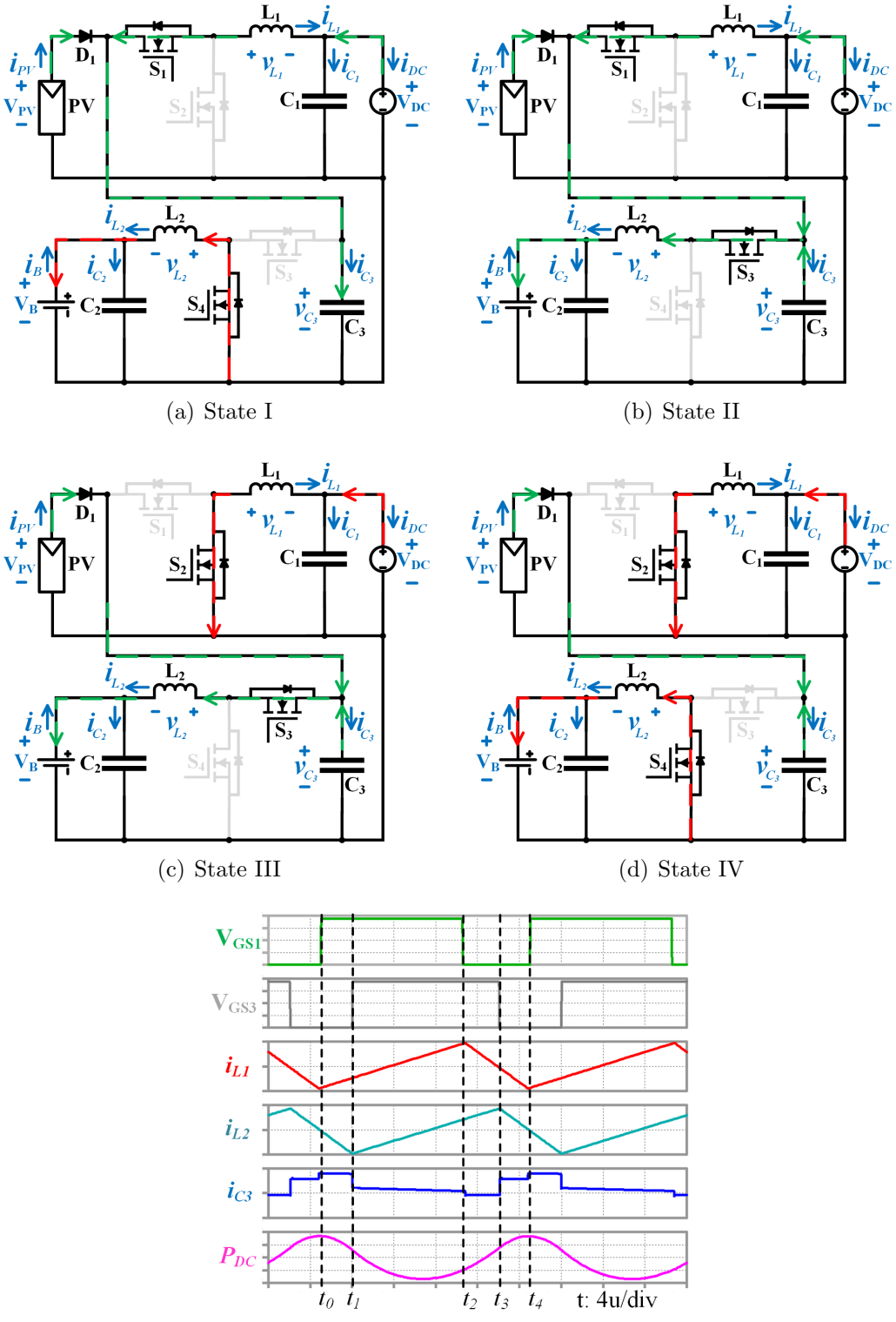

(a) State I

(b) State II

(c) State III

(d) State IV

(e) LTspice waveforms

Fig 4.7: Type II-IIA circuit Mode 5 DISO.

6. **Battery to DC bus**: The TPC is working as a SISO converter between the battery and the DC bus. S_3 and S_4 are working as a pair and S_1 and S_2 are ON

and OFF respectively to maintain a single conversion stage. This operating mode has two switching states, as shown in Fig. 4.8 and discussed below:

State I $[t_0 < t < t_1]$: S_4 is turned ON while S_3 is OFF, C_3 starts to charge L_1. In addition, L_2 starts to charge from the battery via S_4 as shown in Fig. 4.8(a). The voltage across L_1 is given by $v_{L_1} = V_{C_3} - V_{DC}$ and across L_2 is given by $v_{L_2} = -V_B$. This mode ends when S_4 turns OFF at $t = t_1$.

State II $[t_1 < t < t_2]$: S_3 is turned ON while S_4 is OFF, L_1 continues to charge from the battery. In addition, L_2 starts to discharge as shown in Fig. 4.8(b). The voltage across L_1 is given by $v_{L_1} = V_{C_3} - V_{DC}$ and across L_2 is given by $v_{L_2} = V_{C_3} - V_B$. This mode ends when S_3 turns OFF at $t = t_2$.

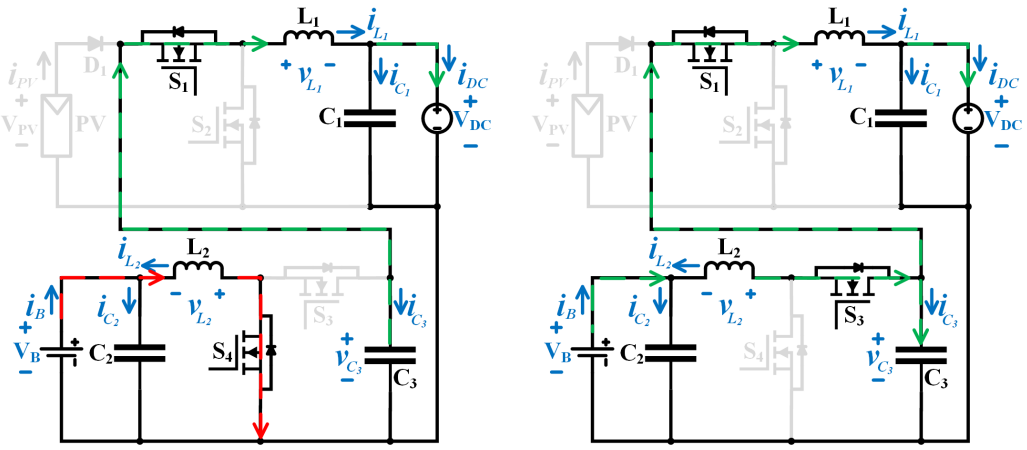

(a) State I (b) State II

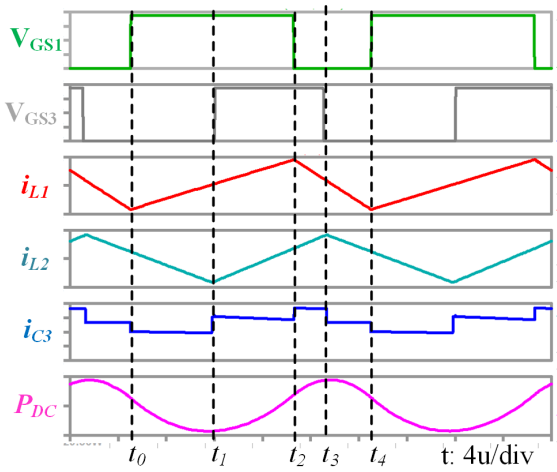

(c) LTspice waveforms

Fig 4.8: Type II-IIA circuit Mode 6 SISO.

7. **DC bus to battery**: The TPC is working as a SISO converter and will be the same as Mode 3. This operating mode has two switching states, as shown in Fig. 4.9 and discussed below:

   State I $[t_0 < t < t_1]$: S_1 and S_4 are turned ON while S_2, S_3 are OFF, the DC bus starts to charge C_3. In addition, L_2 starts to discharge to the battery via S_4 as shown in Fig. 4.9(a). This mode ends when S_3 turns ON at $t = t_1$.

   State II $[t_1 < t < t_2]$: S_1 and S_3 are turned ON while S_2, S_4 are OFF, L_1 continues to discharge to C_3 and the battery. In addition, L_2 starts to charge as shown in Fig. 4.9(b). This mode ends when S_1 turns OFF at $t = t_2$.

The switching patterns to achieve all seven modes of operation are shown in Table

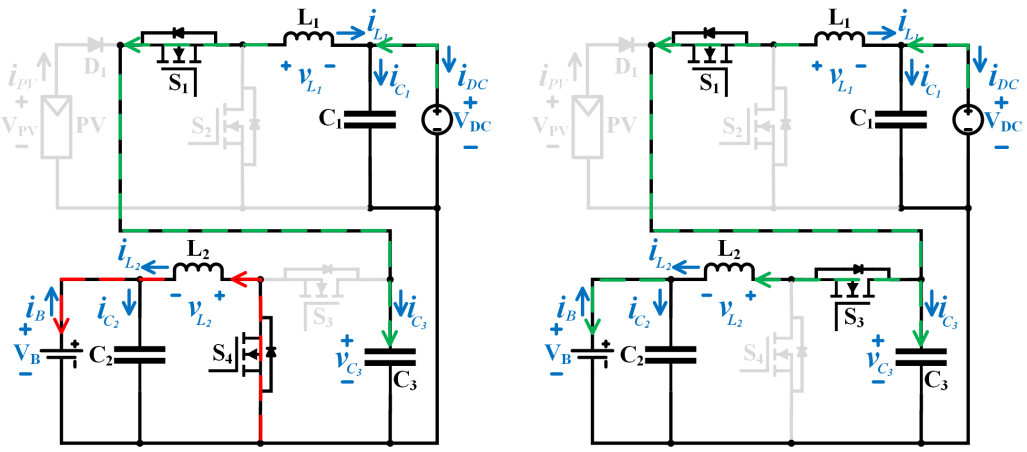

(a) State I (b) State II

(c) LTspice waveforms

Fig 4.9: Type II-IIA circuit Mode 7 SISO.

4.2. Although there are four switches in the converter, only two sets of PWM are required to implement all modes.

Table 4.2: Switching Look-up Table for Different Modes of Converter in Fig. 4.1(a)

Modes	Power	Active Components	State	Switch state ON	Switch state OFF	Control	Duty condition	Fig
PV to DC bus	$P_{pv} = P_{DC}$	D_1, S_1, S_2, L_1, C_1 & C_3	I	S_1^*	S_2^*	MPPT or OVR	–	Fig. 4.3(a)
			II	S_2^*	S_1^*	(S_1, S_2)		Fig. 4.3(b)
PV to battery	$P_{pv} = P_B$	D_1, S_3, S_4, L_2, C_2 & C_3	I	S_3^*	S_4^*	MPPT or BP	–	Fig. 4.4(a)
			II	S_4^*	S_3^*	(S_3, S_4)		Fig. 4.4(b)
PV to DC bus and battery	$P_{pv} = P_{DC} + P_B$	All active	I	S_1^*, S_4^*	S_2^*, S_3^*			Fig. 4.5(a)
			II	S_1^*, S_3^*	S_2^*, S_4^*	MPPT & OVR	$\frac{D_1}{D_3} \approx \frac{V_{DC}}{V_B}$	Fig. 4.5(b)
			III	S_2^*, S_3^*	S_1^*, S_4^*	(S_3, S_4) (S_1, S_2)		Fig. 4.5(c)
			IV	S_2^*, S_4^*	S_1^*, S_3^*			Fig. 4.5(d)
PV and battery to DC bus	$P_{pv} + P_B = P_{DC}$	All active	I	S_1^*, S_4^*	S_2^*, S_3^*			Fig. 4.6(a)
			II	S_1^*, S_3^*	S_2^*, S_4^*	MPPT & OVR	$\frac{D_1}{D_3} \geqslant \frac{V_{DC}}{V_B}$	Fig. 4.6(b)
			III	S_2^*, S_3^*	S_1^*, S_4^*	(S_3, S_4) (S_1, S_2)		Fig. 4.6(c)
			IV	S_2^*, S_4^*	S_1^*, S_3^*			Fig. 4.6(d)
PV and DC bus to battery	$P_{pv} + P_{DC} = P_B$	All active	I	S_1^*, S_4^*	S_2^*, S_3^*			Fig. 4.7(a)
			II	S_1^*, S_3^*	S_2^*, S_4^*	MPPT & OVR	$\frac{D_1}{D_3} \leqslant \frac{V_{DC}}{V_B}$	Fig. 4.7(b)
			III	S_2^*, S_3^*	S_1^*, S_4^*	(S_3, S_4) (S_1, S_2)		Fig. 4.7(c)
			IV	S_2^*, S_4^*	S_1^*, S_3^*			Fig. 4.7(d)
battery to DC bus	$P_B = P_{DC}$	All active except D_1, S_2	I	S_1°, S_4^*	S_3^*	BP or OVR	–	Fig. 4.8(a)
			II	S_1°, S_3^*	S_4^*	(S_3, S_4)		Fig. 4.8(b)
DC bus to battery	$P_{DC} = P_B$	All active except D_1, S_2	I	S_1°, S_4^*	S_3^*	BP	–	Fig. 4.9(a)
			II	S_1°, S_3^*	S_4^*	(S_3, S_4)		Fig. 4.9(b)

* Switch operates in PWM ° Switch is fully ON

4.2.3 Type II-IIB Steady-State Analysis

1. **PV to DC bus:** S_1 and S_2 are working in a complementary manner while S_3 and S_4 are OFF. This operating mode has two switching states, as shown in Fig. 4.10 and discussed below:

   State I $[t_0 < t < t_1]$: S_1 is turned ON while S_2 is OFF. L_1 starts to charge from the PV source. D_1 is forward biased as shown in Fig. 4.10(a). The voltage across L_1 is given by $v_{L_1} = V_{PV} - V_{DC}$. This mode ends when S_1 turns OFF at $t = t_1$.

   State II $[t_1 < t < t_2]$: S_1 is OFF and S_2 is ON where L_1 starts to discharge into the DC bus via S_2 as shown in Fig. 4.10(b). The voltage across L_1 is given by $v_{L_1} = -V_{DC}$. The current from the PV source is charging the capacitor C_3. This mode ends when S_2 turns OFF at $t = t_2$.

2. **PV to battery:** S_1 and S_2 are receiving the PWM signal and working in a complementary manner while S_3 is ON and S_4 is OFF to maintain a single conversion stage. This operating mode has two switching states, as shown in

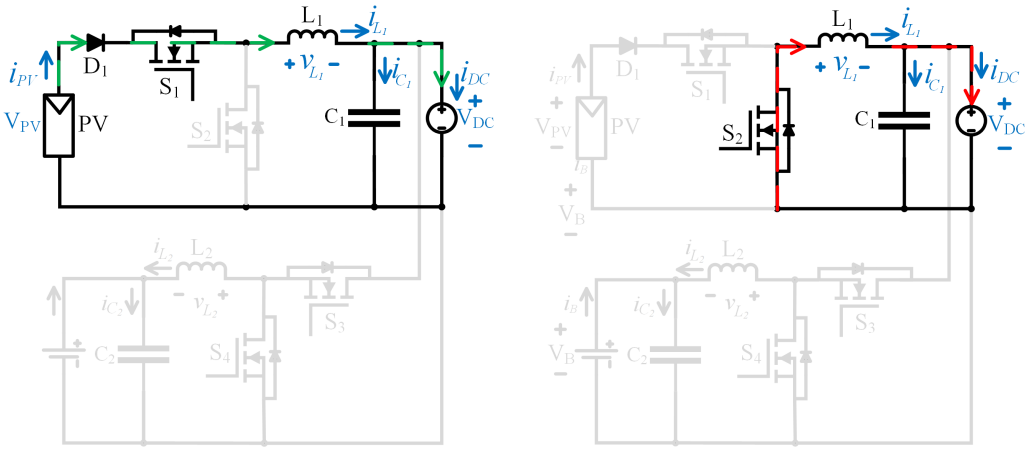

(a) State I (b) State II

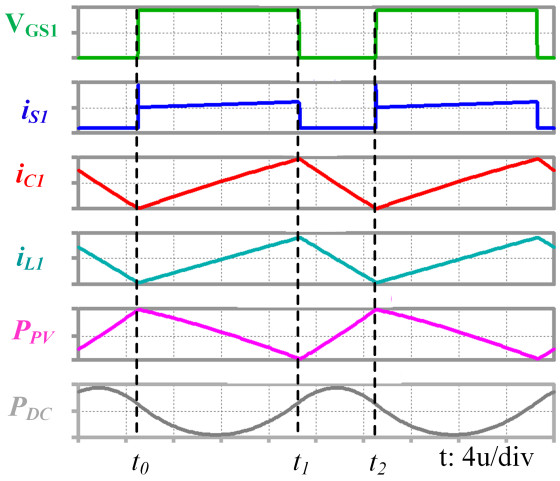

(c) Waveforms

Fig 4.10: Type II-IIB circuit Mode 1 SISO when no battery is connected.

Fig. 4.11 and discussed below:

State I $[t_0 < t < t_1]$: S_1 is turned ON while S_2 is OFF, L_1 starts to charge from the PV source. D_1 is forward biased as shown in Fig. 4.11(a). The voltage across L_1 is given by $v_{L_1} = V_{PV} - V_B$. This mode ends when S_1 turns OFF at $t = t_1$.

State II $[t_1 < t < t_2]$: S_1 is OFF and S_2 is ON where L_1 starts to discharge into the battery via S_2, as shown in Fig. 4.11(b). The voltage across L_1 is given by $v_{L_1} = -V_{DC}$. This mode ends when S_4 turns OFF at $t = t_2$.

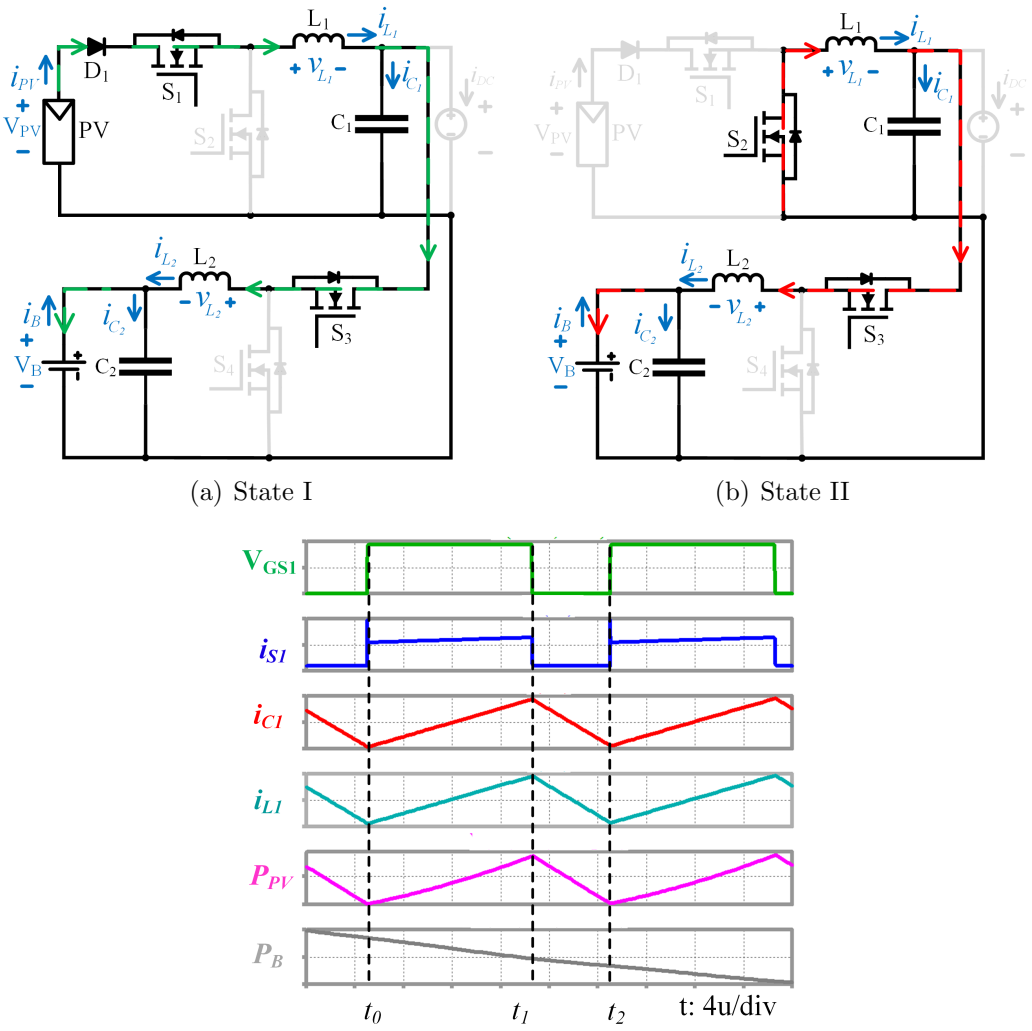

(a) State I (b) State II

(c) Waveforms

Fig 4.11: Type II-IIB circuit Mode 2 SISO when no DC bus is connected.

3. **PV to DC bus and battery**: The system now operates as a SIDO converter. The ratio between the DC bus and the battery is given in (4.14). This operating mode has four switching states, as shown in Fig. 4.12 and discussed below:

   State I $[t_0 < t < t_1]$: S_1 and S_4 are turned ON while S_2, S_3 are OFF. The PV source starts to charge L_1. In addition, L_2 starts to discharge into the battery via S_4, as shown in Fig. 4.12(a). The voltage across L_1 is given by $v_{L_1} = V_{PV} - V_{DC}$ and across L_2 is given by $v_{L_2} = -V_B$. This mode ends when S_3 turns ON at $t = t_1$.

   State II $[t_1 < t < t_2]$: S_1 and S_3 are turned ON while S_2, S_4 are OFF. The

PV source continues to charge L_1. In addition, L_2 starts to charge from the PV source, as shown in Fig. 4.12(b). The voltage across L_1 is given by $v_{L_1} =$

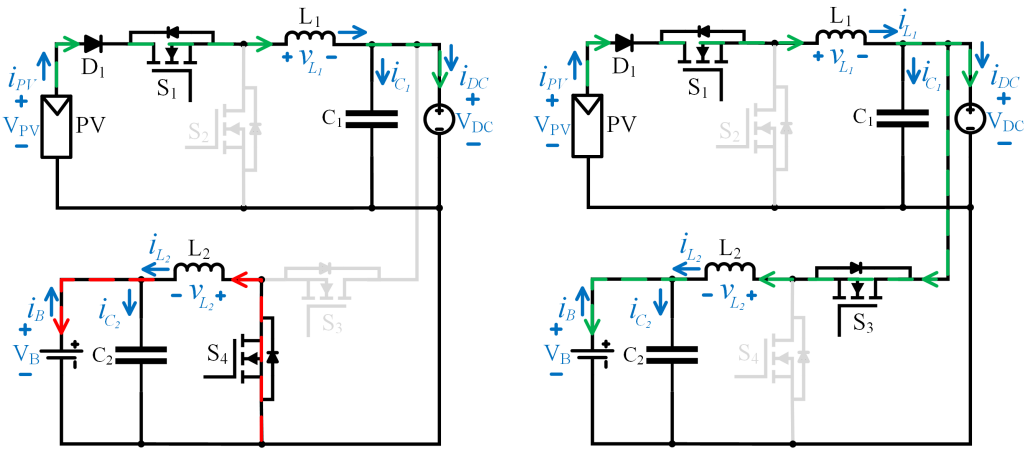

(a) State I

(b) State II

(c) State III

(d) State IV

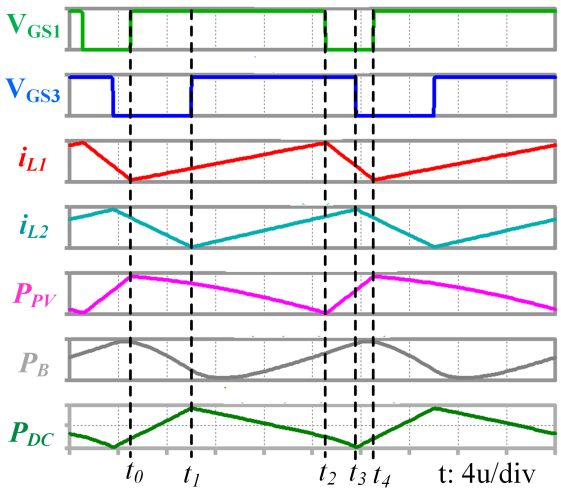

(e) Waveforms

Fig 4.12: Type II-IIB circuit Mode 3 SIDO.

$V_{PV} - V_{DC}$ and across L_2 is given by $v_{L_2} = V_{PV} - V_B$. This mode ends when S_1 turns OFF at $t = t_2$.

State III $[t_2 < t < t_3]$: S_2 and S_3 are turned ON while S_1, S_4 are OFF. L_1 starts to discharge to the DC bus and starts to charge L_2, as shown in Fig. 4.12(c). The voltage across L_1 is given by $v_{L_1} = -V_{DC}$ and across L_2 is given by $v_{L_2} = V_{PV} - V_B$. This mode ends when S_3 turns OFF at $t = t_3$.

State IV $[t_3 < t < t_4]$: S_2 and S_4 are turned ON while S_1, S_3 are OFF. L_1 continues to discharge into the DC bus. In addition, L_2 start to discharge into the battery, as shown in Fig. 4.12(d). The voltage across L_1 is given by $v_{L_1} = -V_{DC}$ and across L_2 is given by $v_{L_2} = -V_B$. This mode ends when S_1 turns ON at $t = t_4$. The relevant steady-state equations are:

$$V_{DC} = V_{PV} d_1 \tag{4.11}$$

$$V_B = V_{PV} d_1 d_3 \tag{4.12}$$

$$I_{PV} = d_1 (I_{DC} + d_3 I_B) \tag{4.13}$$

$$\frac{V_{DC}}{V_B} = \frac{1}{d_3} \tag{4.14}$$

4. **PV and battery to DC bus**: The TPC is working as a DISO converter. All switches are active. However, the duty ratio of these PWM signals are different from those in Mode 3. This operating mode has four switching states, as shown in Fig. 4.13 and discussed below:

   State I $[t_0 < t < t_1]$: S_1 and S_4 are turned ON while S_2, S_3 are OFF. The PV source starts to charge L_1. In addition, L_2 starts to charge from the battery via S_4, as shown in Fig. 4.13(a). The voltage across L_1 is given by $v_{L_1} = V_{PV} - V_{DC}$ and across L_2 is given by $v_{L_2} = -V_B$. This mode ends when S_3 turns ON at $t = t_1$.

   State II $[t_1 < t < t_2]$: S_1 and S_3 are turned ON while S_2, S_4 are OFF. L_1 continues to charge from the PV source. In addition, L_2 starts to discharge,

as shown in Fig. 4.13(b). The voltage across L_1 is given by $v_{L_1} = V_{PV} - V_{DC}$ and across L_2 is given by $v_{L_2} = V_{DC} - V_B$. This mode ends when S_1 turns

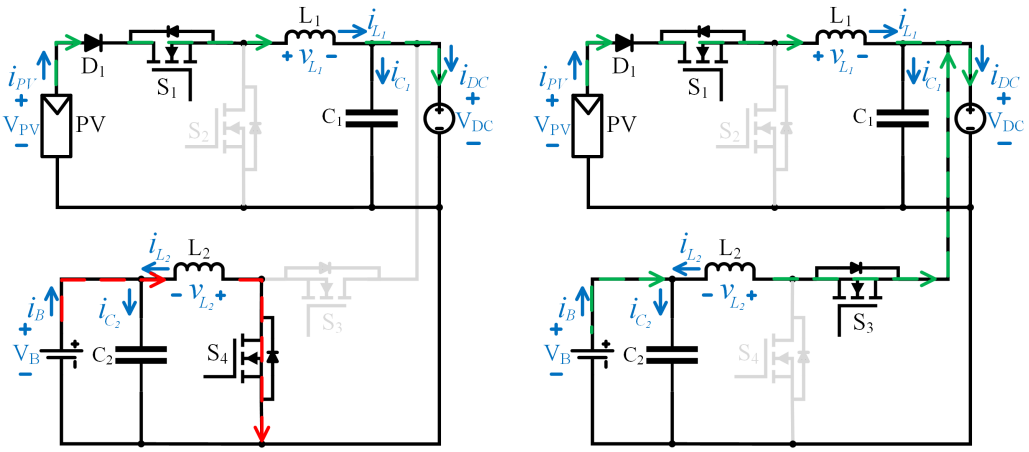

(a) State I (b) State II

(c) State III (d) State IV

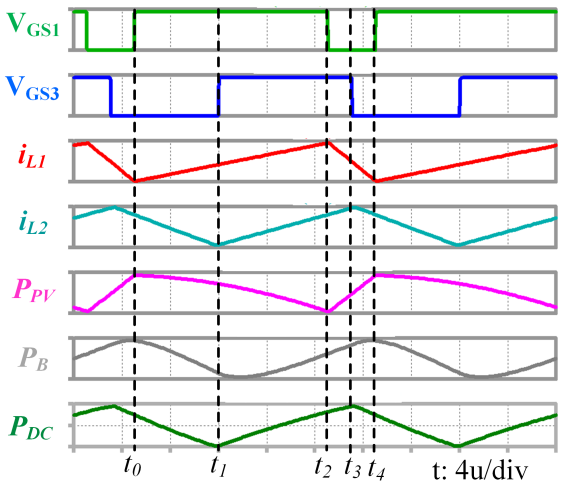

(e) Waveforms

Fig 4.13: Type II-IIB circuit Mode 4 DISO.

OFF at $t = t_2$.

State III $[t_2 < t < t_3]$: S_2 and S_3 are turned ON while S_1, S_4 are OFF. L_1 starts to discharge into the DC bus via S_2. In addition, the battery starts to charge the DC bus, as shown in Fig. 4.13(c). The voltage across L_1 is given by $v_{L_1} = -V_{DC}$ and across L_2 is given by $v_{L_2} = V_{PV} - V_{DC}$. This mode ends when S_3 turns OFF at $t = t_3$.

State IV $[t_3 < t < t_4]$: S_2 and S_4 are turned ON while S_1, S_3 are OFF. L_1 continues to discharge to the DC bus. In addition, L_2 starts to charge again from the battery, as shown in Fig. 4.13(d). The voltage across L_1 is given by $v_{L_1} = -V_{DC}$ and across L_2 is given by $v_{L_2} = -V_B$. This mode ends when S_1 turns ON at $t = t_4$. The steady-state equations are:

$$V_{DC} = V_{PV} d_1 \tag{4.15}$$

$$I_{DC} = \frac{I_{PV}}{d_1} + d_3 I_B \tag{4.16}$$

5. **PV and DC bus to battery**: The TPC is working as a DISO converter. All switches are active. This operating mode has four switching states, as shown in Fig. 4.14 and discussed below:

   State I $[t_0 < t < t_1]$: S_1 and S_4 are turned ON while S_2, S_3 are OFF. The PV source starts to charge L_1. In addition, L_2 starts to discharge to the battery via S_4, as shown in Fig. 4.14(a). This mode ends when S_3 turns ON at $t = t_1$.

   State II $[t_1 < t < t_2]$: S_1 and S_3 are turned ON while S_2, S_4 are OFF. The PV source continues to charge L_1 from PV source. In addition, the DC bus starts to charge L_2, as shown in Fig. 4.14(b). This mode ends when S_1 turns OFF at $t = t_2$.

   State III $[t_2 < t < t_3]$: S_2 and S_3 are turned ON while S_1, S_4 are OFF. L_1 starts to discharge with the DC bus into L_2, as shown in Fig. 4.14(c). This mode ends when S_3 turns OFF at $t = t_3$.

   State IV $[t_3 < t < t_4]$: S_2 and S_4 are turned ON while S_1, S_3 are OFF. L_1

continues to discharge into the DC bus. In addition, L_2 starts to discharge again to the battery, as shown in Fig. 4.14(d). This mode ends when S_1 turns

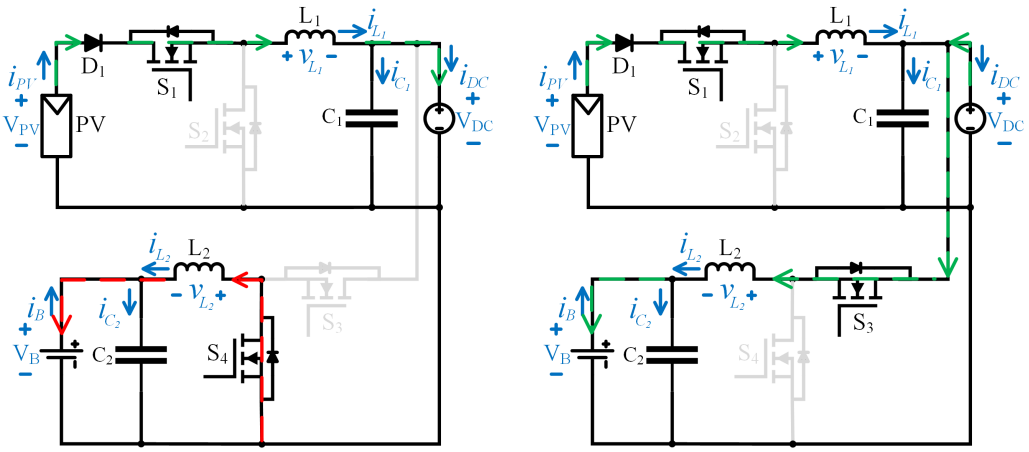

(a) State I (b) State II

(c) State III (d) State IV

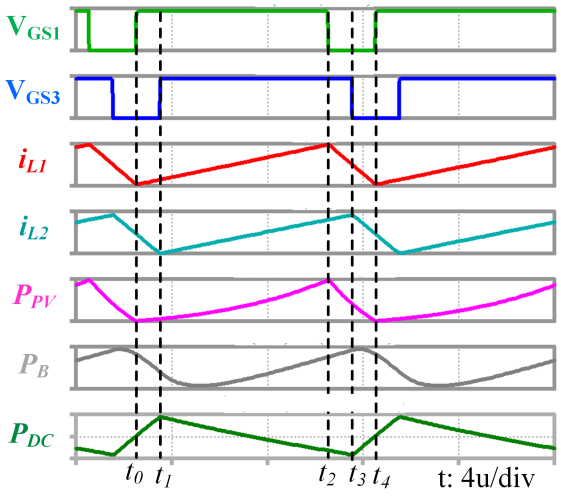

(e) Waveforms

Fig 4.14: Type II-IIB circuit Mode 5 DISO.

ON at $t = t_4$.

$$V_{DC} = V_{PV} d_1 \tag{4.17}$$

$$V_B = V_{PV} d_1 d_3 \tag{4.18}$$

$$I_B = \frac{\frac{I_{PV}}{d_1} + I_{DC}}{d_3} \tag{4.19}$$

6. **battery to DC bus**: The TPC is working between the battery and the DC bus as a SISO converter. This operating mode has two switching states, as shown in Fig. 4.15 and discussed below:

   State I $[t_0 < t < t_1]$: S_3 is turned ON while S_4 is OFF. L_2 starts to charge from the PV source and C_3 is discharging. D_1 is forward biased, as shown in

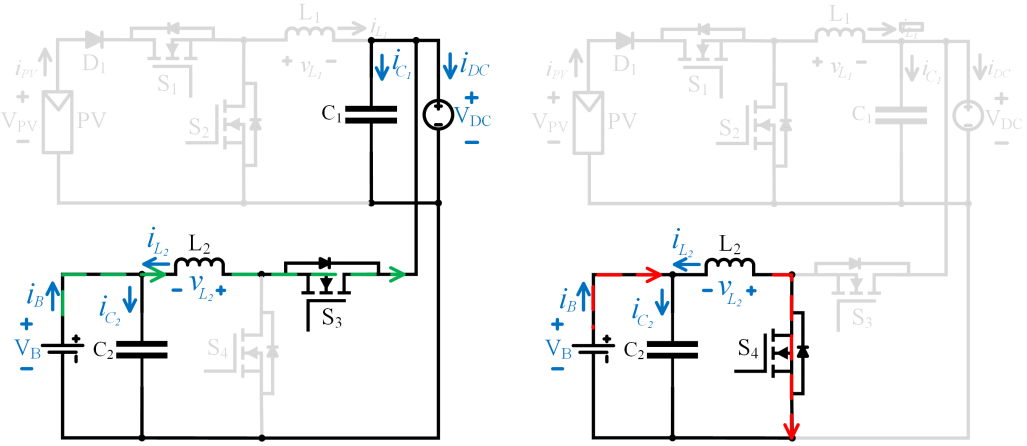

(a) State I (b) State II

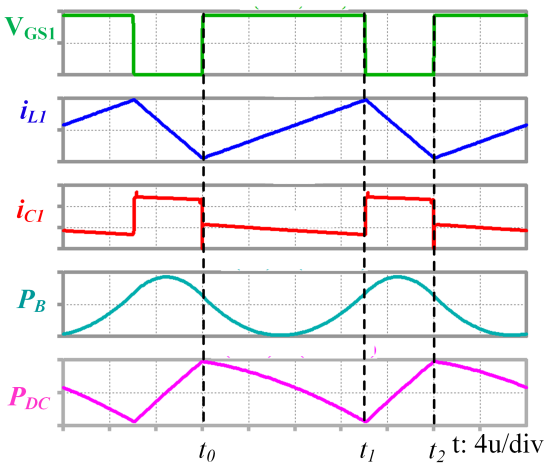

(c) Waveforms

Fig 4.15: Type II-IIB circuit Mode 6 SISO and no PV panel

Fig. 4.15(a). The voltage across L_2 is given by $v_{L_2} = V_B - V_{PV}$. This mode ends when S_3 turns OFF at $t = t_1$.

State II $[t_1 < t < t_2]$: S_3 is OFF and S_4 is ON where L_2 starts to discharge into the battery via S_4 as shown in Fig. 4.15(b). The voltage across L_2 is given by $v_{L_2} = V_B$. The Current of PV source is charging the capacitor C_3. This mode ends when S_4 turns OFF at $t = t_2$.

7. **DC bus to battery**: S_3 and S_4 are receiving the PWM signals and working in a complementary manner while S_1 and S_2 are OFF. This operating mode has two switching states, as shown in Fig. 4.16 and discussed below:

   State I $[t_0 < t < t_1]$: S_3 is turned ON while S_4 is OFF. L_2 starts to charge

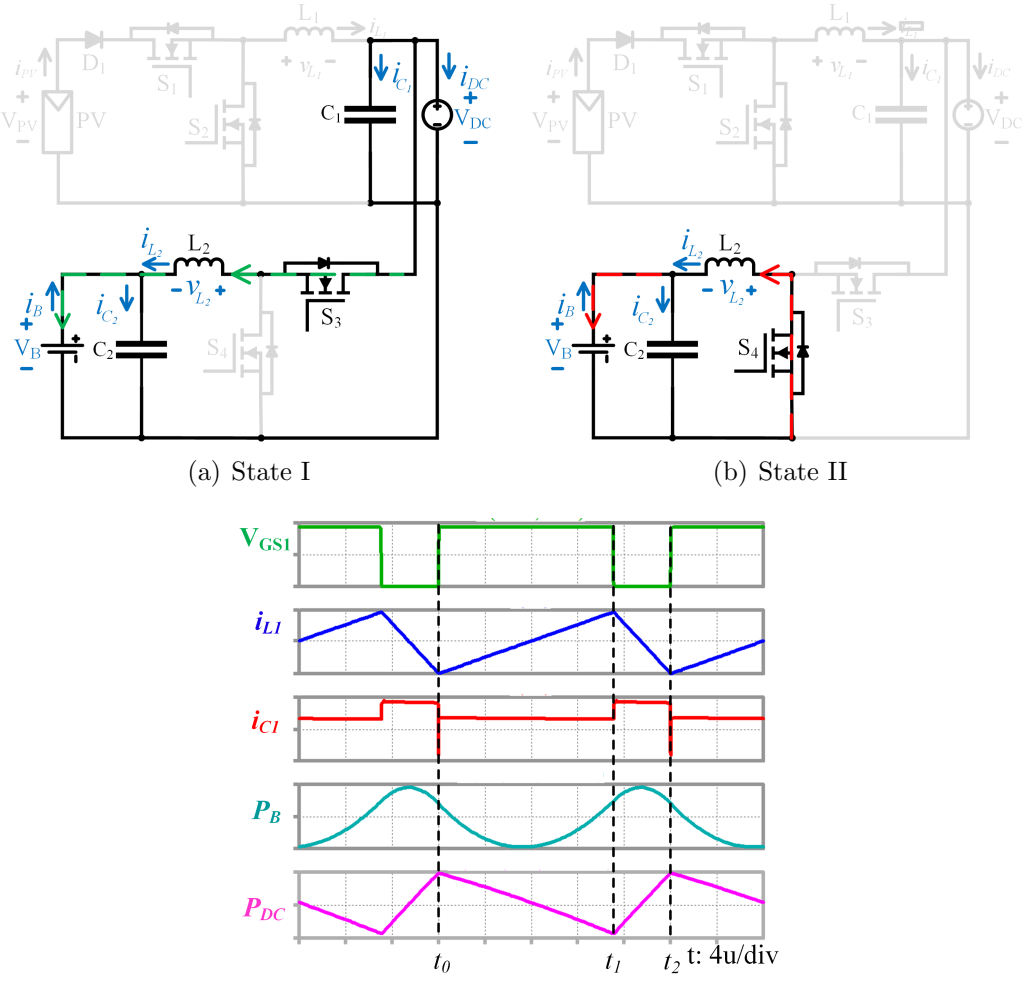

(a) State I (b) State II

(c) Waveforms

Fig 4.16: Type II-IIB circuit Mode 7 SISO and no PV panel

from the DC bus as shown in Fig. 4.16(a). The voltage across L_2 is given by $v_{L_2} = V_{PV} - V_B$. This mode ends when S_3 turns OFF at $t = t_1$.

State II $[t_1 < t < t_2]$: S_3 is OFF and S_4 is ON where L_2 starts to discharge into the battery via S_4 as shown in Fig. 4.16(b). The voltage across L_2 is given by $v_{L_2} = -V_B$. This mode ends when S_4 turns OFF at $t = t_2$.

The switching patterns to achieve all seven modes of operation are shown in Table 4.3.

Table 4.3: Switching Look-up Table for Different Modes of Converter in Fig. 4.1(b)

Modes	Power	Active Components	State	Switch state ON	Switch state OFF	Control	Duty condition	Fig
PV to DC bus	$P_{pv} = P_{DC}$	D_1, S_1, S_2, L_1 & C_1	I	S_1^*	S_2^*	OVR	–	Fig. 4.10(a)
			II	S_2^*	S_1^*	(S_1, S_2)		Fig. 4.10(b)
PV to battery	$P_{pv} = P_B$	All active except S_4	I	S_1^*, S_3°	S_2^*	MPPT or BP	–	Fig. 4.11(a)
			II	S_2^*, S_3°	S_1^*	(S_1, S_2)		Fig. 4.11(b)
PV to DC bus and battery	$P_{pv} = P_{DC} + P_B$	All active	I	S_1^*, S_4^*	S_2^*, S_3^*			Fig. 4.12(a)
			II	S_1^*, S_3^*	S_2^*, S_4^*	MPPT & OVR	$\frac{1}{D_3} \approx \frac{V_{DC}}{V_B}$	Fig. 4.12(b)
			III	S_2^*, S_3^*	S_1^*, S_4^*	(S_1, S_2) (S_3, S_4)		Fig. 4.12(c)
			IV	S_2^*, S_4^*	S_1^*, S_3^*			Fig. 4.12(d)
PV and battery to DC bus	$P_{pv} + P_B = P_{DC}$	All active	I	S_1^*, S_4^*	S_2^*, S_3^*			Fig. 4.13(a)
			II	S_1^*, S_3^*	S_2^*, S_4^*	MPPT & OVR	$\frac{1}{D_3} \geqslant \frac{V_{DC}}{V_B}$	Fig. 4.13(b)
			III	S_2^*, S_3^*	S_1^*, S_4^*	(S_1, S_2) (S_3, S_4)		Fig. 4.13(c)
			IV	S_2^*, S_4^*	S_1^*, S_3^*			Fig. 4.13(d)
PV and DC bus to battery	$P_{pv} + P_{DC} = P_B$	All active	I	S_1^*, S_4^*	S_2^*, S_3^*			Fig. 4.14(a)
			II	S_1^*, S_3^*	S_2^*, S_4^*	MPPT & OVR	$\frac{1}{D_3} \leqslant \frac{V_{DC}}{V_B}$	Fig. 4.14(b)
			III	S_2^*, S_3^*	S_1^*, S_4^*	(S_1, S_2) (S_3, S_4)		Fig. 4.14(c)
			IV	S_2^*, S_4^*	S_1^*, S_3^*			Fig. 4.14(d)
battery to DC bus	$P_B = P_{DC}$	S_3, S_4, L_2, C_1 & C_2	I	S_3^*	S_4^*	BP or OVR	–	Fig. 4.15(a)
			II	S_4^*	S_3^*	(S_3, S_4)		Fig. 4.15(b)
DC bus to battery	$P_{DC} = P_B$	S_3, S_4, L_2, C_1 & C_2	I	S_3^*	S_4^*	BP	–	Fig. 4.16(a)
			II	S_4^*	S_3^*	(S_3, S_4)		Fig. 4.16(b)

* Switch operates in PWM $^\circ$ Switch is fully ON

4.2.4 Inductors and Capacitors Design

Choosing the magnetic core material is mainly dependent on the application. Iron powdered core is hard to saturate because it has an inherent distributed air gap and has a low μ so it is suitable for chokes and inductors but not for transformers. However, it produces a high core losses and high flux density. In contrast, ferrite core is suitable for frequency (1khz- few hundred khz) as it has lower flux density and core losses. A comparison between it as in Table 4.4. To be able to calculate number of turns A_L inductor factor should be taken from T80-26 datasheet which

Table 4.4: Comparison between different types of inductors materials

Inductor material	**Saturation**	**Core losses**	μ	**Flux density**
Iron powdered	Hard	High	Low	High
Ferrite core	Easy	Low	High	Low

is 46 nH/t^2. Then the following equation can be used:

$$N = \sqrt{\frac{L}{A_L}} \tag{4.20}$$

To calculate the core losses flux density should be calculated first as follow:

$$\delta B = \frac{vD}{fNA_c} \tag{4.21}$$

The core loss of T80-26 material by the formula provided in the datasheet is:

$$Coreloss(mW/cm^3) = \frac{f}{\frac{a}{B^3} + \frac{b}{B^{2.3}} + \frac{c}{B^{1.65}}} + df^2B^2 \tag{4.22}$$

The skin depth of the inductor is given by:

$$\delta = \frac{7.5}{\sqrt{f}} = 0.335mm \tag{4.23}$$

As the converter is designed to work in continuous conduction mode the minimum inductor and capacitor equations are given below:

$$L_1 = \frac{(V_{PV} - V_{DC})}{\Delta i_{L_1} f} d_1 \tag{4.24}$$

$$C_1 = \frac{(1 - d_1)V_{DC}}{8L_1 f^2 \Delta V_{DC}} \tag{4.25}$$

$$L_2 = \frac{(V_{PV} - V_B)}{\Delta i_{L_2} f} d_3 \tag{4.26}$$

$$C_2 = \frac{(1 - d_3)V_B}{8L_2 f^2 \Delta V_B} \tag{4.27}$$

where $V_{PV}, V_{DC}, V_B, d_1, d_2, d_3, \Delta i_{L_1}, \Delta i_{L_2}$, and f are the PV source voltage, the DC bus voltage, battery voltage, duty cycle of S_1, duty cycle of S_2, duty cycle of S_2, first inductor ripple current, second inductor ripple current, and switching frequency. The worst case, which is DISO in Mode 5, is used to calculate the capacitor C_3,

$$C_3 = \frac{[i_{L_1}(t_d) - i_{L_1(max)}]t_d + [(1-d_3)T - t_d]I_{PV}}{\Delta V_{PV}} \tag{4.28}$$

where C_3 is the input capacitor connecting the PV to battery converter and t_d is the delay between the switch S_1 PWM and S_3 PWM signals.

4.3 Control Structure and Mode Selection

The TPC topology consists of two pairs of switches where in each pair the switches are working complementary during different modes. Both switches of these complementary pairs will turn on/off according to the requirements of the modes. The control arrangement loops, namely MPPT, battery protection (BP) and output voltage regulation. MPPT is achieved through the first pair S_1 & S_2, while S_3 & S_4 are responsible for both output voltage regulation (PI controller) and battery protection. Texas Instrument DSP controller (TMS320F28379D) is used to control the converter. The TPC is constructed based on basic buck and boost converters. The transfer functions of buck and boost converters are given in many literatures as in [89]. To make the buck converter model more precise, many parameters have been added to the basic transfer function as in [90]. After substituting all components values in the transfer function as in (4.29) & (4.30), Matlab is used to find the Z-transform of the transfer function using zero-order hold (ZOH) model as in (4.31). Then, the margin stability bode plot and root locus tools are used to find the controller transfer function as in (4.32) and the step response of the closed-loop system where K_a=k_p andK_b=k_iT_s-k_p as shown in Fig. 4.17. For the buck converter, K_a = 0.2 and K_b= -0.19 which used in DSP to control the converter.

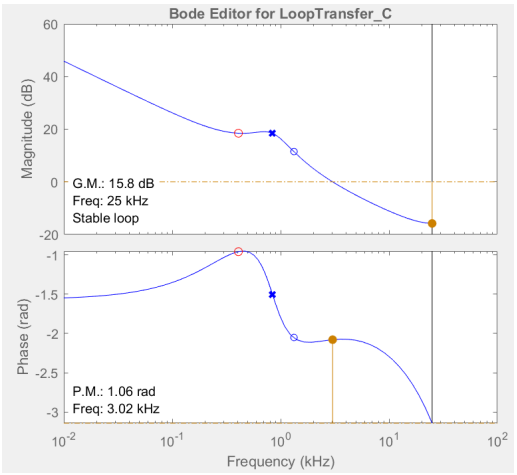

(a) Margin stability bode plot

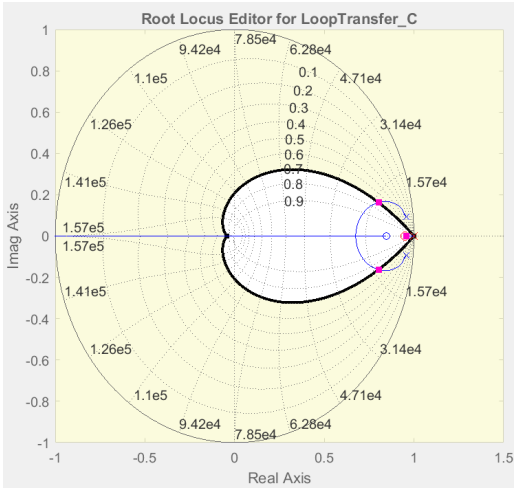

(b) Root locus of the closed loop transfer function

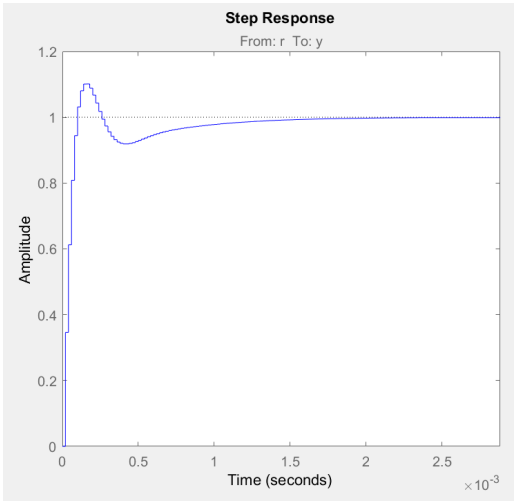

(c) Step response

Fig 4.17: Bode plot, Root locus of the closed-loop transfer function and the step response of the buck converter.

$$G_{vd}(s) = \frac{\frac{RV_i}{LC(R+r_c)}(r_cCs+1)}{s^2 + (\frac{1}{L}(r_L+r_c) + \frac{1}{C(R+r_c)})s + \frac{r_L+R}{LC(R+r_c)}} \tag{4.29}$$

$$G_{vd}(s) = \frac{0.04446s + 370.5}{5.346e^{-7}s^2 + 0.002146s + 15.01} \tag{4.30}$$

$$G_{vd}(z) = \frac{1.73z - 1.464}{z^2 - 1.912z + 0.9228} \tag{4.31}$$

$$G_c(z) = \frac{0.2z - 0.19}{z - 1} \tag{4.32}$$

Similarly, the transfer function of boost converter is obtained as in (4.33) and the

controller function in (4.34). The step response of the closed-loop system of boost converter is presented in Fig. 4.18 and the parameters are $K_a = 0.0004$ and K_b= -0.00032.

$$G_{vd}(z) = \frac{-3.36z^2 + 6.794z - 3.176}{z^2 - 1.975z + 0.9802} \tag{4.33}$$

$$G_c(z) = \frac{0.0004z - 0.00032}{z - 1} \tag{4.34}$$

The working of the two pairs of complementary switches can be conveniently explained with the help of Table 4.2 and Table 4.3. There are four SISO modes (1, 2, 6 & 7) in which only one pair of switches is receiving PWM signals. However, it is worth mentioning that in Modes 6 & 7, S_1 is always on while S_2 is always off to achieve single-stage power conversion. In the remaining modes, all switches receive PWM signals. Based on the available power and load power demand, the mode is selected automatically. It is evident that there are 7 different modes toggling from one mode to another according to the conditions.

The aforementioned switching requirements in different modes present a challenge in designing a proper switching strategy that optimizes the conversion efficiency, manages system delays and fulfills the control objectives. To show the merits and feasibility of the proposed method, different scenarios are considered for comparison with conventional practice:

Case 1: The "no PV power" scenario is activated when the PV power is set to 0 W. In practice, the PV power is larger than 0 W during daylight even in cloudy or stormy weather condition and thus the power threshold should be defined. Conventionally, the converter turns OFF to avoid losses. However, if the generated power from the PV source is higher than the losses, it is worth keeping the converter ON, as in the proposed method and using this power instead of losing it all. This will also simplify the control patterns, making the one pattern control possible. For example, 1% of 30 W power is 0.3 W and the condition is to turn the converter ON if the PV power is higher than 0.3 W, even when the loss in the converter is 0.1 W.

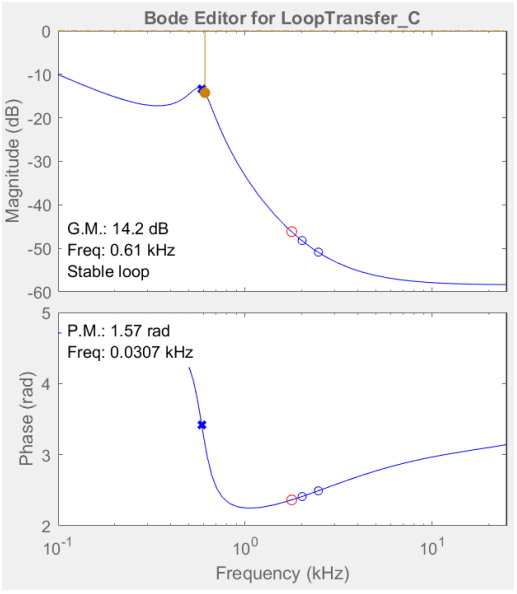

(a) Margin stability bode plot

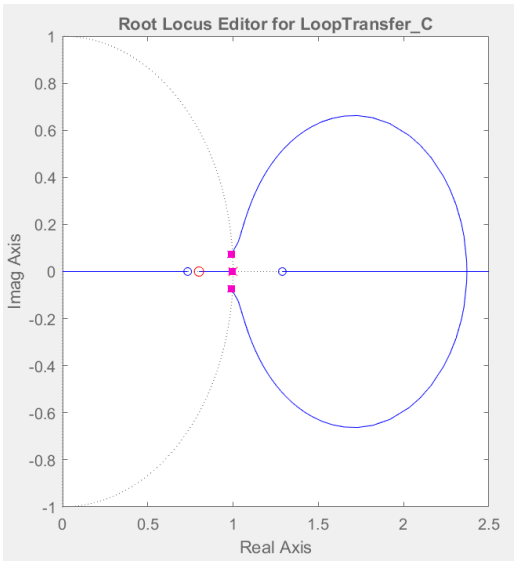

(b) Root locus of the closed loop transfer function

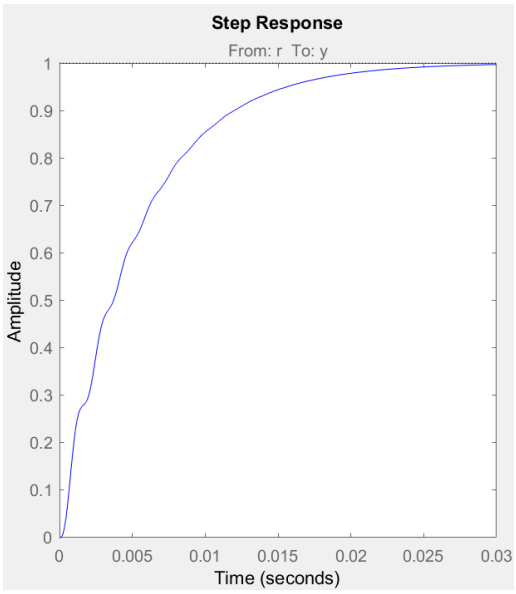

(c) Step response

Fig 4.18: Bode plot, Root locus of the closed-loop transfer function and the step response of the boost converter.

Case 2: If the converter that is connected to the PV source is turned OFF, the PV power may not be able to measure unless additional light sensor is used which increase the cost and the complexity. Another way is to deliberately turn ON the converter periodically (such as in every 2 s) to check the PV power availability. In the proposed method, the converter is always ON and it would not run into this situation except when the PV power is close to 0 W for a long time such as during

night time. Once the converter becomes OFF the V_{OC} is used as an indicator to turn ON the converter and measure the power if it is more than the threshold, as shown in the left side of Fig. 4.22.

Case 3: Conventionally in PV to DC bus mode, the converter that is connected to the battery is turned OFF, and in this case there is no output voltage regulation, where one control objective will be sacrificed. In addition, it is rarely to have PV power exactly equal output power but a constant variation above or below the output load power. In the proposed method, when PV power is close to the power of DC bus there is no need to check $P_{PV} = P_{DC}$ condition and turns the converter OFF as in the conventional method because there is no power injecting from the battery.

Case 4: Every mode transition takes 2 s to be active. The reason is to ensure steady measurements. For example, if the battery voltage exceeds the maximum voltage, the second pair (S_3 & S_4) turns OFF to protect the battery. As a result after short period of time the battery voltage reaches slightly lower than the maximum voltage and turns ON. If the update is very fast, the system turns the converter ON and OFF at similar speed. As a result the switching losses would increase in proportion to the frequency at which it switches. In Fig. 4.22(b), the minimum response time of the commercial PV emulator used in this experiment is 1 s. Therefore, minimum 2 s update is needed to to ensure steady measurements. However, the proposed method reduces the selection conditions and simplifies the decision making process with less frequent updates.

4.3.1 The Proposed Method

In order to get rid of the complex switching patterns and the associated control design, a new criterion for mode selection has been proposed where both pairs of the switches are receiving PWM signals all the time. The power loss when there is

no input power is found by LTspice© to be around 0.1 W for the proposed method which means less than 1% degradation of the efficiency.

In Type II-IIA circuit, the first pair (S_1 & S_2) will be responsible for regulating the output voltage while the second pair (S_3 & S_4) is achieving MPPT. In PV to battery mode, no power is being transfered by S_1 & S_2 as there is no load. On the other hand, S_3 & S_4 are transferring power from the PV source to the battery. Furthermore, the PV to DC bus mode can be achieved when the PV power is equal to the power of DC bus. This power will not be coming from the battery even it is connected. In battery to DC bus mode, the power will be transferred from the battery to the DC bus under no-PV power condition. In this way, the converter is moving from one mode to another irrespective of any conditions. This makes a single pattern control for all the three ports of the converter possible. In the conventional way, 3 current sensors, 3 voltage sensors and 1 irradiation sensor are needed for the proposed method. However, only 1 current sensor and 3 voltage sensors are used. In this method there are only two conditions namely, the battery being over-charged (V_{Bmax}) or discharged (V_{Bmin}) and the PV power being under the threshold (P_{Th}) for a long time (t_{Th}) such as during night time, as shown in Fig. 4.19(a).

Similarly, in Type II-IIB circuit, the first pair (S_1 & S_2) will be responsible for MPPT while the second pair (S_3 & S_4) is regulating the output voltage. In battery to DC bus mode, no power is being transfered by S_1 & S_2 as there is no PV power. On the other hand, S_3 & S_4 are transferring power from battery to DC bus. Furthermore, the PV to DC bus mode can be achieved when the PV power is equal to the power of DC bus. This power will not be coming from the battery even it is connected. In PV to battery mode, the power will be transferred from PV to battery under no-load condition. In this way, the converter is moving from one mode to another irrespective of any conditions. In this method there are only two conditions namely, the battery being over-charged or discharged and the PV power being under the threshold for a long time such as during night time, as shown in Fig. 4.19(b).

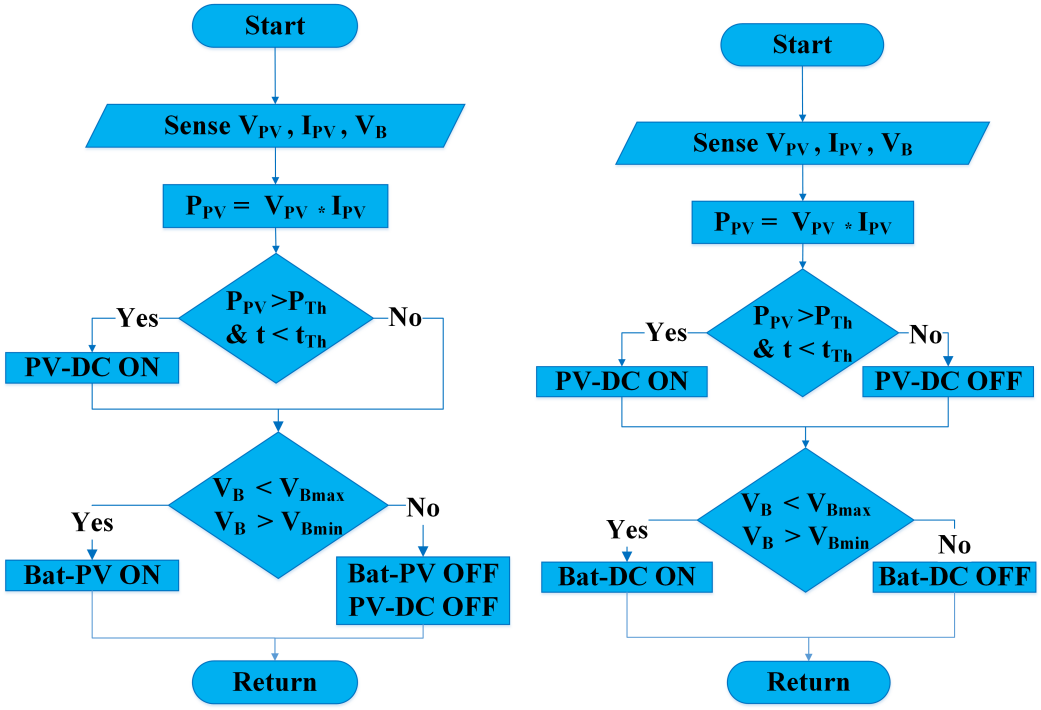

(a) Type II-IIA (b) Type II-IIB

Fig 4.19: Flowchart of the proposed method with only 2 conditions to implement all 7 modes of operation for both converter.

In this work, the output is a resistive load where a linear controller can satisfy the stability of the system. However, if the output is a constant power load (CPL) there is no guarantee that the control performance will be satisfactory for all operating range. However, this problem has been well rehearsed in literature [91], where an observer-based dc voltage droop and current feed-forward control is presented. In addition, authors in [92] proposed a novel composite nonlinear controller for stabilization of constant power load. Furthermore, feedforward terms are added to V-I droop-based dual-loop controller to ensure the exponential stability in the whole operating range [93]. These methods are applicable to TPCs which will be our future work as it requires extensive analysis and it is not the scope of this research. Nevertheless, the main contribution is designing TPCs with smooth transitions for 7 distinctive operating modes.

4.4 Experimental Results

The experimental setup of Type II-IIA and Type II-IIB circuits is shown in Fig. 4.20(a). A hardware prototype is built as in Fig. 4.20(b) and tested based on Fig. 4.1(a), and then modified based on Fig. 4.1(b). The components used in the circuit are listed in Table 4.5 and shown in Fig. 4.21. Simple voltage divider is used to sense the voltage of each port as shown in Fig. 4.20(b). In addition, ACS712 current sensor is connected to the PV port. The experimental waveforms and transient responses of changing from one mode to another for Type II-IIA and Type II-IIB converters are shown in Figs. 4.23 and 4.24, respectively.

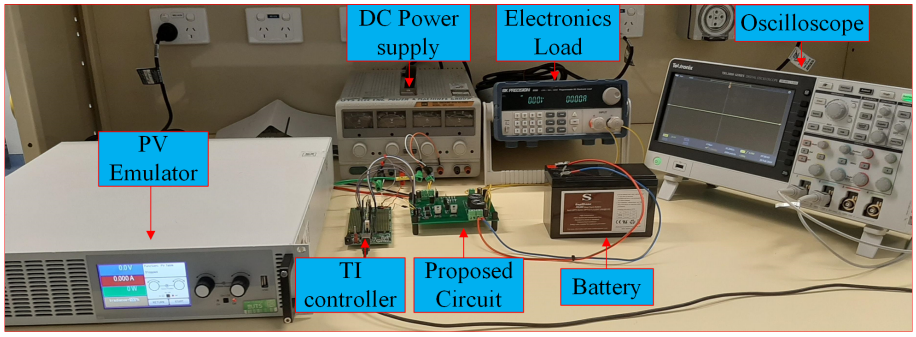

(a) Experimental setup of the proposed circuit

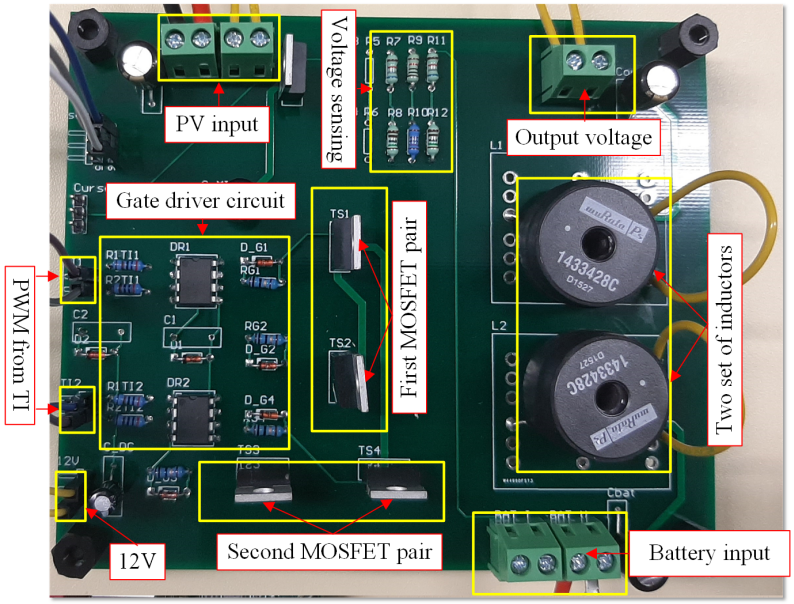

(b) Hardware prototype of Type II-IIA circuit

Fig 4.20: Experimental setup and the prototype of the circuit.

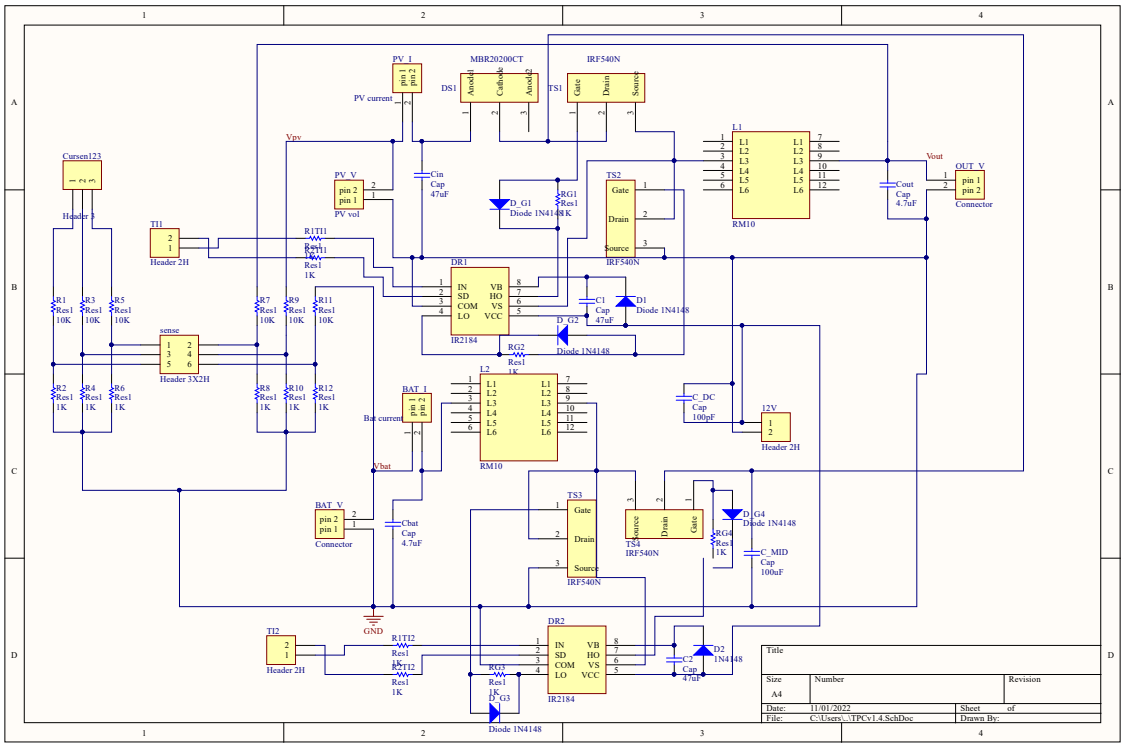

Fig 4.21: The schematic diagram of the presented circuit.

In Fig. 4.23, the order of these four traces from top view to bottom view are PV voltage, output voltage, first inductor current and battery current respectively. A PV emulator is used and a simple Perturb and Observe (P&O) is used to achieve MPPT where $V_{MPP} = 23$ V. The output port is connected to an electronic load which is programmed as Constant Voltage (CV) at 15 V. In Fig. 4.23(a), battery current is zero as the PV source supplies power to the DC bus only and the inductor

Table 4.5: Component specification

Parameter	Value
Controller	TMS320f28379D
Battery	12 V, 7.2 A
PV emulator	ELEKTRO-AUTOMATIK EA-PSI 9360-15 (30 W)
Output	ELEKTRO-AUTOMATIK EA-EL 9750-25
MOSFETs	IRF540Z
D_1	STPS10L25D
L_1 and L_2	330 uH
C_1 and C_2	100 uF
f_s	50 KHz
C_3	120 uF

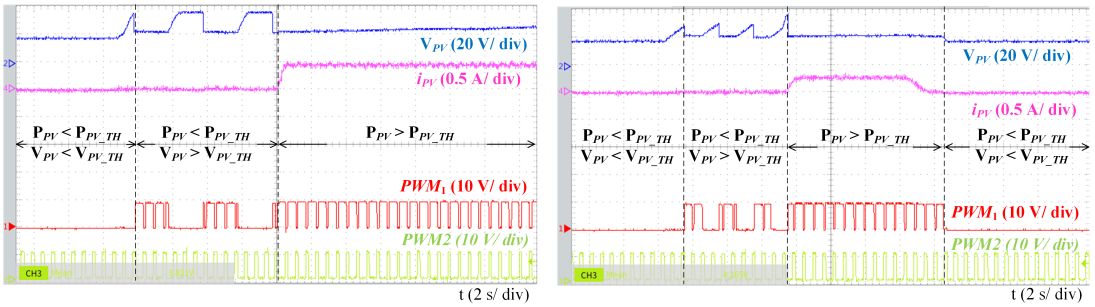

(a) Buck converter operates with the PV power and V_{OC} as indicators with 2 s update.

(b) Buck converter operates with the PV power and V_{OC} as indicators with 1 s update.

Fig 4.22: The power conditions of the upper converter (buck) of Type II-IIB.

current is approximately 2 A. Then, in Fig. 4.23(b), DC bus is not connected (i.e., $V_{DC} = 0$). The current from the battery is negative to indicate that the battery is charging. Fig. 4.23(c) shows the transient response of transition from Mode 4 (where PV and battery are supplying power to the DC bus and when PV is able to supply both DC bus and battery) switched to Mode 3 (where the battery current changed the direction to charging). Fig. 4.23(d) shows the transient response of transition from Mode 4 to Mode 6 or vice-versa, the PV source and battery are supplying power to the DC bus and when PV does not have enough power, the battery can power the DC bus and increase the battery's current to cover absence of the PV source. Fig. 4.23(e) shows the transient response of transition from Mode 6 to Mode 3, the battery is discharging to the DC bus. When PV has power to supply the battery and DC bus at the same time, the system will pass through Mode 4 for a small period of time, typically less than half a second, and then will reach Mode 6 in the steady state. Fig. 4.23(f) shows the transient response from Mode 5 to Mode 7. The DC bus is supplying the battery then PV has some power with DC bus to supply the battery. Therefore, the battery's current continues to charge but at a higher level when the PV source has excess power.

The transition response of Type II-IIB converter is shown in Fig. 4.24. Fig. 4.24(a) shows a step response from PV emulator with no load. Fig. 4.24(b) shows a step response in the load at no PV power. Fig. 4.24(c) shows a step change in PV power to 0 and battery supplies the load. Fig. 4.24(d) shows PV power

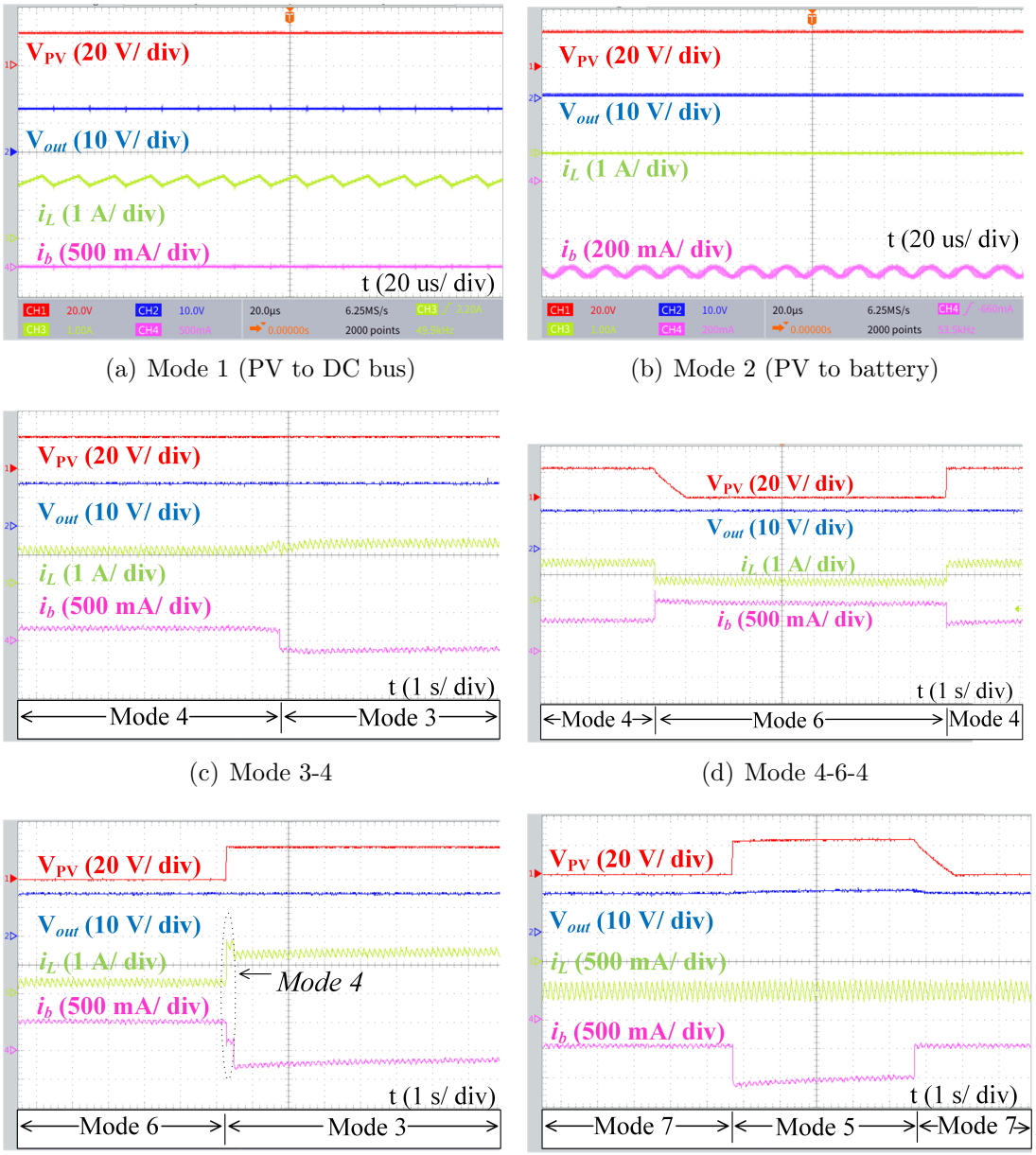

(a) Mode 1 (PV to DC bus)

(b) Mode 2 (PV to battery)

(c) Mode 3-4

(d) Mode 4-6-4

(e) Mode 6-4-3

(f) Mode 7-5-7

Fig 4.23: Waveforms of Type II-IIA converter.

only supplies load and then battery supplies the load. Finally, Fig. 4.24(e) shows continuous change in PV power to show the controllability of the converters in different modes.

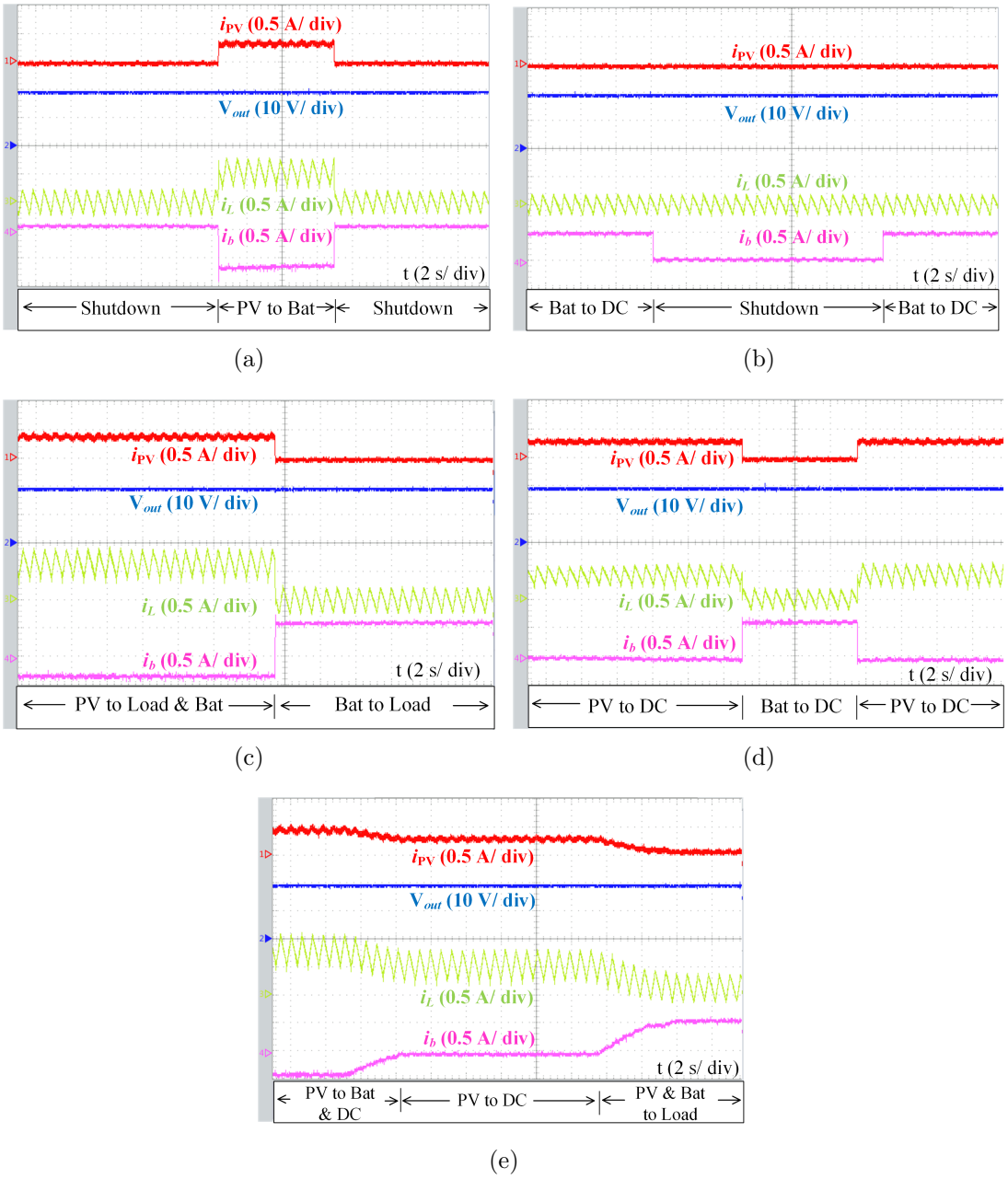

Fig 4.24: Waveforms of Type II-IIB converter.

4.5 Summary

Conventionally, mode transition is achieved by assigning specific switching patterns through feedback signals and control algorithms. Defining a power threshold, ensuring smooth transition, achieving fast response, minimizing sensor error and time to update are issues in the conventional mode selection. A mechanism for ensuring fast and smooth transitions of operating modes for TPCs is presented in this

chapter. In addition, this work considers two bidirectional ports as compared to only one bidirectional port in most reported topologies. This configuration enables both standalone and grid-connected applications. MPPT, battery protection and output voltage regulation are achieved. In the proposed method, the number of switching patterns is significantly reduced and decisions are simplified for all modes. The transitions between modes are achieved with fast settling time and no obvious overshoot and undershoot. Based on the power availability and load demand, the mode is activated automatically. The proposed control strategy and mechanism for TPC have potential applications in the DC microgrid.

Chapter 5

Topological Derivations and Study of Type I-III-I & Type I-II-I Configurations

5.1 Overview

Based on the research conducted in Chapter 3, it is evident that TPCs consisting of two power flow paths will always give the best required results. However, taking three power flow graphs will give some useful configurations, such as single power conversion. This chapter studies all possible power flow graphs, with a particular focus on those converters with three power flow subgraphs. Each of these configurations has been studied, and circuit realisation has been done. Additionally, a comparison has been carried out for all useful configurations.

5.2 A Review of Three-Port Configurations

There are many ways of deriving the TPCs configuration, as explained previously in [32,62,67,94]. In [62], a systematic analytical technique for different configurations is constructed based on the power flow graph tool. The extension of this work with different buck, boost and buck-boost converters is presented in [67]. This work was specifically designed for some specific configurations. Similarly, power flow graphs have been used to construct different configurations for IoT applications, as in [94]. A computer program was used to drive different topologies of three-port converters [95]. As compared to the manual derivation method, this programmable method is faster and covers more viable topologies. However, the main structure is limited to one inductor and three switches. Therefore, any changes in the TPCs, such as the bidirectional port, leads to a repeat of the whole derivation process. In [32], five TPC structures were constructed limited to a single bidirectional port. Therefore, this chapter focuses on analysing two bidirectional ports where all these structures are modified, as shown in Fig. 5.1. These structures are evaluated comprehensively based on three dimensions: efficiency, the complexity of the topology, and control simplicity. A comparison of these five structures is outlined in Table 5.1.

Many factors can affect the efficiency of a TPC. One factor is the number of power processing stages between any two ports. The TPC structure in Fig. 5.1(a) is the best in terms of efficiency as a single power processing between any two ports. The TPC structures in Fig. 5.1(c) and Fig. 5.1(d) comes after the TPC structure in Fig. 5.1(a) as two paths have single power processing. After that, the TPC structure in Fig. 5.1(b) has two paths of single power processing. However, it has two power processing in the primary path (PV source to DC bus). Finally, the TPC structure in Fig. 5.1(e) has two power processing between any two ports. Based on the topology complexity, the TPC structures in Fig. 5.1(b) and Fig. 5.1(c) are the best, as only two converters are needed. The next best is the TPC structure in Fig. 5.1(d), where two converters are bidirectional, then the TPC structure in Fig. 5.1(a),

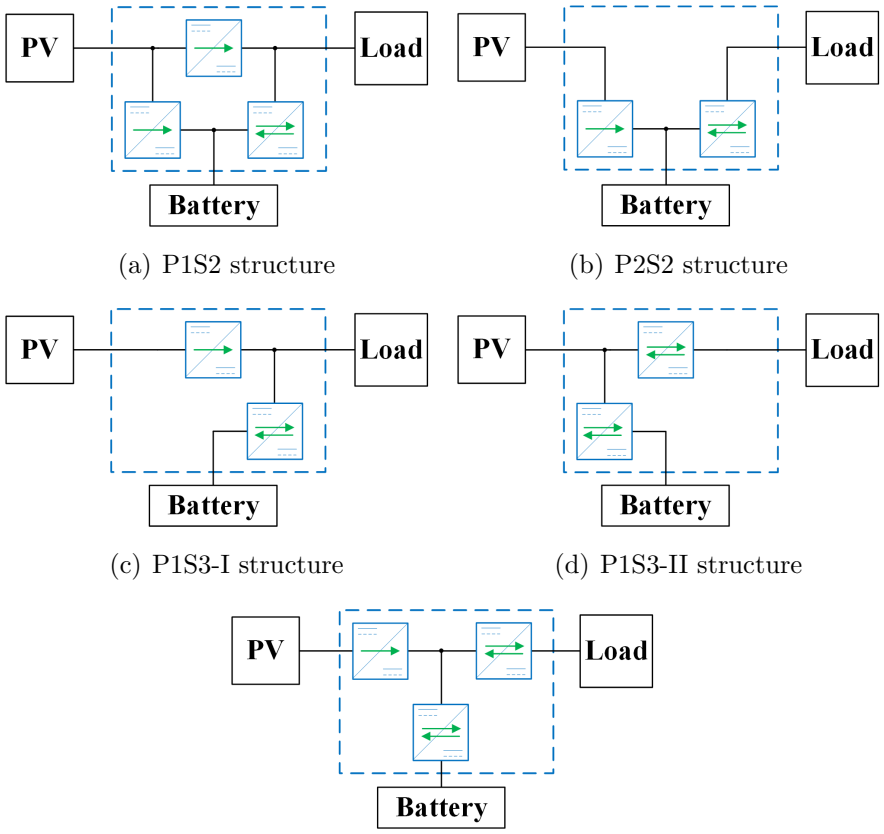

(a) P1S2 structure (b) P2S2 structure

(c) P1S3-I structure (d) P1S3-II structure

(e) P2S4 structure

Fig 5.1: A modified TPC structures with two bidirectional ports based on [32].

which has two unidirectional converters and one bidirectional converter. Finally, the TPC structure in Fig. 5.1(e) has two bidirectional converters and one unidirectional converter. This feature could be advantageous based on the control simplicity as fewer control parameters (controller) are used. However, the system will have less control objective as well [96]. Therefore, the TPC structures in Fig. 5.1(b) and Fig. 5.1(d) are the simplest as every converter achieves one control objective for all different modes of operation. The TPC structure in Fig. 5.1(c) has two control objectives. However, these objectives will change in different modes, which increase the complexity of this structure. Finally, the TPC structures in Fig. 5.1(a) and Fig. 5.1(e) have three control objectives which are the most complex to control.

Table 5.1: A comparison between different TPC structures [32].

	Efficiency	**The complexity of the topology**	**Control simplicity**
P1S2 structure	Highest	High	Lowest
P2S2 structure	Low	Lowest	Highest
P1S3-I structure	High	Lowest	High
P1S3-II structure	High	Low	Highest
P2S4 structure	Lowest	Highest	Lowest

5.3 Circuit Realisation Based on Proposed Power Flow Graphs

This section includes the circuit realisation based on proposed the power flow graphs, which was initially proposed in Chapter 3. A Type I-II-IA is based on the power flow graph shown in Fig 5.2. This structure has a central converter and a unidirectional converter between the PV source to the battery. The central converter can achieve the PV source to the battery and the DC bus through a single inductor by using two paths. These two sources have the time-sharing between them to ensure the switches are working in an alternate pattern [97,98]. In addition, a bidirectional path can be constructed between the DC bus and the battery using the same central converter. Finally, a separate converter is used to connect the PV source to the battery. Compared with other topologies, this topology can achieve single power processing for all seven modes at the cost of adding only one additional switch.

The first circuit of Type I-III-IA, in Fig. 5.3(b) is based on the proposed power flow graph as depicted in Fig 5.3(a). In PV to DC bus and battery mode, the power will be processed from the PV source to the battery by the buck converter and DC bus has a connection to the PV source via C_1. The first converter is connected between the PV source and the battery. The second converter is a bidirectional converter between the battery and the DC bus. This converter will have high efficiency in the PV source to the battery and the DC bus mode as it involves single power processing among the ports. Similarly, the battery to the DC bus and the DC bus to the battery mode also involves single power processing. On the other hand, to

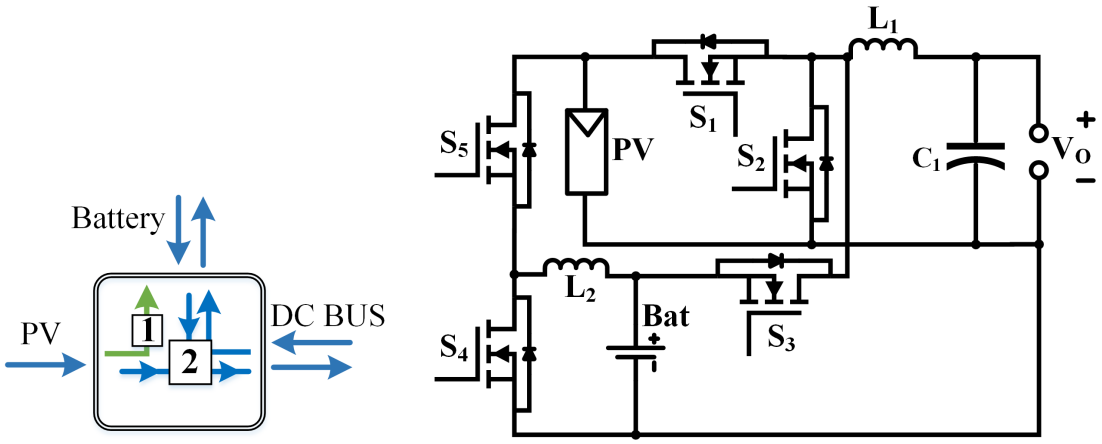

(a) Type I-II-IA (b) Circuit

Fig 5.2: Type I-II-IA realisation.

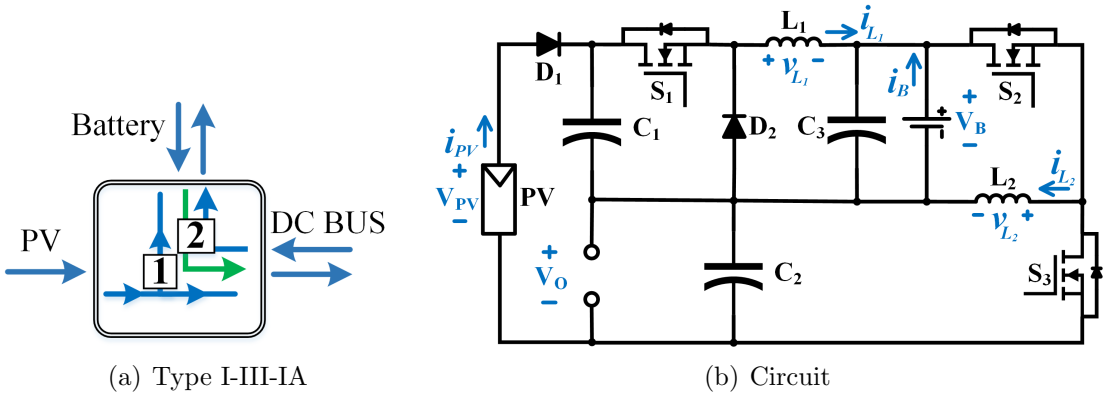

(a) Type I-III-IA (b) Circuit

Fig 5.3: Type I-III-IA realisation.

achieve the PV source to the DC bus and the PV source to the battery modes, all switches are required to complete the path and achieve these modes. This results in double power processing, which will degrade the efficiency but ensure that the system will work even if the battery or the DC bus are disconnected.

The second circuit of Type I-III-IB, in Fig. 5.4(b) is based on proposed the power flow graph as depicted in Fig 5.4(a). In PV to DC bus and battery mode, the power will be processed from the PV source to the DC bus by the buck converter and the battery has a connection to the PV source via C_1. The first converter is connected between the PV source and the DC bus. The second converter is a bidirectional converter between the battery and the DC bus. This converter will have high efficiency in the PV source to the battery and the DC bus mode as it

involves single power processing among the ports. Similarly, the battery to the DC bus and the DC bus to the battery mode involves single power processing. On the other hand, in order to achieve the PV source to the DC bus and the PV source to the battery modes, all switches are required to complete the path and achieve these modes. As above, this results in double power processing, which will degrade the efficiency but will ensure that the system will work even if the battery or the DC bus are disconnected.

The third circuit of Type I-III-I-C configuration is realised based on the proposed power flow graph in Fig 5.5. This configuration has a direct connection between the battery and the DC bus. The first converter is connected between the PV source to the battery and the DC bus. The second converter is a bidirectional converter between the battery and the DC bus. This converter can have high efficiency in the PV source to the battery and the DC bus mode as it involves single power processing among the ports. Similarly, the battery to the DC bus and the DC bus to the battery mode also involves single power processing. This converter works similar to the converter mentioned above in the PV source to the DC bus and the PV source to the battery modes.

The fourth circuit of Type I-III-I-D is based on the power flow graph shown in Fig 5.6. This structure has a central converter and a bidirectional converter between the battery and the DC bus. The central converter can couple the PV source to the battery and the DC bus through a single inductor using a different path but increases the number of switches. However, the PV source to the DC bus and the PV source to the battery mode is achievable through single power processing without using all the switches to complete the path.

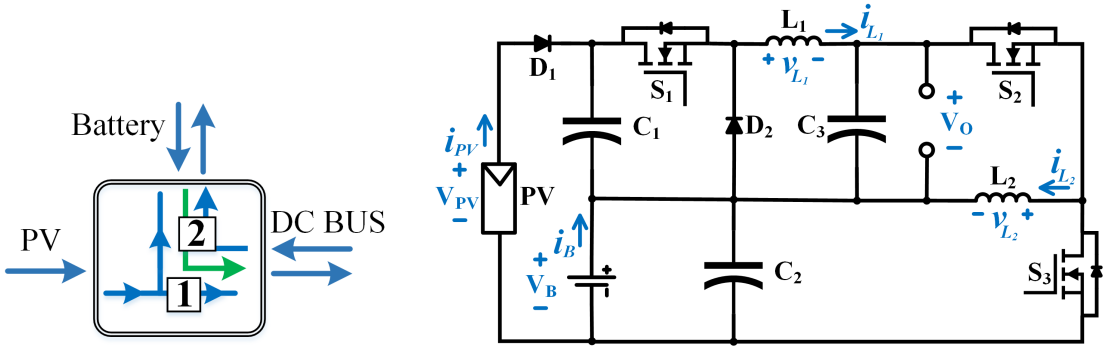

(a) Type I-III-IB (b) Circuit

Fig 5.4: Type I-III-IB realisation.

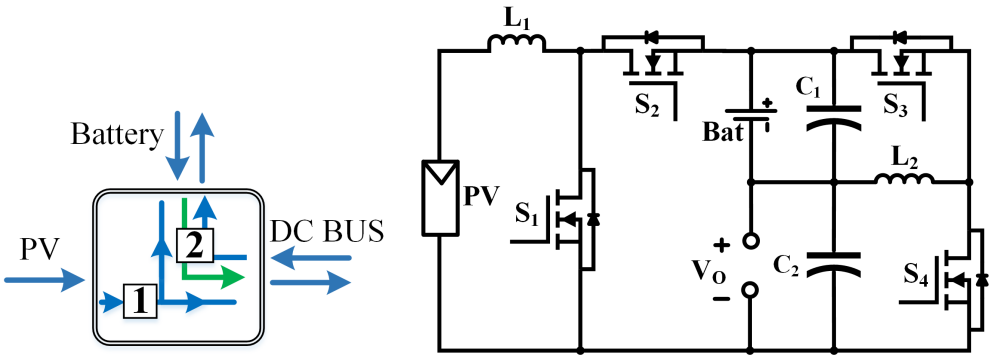

(a) Type I-III-IC (b) Circuit

Fig 5.5: Type I-III-IC realisation.

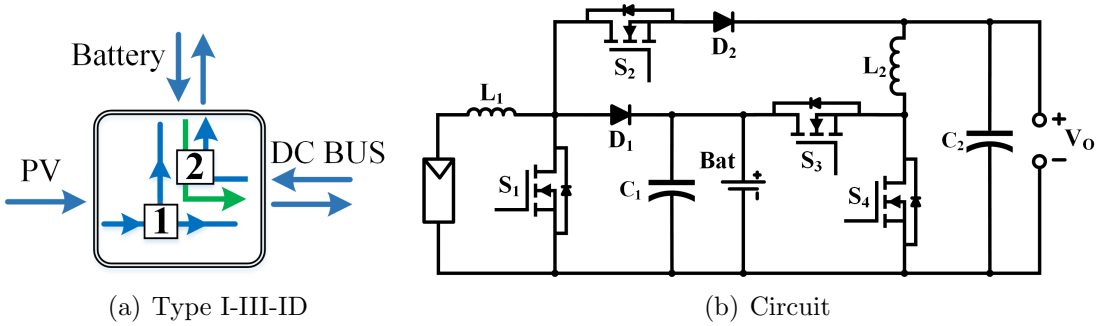

(a) Type I-III-ID (b) Circuit

Fig 5.6: Type I-III-ID realisation [56].

5.4 Principles of Type I-III-IC Operation

This section discusses principles of operations and simulation results of Type I-III-IC, which has been chosen for the purpose of illustration. The converter connected with the PV source to the battery and the DC bus is a boost converter. The battery is connected to the DC bus using a bidirectional buck-boost converter. The circuit

realisation is shown in Fig. 5.5. These simulations results include Mode 5, 6, and 7, as the first four modes are SISO which are easy to implement. According to design requirement, the converter operates in continuous conduction mode (CCM). The circuit has seven modes of operation. These modes are discussed as below:

1. **PV to DC bus:** In this mode, the PV source supplies the power only to the DC bus as the battery is at maximum SoC.

2. **PV to battery:** In this mode, the PV source supplies the power to the battery at no load condition.

3. **Battery to DC bus:** In this mode, the battery supplies the power to the DC bus as the PV source cannot supply power during nighttime.

4. **DC bus to Battery:** In this mode, the DC bus supplies the power to the battery as the PV source cannot supply power during nighttime.

5. **PV to battery and DC bus:** In this mode, the PV source has sufficient power to supply the battery and the DC bus. Fig. 5.7 shows two switching states and explained as follows:

   State I $[t_0 < t < t_1]$: S_1 is turned ON. The PV source starts to charge L_1 where $I_{L_1} = I_{PV}$ as shown in Fig. 5.7(a). When S_1 turns OFF at $t = t_1$, this state ends.

   State II $[t_1 < t < t_2]$: S_1 is turned OFF. L_1 starts to discharge to the battery and the DC bus, as shown in Fig. 5.7(b). When S_1 turns ON at $t = t_2$, this state ends. The simulation waveforms are shown in Fig. 5.7(c).

6. **PV and battery to DC bus:** In this mode, the battery and the PV source provide the power to the DC bus. The system now operates as a DISO converter. Fig. 5.8 shows four switching states and explained as follows:

   State I $[t_0 < t < t_1]$: S_1 and S_3 are turned ON while S_2, S_4 are OFF. PV starts to charge L_1. In addition, L_2 starts to charge from the battery via S_3, as shown in Fig. 5.8(a). The voltage across L_1 is given by $v_{L_1} = V_{PV}$ and that

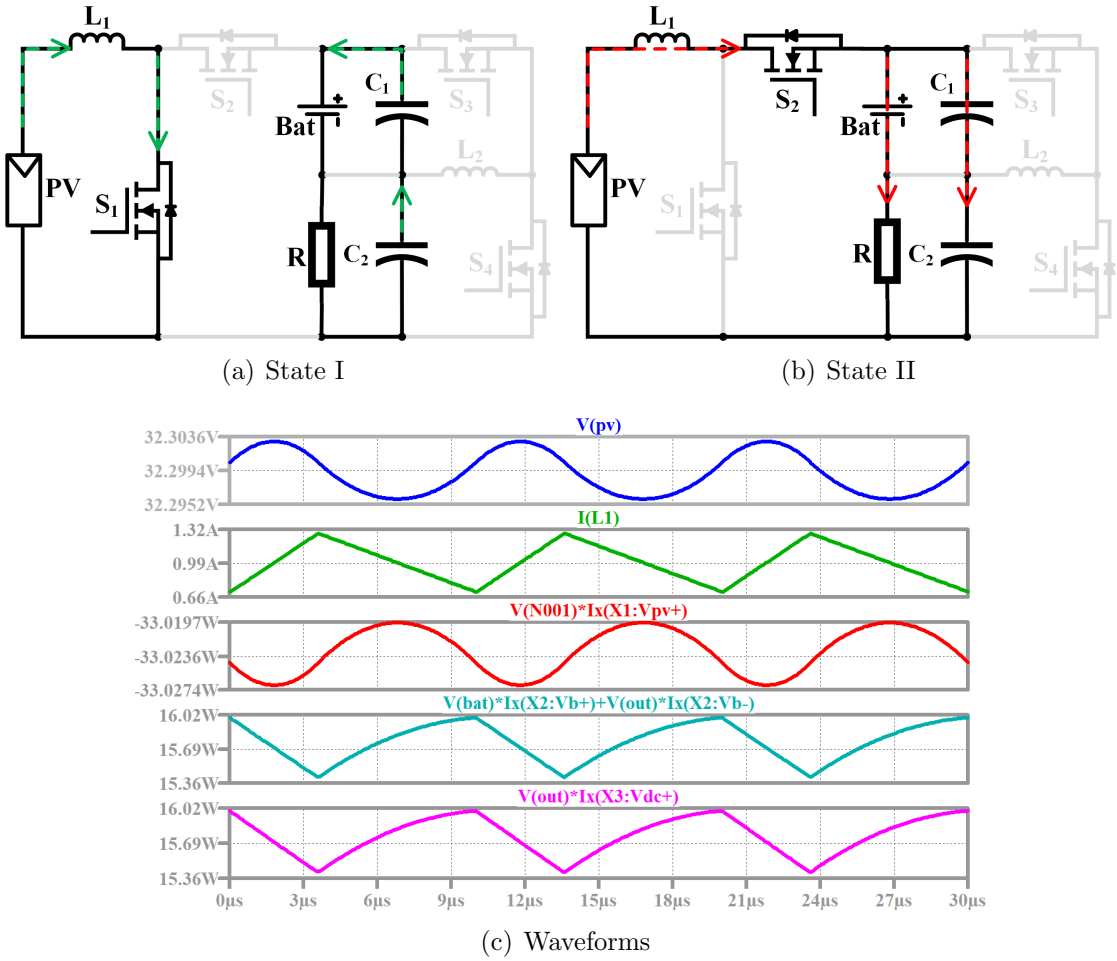

(a) State I (b) State II

(c) Waveforms

Fig 5.7: Type I-III-IC circuit Mode 5 SIDO.

across L_2 is given by $v_{L_2} = V_B$. This mode ends when S_3 turns OFF at $t = t_1$.

State II $[t_1 < t < t_2]$: S_1 and S_4 are turned ON while S_2, S_3 are OFF, PV source continues to charge L_1. In addition, L_2 starts to discharge into the DC bus and C_2, as shown in Fig. 5.8(b). The voltage across L_1 is given by $v_{L_1} = V_{PV}$ and across L_2 is given by $v_{L_2} = -V_{DC}$. This mode ends when S_1 turns OFF at $t = t_2$.

State III $[t_2 < t < t_3]$: S_2 and S_4 are turned ON while S_1, S_3 are OFF, L_1 starts to discharge to the battery via S_2. In addition, L_2 continues to discharge into the DC bus and C_2, as shown in Fig. 5.8(c). The voltage across L_1 is given by $v_{L_1} = V_{PV} - V_{DC} - V_B$ and across L_2 is given by $v_{L_2} = -V_{DC}$. This mode ends when S_3 turns ON at $t = t_3$.

State IV $[t_3 < t < t_4]$: S_2 and S_3 are turned ON while S_1, S_4 are OFF. L_1

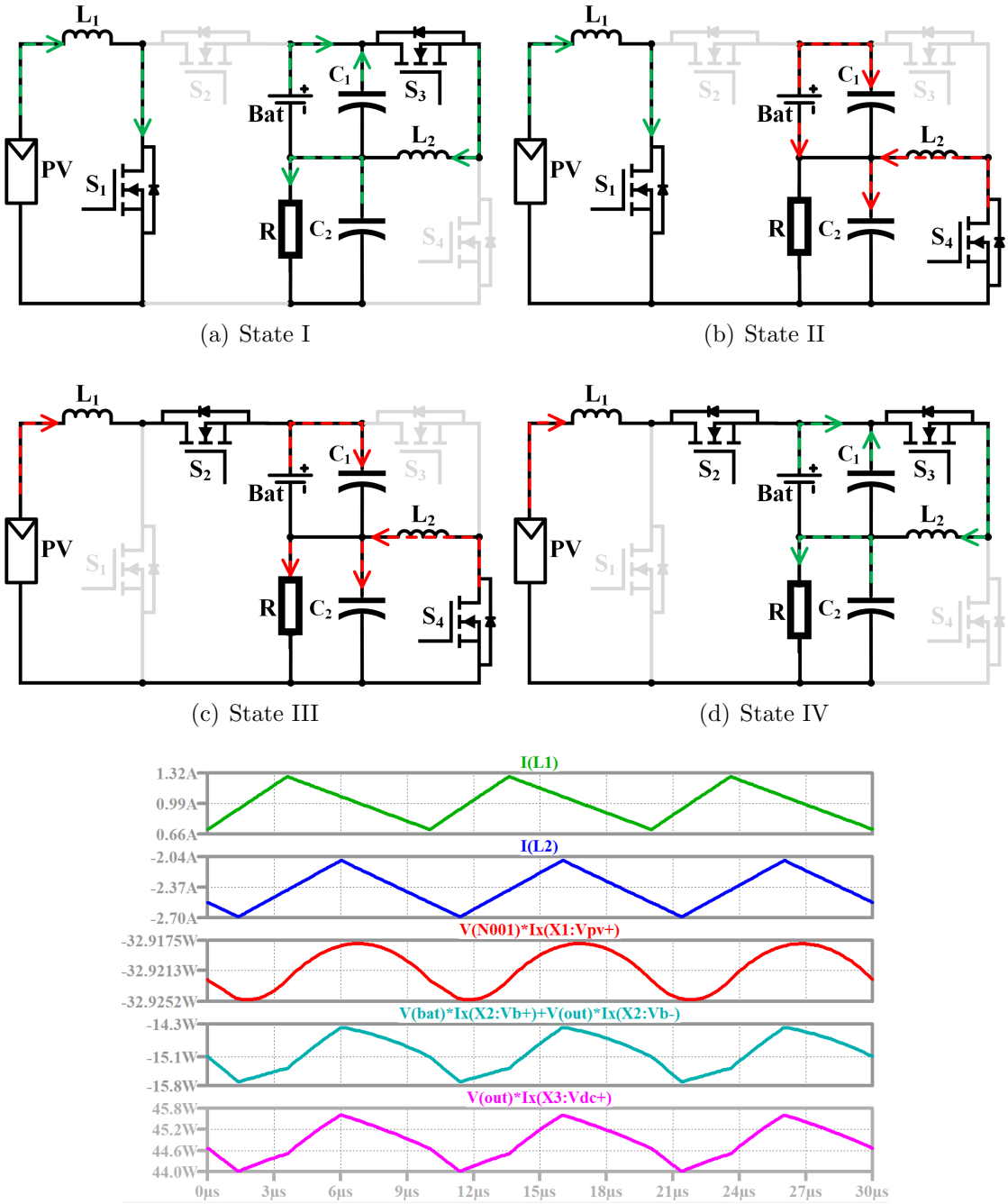

Fig 5.8: Type I-III-IC circuit Mode 6 DISO.

continues to discharge into the battery. In addition, L_2 start to charge from the battery and C_1, as shown in Fig. 5.8(d). The voltage across L_1 is given by $v_{L_1} = V_{PV} - V_{DC} - V_B$ and across L_2 is given by $v_{L_2} = V_B$. This mode ends when S_1 turns ON at $t = t_4$. The simulation waveforms are shown in Fig. 5.8(e).

7. **PV and DC bus to battery:** As the battery is low in SoC as well as PV source is generating less power, therefore DC bus and PV source together charge the battery at the rated current. The TPC operates as a DISO converter. This mode consists of four switching states, as shown in Fig. 5.9 and as follows:

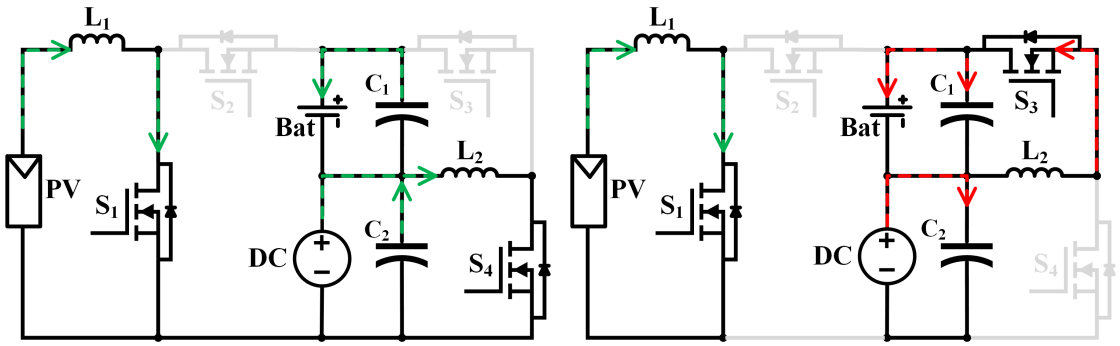

(a) State I (b) State II

(c) State III (d) State IV

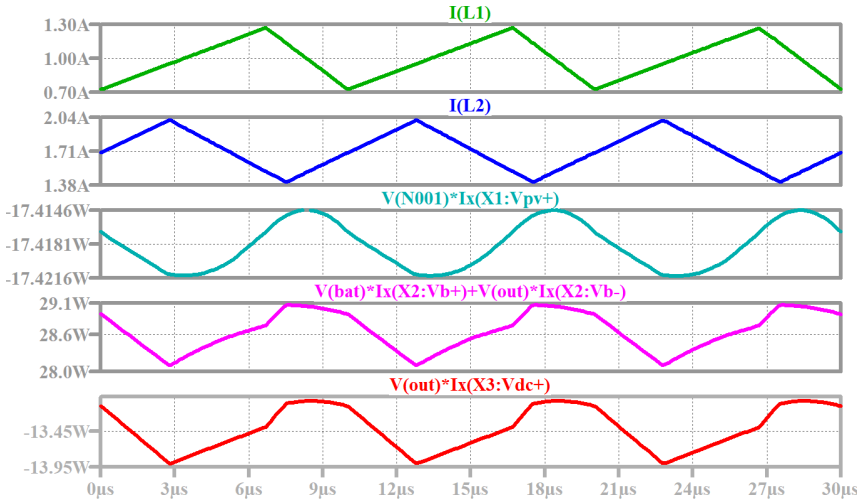

(e) Waveforms

Fig 5.9: Type I-III-IC circuit Mode 7 DISO.

State I $[t_0 < t < t_1]$: S_1 and S_4 are turned ON while S_2 and S_3 are OFF. The PV source starts to charge L_1 where $I_{L_1} = I_{PV}$. In addition, L_2 starts to be charged from the DC bus via S_4 where $I_{L_2} = I_{DC} + I_{C_2}$, as shown in Fig. 5.9(a). When S_4 turns OFF at $t = t_1$, this state ends.

State II $[t_1 < t < t_2]$: S_1 and S_3 are turned ON while S_2 and S_4 are OFF. L_1 continues to be charged from the PV source and L_2 starts to discharge into the battery, as shown in Fig. 5.9(b). When S_1 turns OFF at $t = t_2$, this state ends.

State III $[t_2 < t < t_3]$: S_2 and S_3 are turned ON while S_1 and S_4 are OFF. L_1 starts to discharge into the battery via S_2 and L_2 continues to discharge into the battery, as shown in Fig. 5.9(c). When S_4 turns ON at $t = t_3$, this state ends.

State IV $[t_3 < t < t_4]$: S_2 and S_4 are turned ON while S_1 and S_3 are OFF. L_1 continues to discharge into the battery and L_2 starts be charged from DC bus, as shown in Fig. 5.9(d). When S_1 turns ON at $t = t_4$, this state ends. The simulation waveforms are shown in Fig. 5.9(e).

5.5 Summary

This chapter studied all possible power flow graphs more specifically those converters having three power flow subgraphs. Each of these configurations has been studied, and circuit realisation has been done. Additionally, a comparison is carried out for all these useful configurations.

Chapter 6

A New Three-Port Converter Based on Type I-III-IA

6.1 Introduction

This chapter focuses on one of the most appropriate power flow configurations, namely, Type I-III-IA of Fig. 3.11(b). While other configurations, i.e., Types II-IIA, II-IIB and II-IIC, require two power processing stages between some ports, this configuration (I-III-IA) requires only one power processing stage between any two ports to achieve high efficiency and complete control of the ports. Table 6.1 shows a detailed comparison of different TPC topologies. Motivated by all the challenges and limitations described in Table 6.1, this chapter proposes a new TPC with two bidirectional ports having a lower component count. Additionally, a simple switching control scheme has been applied to achieve a smooth transition (i.e., no evident overshoot or undershoot and fast settling time) between different modes of operation. The contributions of this work are summarised as follows:

- This work considers two bidirectional ports with a lower component count than reported topologies.

Table 6.1: Comparison table of the proposed topology with previous topologies.

Topology	Structure	Number of inductors	Number of capacitors	Number of semiconductors	Rated Power	Power density $\frac{W}{cm^3}$	Average Efficiency η	Switching frequency
[80]	Unidirectional (3M°)	2	3	3 Switches, 5 diodes	250W	N/A	N/A	50kHz
[99]	Unidirectional (3M°)	(3) CI*	5	3 Switches, 4 diodes	250W	N/A	94.3%*-95.5%•	20kHz
[52]	Unidirectional (3M°)	1, CI*	6	3 Switches, 5 diodes	300W	N/A	93.6%*-95.9%•	50kHz
[50]	Unidirectional (3M°)	2	3	3 Switches, 3 diodes	500W	N/A	96.4%*-97.2%•	100kHz
[76]	Unidirectional (4M°)	1, CI*,	5	2 Switches, 2 diodes	500W	N/A	84.9%*-89.4%•	15kHz
[100]	Unidirectional (4M°)	2, (2) CI*	3	3 Switches, 3 diodes	200W	0.18	93.3%*-95.5%•	100kHz
[101]	Unidirectional (5M°)	(1), CI*	3	4 Switches, 3 diodes	180W	0.31	93.9%*-94.3%•	100kHz
[55]	Unidirectional (6M°)	CI*	3	3 Switches, 1 diode	60W	0.08	90.8%*-95.5%•	50kHz
[70]	Bidirectional (4M°)	CI*	4	4 Switches, 1 diode	180W	0.16	81%*-88.3%•	50kHz
[56]	Bidirectional (7M°)	2, 2°	3, 3°	4 Switches, 2 diodes	50W	N/A	89.4%*-93.2%•	100kHz
[102]	Bidirectional (7M°)	1	3	4 Switches, 5 diodes	50W	N/A	87.8%*-93%•	20kHz
[103]	Bidirectional (7M°)	2	3	4 Switches, 1 diode	30W	0.09	N/A	50kHz
Proposed	Bidirectional (7M°)	2	3	3 Switches, 1 diode	100W	0.21	90.5%*-95.3%•	50kHz

° Modes of operation * Coupled-inductor ° Soft switching

* Mode with lowest η
• Mode with highest η

- The proposed power flow configuration, Type I-III-IA in Fig. 3.11(b), has the advantage of a single power processing feature for all ports with a minimum number of converters.
- The proposed structure allows easier insertion of the buck-boost converter to connect the battery and the DC bus, thus providing a wide voltage range of battery operation, either lower or higher than the DC bus voltage.
- Seamless and smooth transition between seven modes of operation is achieved.

This chapter is organised as follows: in Section 6.2, the circuit design, principles of operation and working conditions of Type I-III-IA configuration are studied. In Section 6.3, the design guidelines for selecting the inductors and the capacitors are provided. In Section 6.4, the control structure and mode selection are explained. In Section 6.5, the experimental setup and measured waveforms are presented, followed by a summary in Section 6.6.

6.2 Principles of Operation and Steady-State Analysis of Type I-III-IA

In the proposed circuit, there are two input sources, namely the PV source and the battery. A unidirectional input port is connected to the PV source, while a

bidirectional port is connected to the DC bus and the battery. There are indeed cases where the PV voltage is less than the DC bus or battery voltage, which would require a voltage boosting conversion. However, there are also PV panels such as LG365Q1C-V5, and LG370Q1C-V5 which have V_{mpp}= 36.7V and V_{mpp} = 37V respectively. For powering the system with standard 12V or 24V battery and DC-bus system, a buck converter is necessary. This chapter focuses on the latter scenario. The battery is connected to the DC bus using a bidirectional buck-boost converter, as shown in Fig. 6.1. This section provides a detailed study about the different operations of the modes, LTspice© simulation and steady-state analysis. The experimental verification of the proposed converter and in-depth analysis has been undertaken in Section 6.5. The proposed converter can be used in PV-battery powered DC systems. According to the design requirement, the converter operates in continuous conduction mode (CCM).

The proposed TPC has seven modes of operation. The detailed working states of these switches are briefly discussed with the help of Table 6.2. Finally, all the modes are explained in detail as follows:

1. **PV to DC bus and battery:** The PV source provides power to the battery

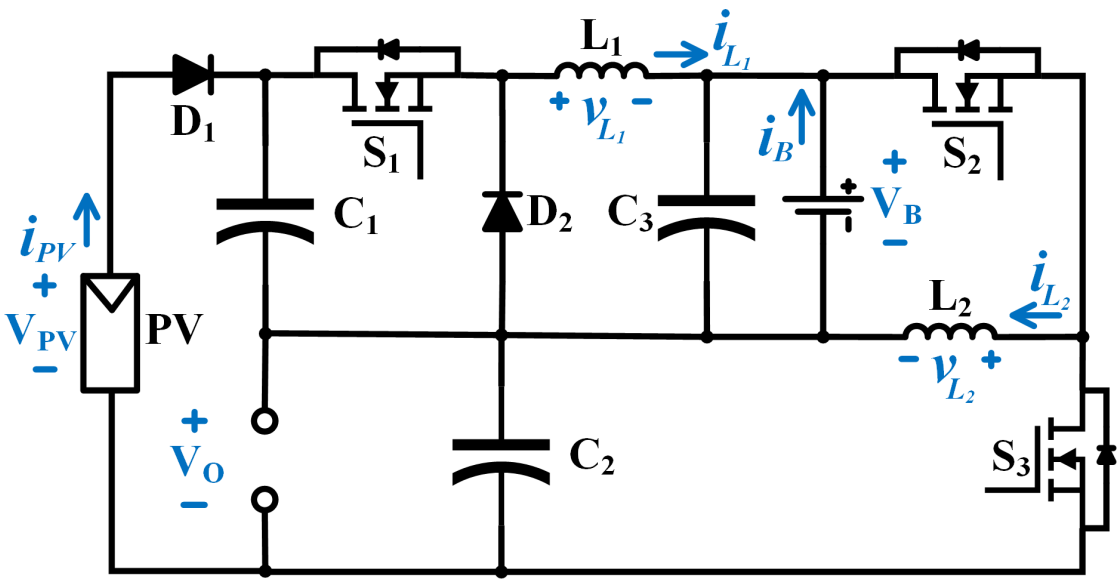

Fig 6.1: The proposed circuit of Type I-III-IA.

and DC bus by operating as a SIDO converter. Fig. 6.2 shows two switching states and is explained as follows:

State I $[t_0 < t < t_1]$: S_1 is turned ON. The PV source starts to charge L_1 where $I_{L_1} = I_{PV} + I_{C_1}$. D_1 is forward biased, and D_2 is reverse-biased, as shown in Fig. 6.2(a). When S_1 turns OFF at $t = t_1$, this state ends.

State II $[t_1 < t < t_2]$: S_1 is turned OFF. L_1 starts to discharge to the battery via D_2, as shown in Fig. 6.2(b). When S_1 turns ON at $t = t_2$, this state ends.

2. **Battery to DC bus**: During heavily shaded conditions or nighttime, the PV source cannot supply power to the DC bus. However, the power is supplied to the DC bus through the battery. The TPC operates as a SISO converter. Fig. 6.3 shows two switching states, which are explained as follows:

   State I $[t_0 < t < t_1]$: S_2 is turned ON while S_3 is OFF. The battery and C_3 start to charge L_2, as shown in Fig. 6.3(a). The voltage across L_2 is given by $v_{L_2} = V_B$. The capacitor C_2 is discharging to the DC bus. When S_2 turns OFF at $t = t_1$, this state ends.

   State II $[t_1 < t < t_2]$: S_3 is turned ON while S_2 is OFF. L_1 starts to discharge into the DC bus, as shown in Fig. 6.3(b). The voltage across L_2 is given by $v_{L_2} = -V_{DC}$. When S_2 turns ON at $t = t_2$, this state ends.

3. **DC bus to battery**: During heavily shaded conditions or nighttime, the PV source cannot supply power to the DC bus. On the other hand, the battery is also low in SoC. Therefore, the DC bus charges the battery. The TPC operates

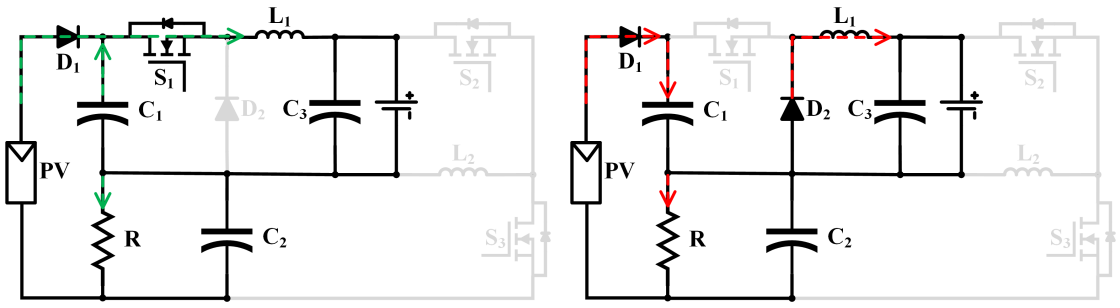

(a) State I (b) State II

Fig 6.2: Mode 1 SIDO.

as a SISO converter. Fig. 6.4 shows two switching states and is explained as follows:

State I $[t_0 < t < t_1]$: S_3 is turned ON while S_2 is OFF. The DC bus and C_3 start to charge L_2, as shown in Fig. 6.4(a). When S_3 turns OFF at $t = t_1$, this state ends. **State II** $[t_1 < t < t_2]$: S_3 is turned OFF, and S_2 is ON. L_1 starts to discharge into C_3 and the battery, as shown in Fig. 6.4(b). When S_3 turns ON at $t = t_2$, this state ends.

4. **PV and battery to DC bus**: In this mode, the PV source is generating less power than the power required by the DC bus. In this scenario, the battery provides the remaining power to the DC bus. The TPC operates as a DISO converter. This mode consists of four switching states, as shown in Fig. 6.5 and as follows:

   State I $[t_0 < t < t_1]$: S_1 and S_2 are turned ON while S_3 is OFF. The PV source starts to charge L_1. In addition, L_2 starts to get charged from the

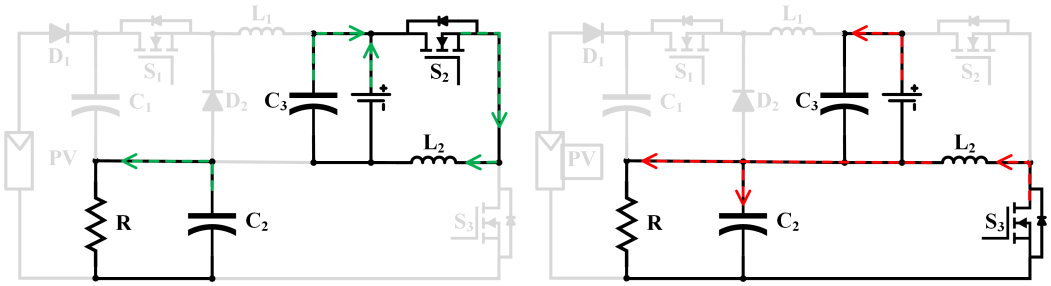

(a) State I (b) State II

Fig 6.3: Mode 2 SISO.

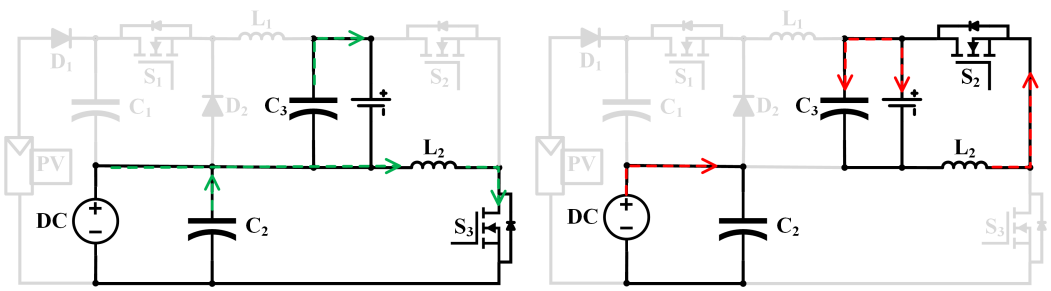

(a) State I (b) State II

Fig 6.4: Mode 3 SISO.

battery via S_2, as shown in Fig. 6.5(a). When S_2 turns OFF at $t = t_1$, this state ends.

State II $[t_1 < t < t_2]$: S_1 and S_3 are turned ON while S_2 is OFF. L_1 continues to be charged from the PV source, and L_2 starts to discharge, as shown in Fig. 6.5(b). When S_1 turns OFF at $t = t_2$, this state ends.

State III $[t_2 < t < t_3]$: S_1 and S_2 are turned OFF while S_3 is ON. L_1 starts to discharge into the battery via D_2 and L_2 continues to discharge into the DC bus, as shown in Fig. 6.5(c). When S_2 turns ON at $t = t_3$, this state ends.

State IV $[t_3 < t < t_4]$: S_1 and S_3 are turned OFF while S_2 is ON. The battery and L_1 continue to discharge into L_2, as shown in Fig. 6.5(d). When S_1 turns ON at $t = t_4$, this state ends. The LTspice© simulation waveforms are shown in Fig. 6.5(e).

5. **PV and DC bus to battery**: As the battery has a low SoC and the PV source generates lower power, the DC bus and PV source charge the battery at the rated current. The TPC operates as a DISO converter. This mode consists of four switching states, as shown in Fig. 6.6 and as follows:

   State I $[t_0 < t < t_1]$: S_1 and S_3 are turned ON while S_2 is OFF. The PV source starts to charge L_1 where $I_{L_1} = I_{PV} + I_{C_1}$. In addition, L_2 starts to be charged from the DC bus via S_3 where $I_{L_2} = I_B + I_{DC} + I_{C_2}$, as shown in Fig. 6.6(a). When S_3 turns OFF at $t = t_1$, this state ends.

   State II $[t_1 < t < t_2]$: S_1 and S_2 are turned ON while S_3 is OFF. L_1 continues to be charged from the PV source and L_2 starts to discharge, as shown in Fig. 6.6(b). When S_1 turns OFF at $t = t_2$, this state ends.

   State III $[t_2 < t < t_3]$: S_1 and S_3 are turned OFF while S_2 is ON. L_1 starts to discharge into the battery via D_2 and L_2 continues to discharge into the battery, as shown in Fig. 6.6(c). When S_3 turns ON at $t = t_3$, this state ends.

   State IV $[t_3 < t < t_4]$: S_1 and S_2 are turned OFF while S_3 is ON. L_1 continues to discharge into the battery, and L_2 starts to charge from the DC bus, as shown in Fig. 6.6(d). When S_1 turns ON at $t = t_4$, this state ends.

The LTspice© simulation waveforms are shown in Fig. 6.6(e).

6. **PV to DC bus:** In this mode, the battery is fully charged, or at the present maximum SoC; therefore, the PV source supplies the power to the DC bus only. The TPC operates as a SISO converter. This mode consists of four switching states, as shown in Fig. 6.7 and as follows:

   State I $[t_0 < t < t_1]$: S_1 and S_2 are turned ON while S_3 is OFF. The PV

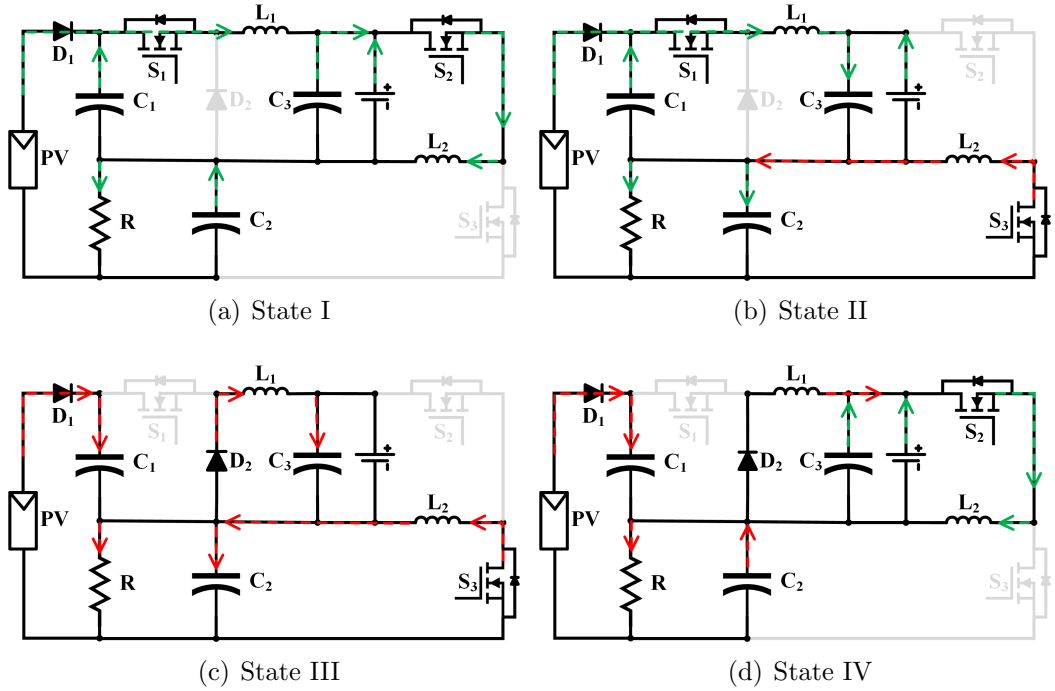

(a) State I (b) State II

(c) State III (d) State IV

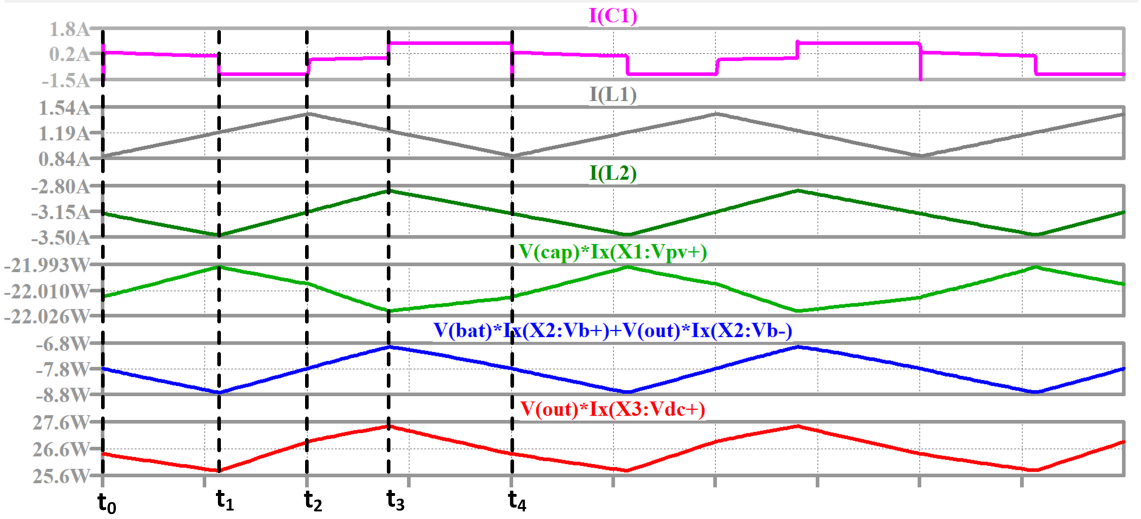

(e) Waveforms

Fig 6.5: Mode 4 DISO.

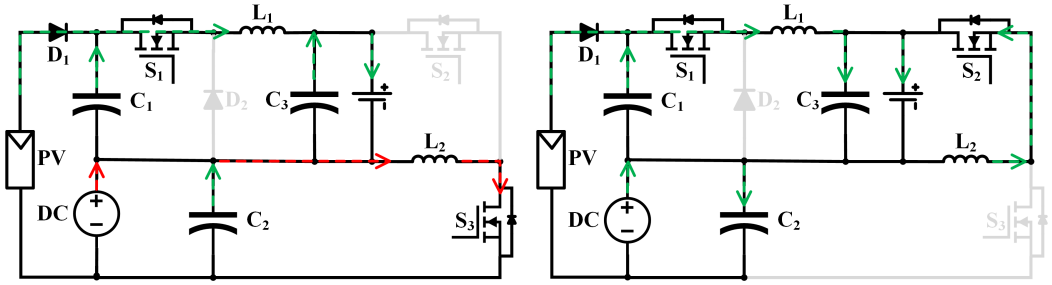

(a) State I

(b) State II

(c) State III

(d) State IV

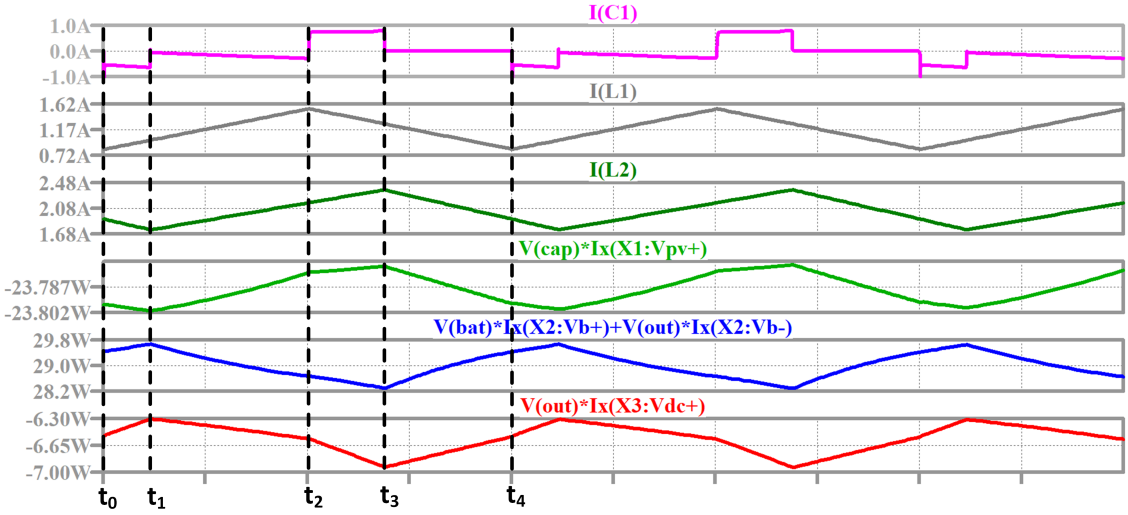

(e) Waveforms

Fig 6.6: Mode 5 DISO.

source starts to charge L_1 where $I_{L_1} = I_{PV} + I_{C_1}$ and L_2 where $I_{L_2} = I_{L_1} + I_{C_3}$, as shown in Fig. 6.7(a). When S_2 turns OFF at $t = t_1$, this state ends.

State II $[t_1 < t < t_2]$: S_1 and S_3 are turned ON while S_2 is OFF. L_1 continues to be charged from the PV source, and L_2 starts to discharge, as shown in Fig. 6.7(b). When S_1 turns OFF at $t = t_2$, this state ends.

State III $[t_2 < t < t_3]$: S_1 and S_2 are turned OFF while S_3 is ON. L_1 starts to discharge into C_3 via D_2, and L_2 continues to discharge into the DC bus,

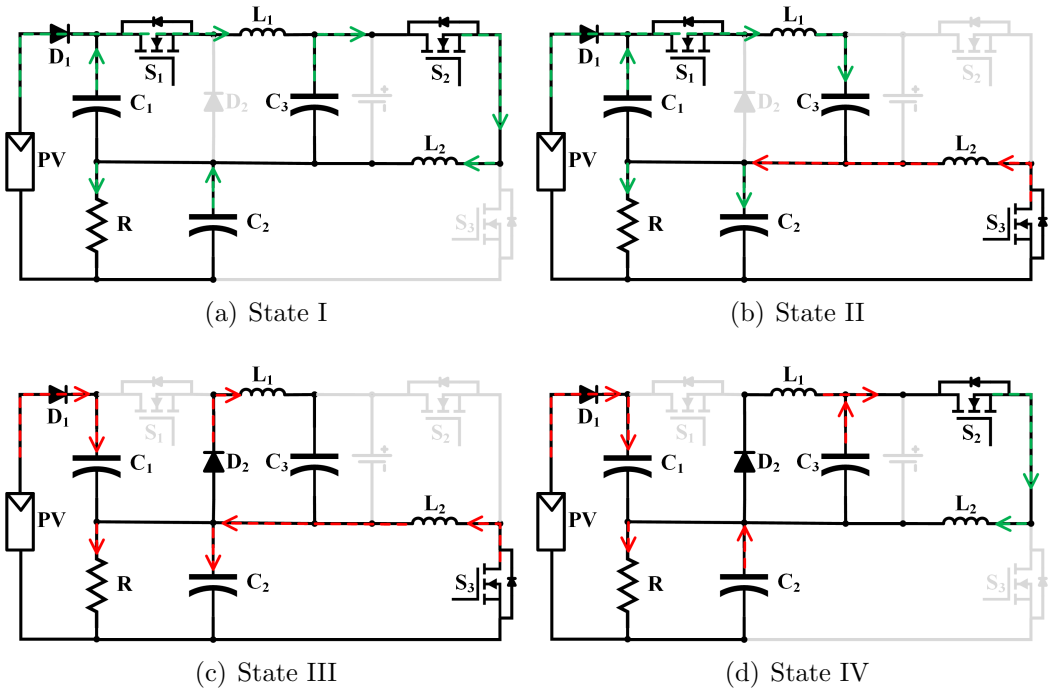

(a) State I (b) State II

(c) State III (d) State IV

Fig 6.7: Mode 6 SISO.

as shown in Fig. 6.7(c). When S_2 turns ON at $t = t_3$, this state ends.

State IV $[t_3 < t < t_4]$: S_1 and S_3 are turned OFF while S_2 is ON. C_3 and L_1 continue to discharge into L_2, as shown in Fig. 6.7(d). When S_1 turns ON at $t = t_4$, this state ends.

7. **PV to battery:** The PV source charges the battery at no load condition in this mode. The TPC operates as a SISO converter as a SISO converter. This mode consists of four switching states, as shown in Fig. 6.8 and as follows:

   State I $[t_0 < t < t_1]$: S_1 and S_3 are turned ON while S_2 is OFF. The PV source starts to charge L_1 where $I_{L_1} = I_{PV} + I_{C_1}$. In addition, L_2 starts to be charged from C_2 via S_3 where $I_{L_2} = I_B + I_{C_2}$, as shown in Fig. 6.8(a). When S_3 turns OFF at $t = t_1$, this state ends.

   State II $[t_1 < t < t_2]$: S_1 and S_2 are turned ON while S_3 is OFF. L_1 continues to be charged from the PV source, and L_2 starts to discharge, as shown in Fig. 6.8(b). When S_1 turns OFF at $t = t_2$, this state ends.

   State III $[t_2 < t < t_3]$: S_1 and S_3 are turned OFF while S_2 is ON. L_1 starts to discharge into the battery via D_2, and L_2 continues to discharge into the

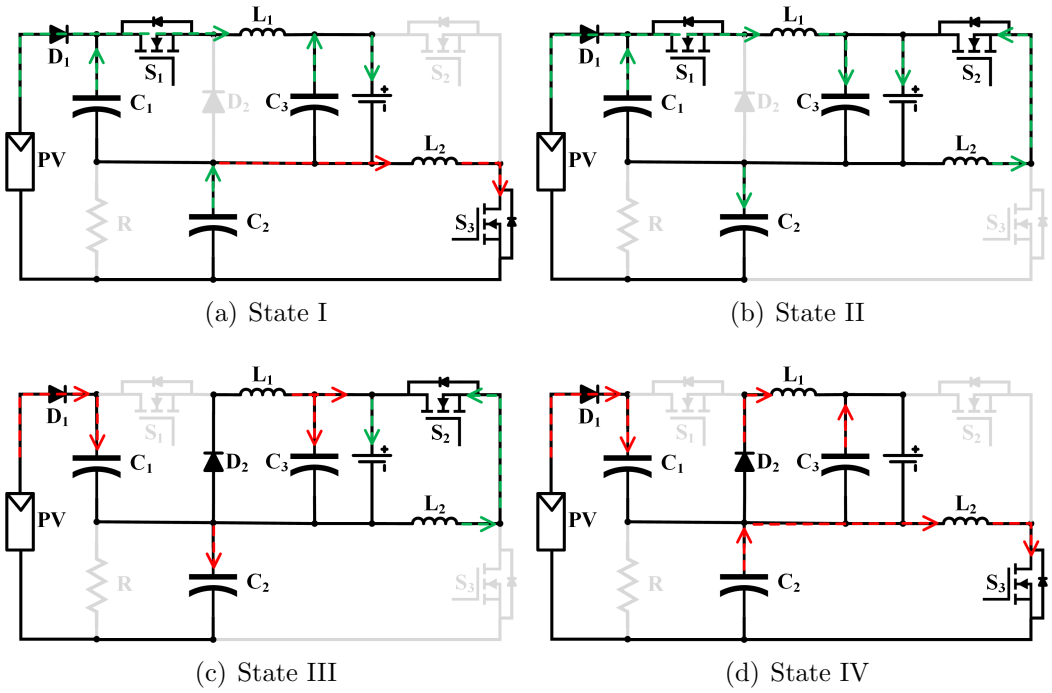

(a) State I (b) State II

(c) State III (d) State IV

Fig 6.8: Mode 7 SISO.

battery, as shown in Fig. 6.8(c). When S_3 turns ON at $t = t_3$, this state ends.

State IV $[t_3 < t < t_4]$: S_1 and S_2 are turned OFF while S_3 is ON. L_1 continues to discharge into the battery, and L_2 starts to charge from C_2, as shown in Fig. 6.8(d). When S_1 turns ON at $t = t_4$, this state ends.

6.3 Design Guidelines

6.3.1 Inductor Design

The minimum inductances for L_1 and L_2 are calculated in order to operate in CCM as follows:

$$L_1 = \frac{(V_{C_1} - V_B)}{\Delta i_{L_1} f} d_1 \tag{6.1}$$

$$L_2 = \frac{(V_B)}{\Delta i_{L_2} f} d_2 \tag{6.2}$$

where $V_{C_1}, V_B, d_1, d_2, \Delta i_{L_1}, \Delta i_{L_2}$, and f are the capacitor voltage, battery voltage, duty cycle of S_1, duty cycle of S_2, first inductor ripple current, second inductor

Table 6.2: Switching Look-up Table for Different Modes

Modes	Power	Active Components	State	Switch state ON	Switch state OFF	Diagram
1. PV to DC bus and battery	$P_{pv} = P_{DC} + P_B$	D_1, S_1, L_1, C_1, C_2 & C_3	I	S_1*	-	Fig. 6.2(a)
			II	-	S_1*	Fig. 6.2(b)
2. battery to DC bus	$P_B = P_{DC}$	S_2, S_3, L_2, C_2 & C_3	I	S_2*	S_3*	Fig. 6.3(a)
			II	S_3*	S_2*	Fig. 6.3(b)
3. DC bus to battery	$P_{DC} = P_B$	S_2, S_3, L_2, C_2 & C_3	I	S_3*	S_2*	Fig. 6.4(a)
			II	S_2*	S_3*	Fig. 6.4(b)
4. PV and battery to DC bus	$P_{pv} + P_B = P_{DC}$	All active	I	S_1*, S_2*	S_3*	Fig. 6.5(a)
			II	S_1*, S_3*	S_2*	Fig. 6.5(b)
			III	S_3*	S_1*, S_2*	Fig. 6.5(c)
			IV	S_2*	S_1*, S_3*	Fig. 6.5(d)
5. PV and DC bus to battery	$P_{pv} + P_{DC} = P_B$	All active	I	S_1*, S_3*	S_2*	Fig. 6.6(a)
			II	S_1*, S_2*	S_3*	Fig. 6.6(b)
			III	S_2*	S_1*, S_3*	Fig. 6.6(c)
			IV	S_3*	S_1*, S_2*	Fig. 6.6(d)
6. PV to DC bus	$P_{pv} = P_{DC}$	All active	I	S_1*, S_2*	S_3*	Fig. 6.7(a)
			II	S_1*, S_3*	S_2*	Fig. 6.7(b)
			III	S_3*	S_1*, S_2*	Fig. 6.7(c)
			IV	S_2*	S_1*, S_3*	Fig. 6.7(d)
7. PV to battery	$P_{pv} = P_B$	All active	I	S_1*, S_3*	S_2*	Fig. 6.8(a)
			II	S_1*, S_2*	S_3*	Fig. 6.8(b)
			III	S_2*	S_1*, S_3*	Fig. 6.8(c)
			IV	S_3*	S_1*, S_2*	Fig. 6.8(d)

* Receiving PWM signal,

ripple current, and switching frequency.

6.3.2 Capacitor Design

The minimum capacitances are calculated in order to maintain the voltage ripple under 1% as follows:

$$C_1 = \frac{(1-d_1)(V_{PV} - V_{DC})}{Rf\Delta V_{C1}} \tag{6.3}$$

$$C_2 = \frac{d_2 V_o}{Rf\Delta V_o} \tag{6.4}$$

$$C_3 = \frac{(1-d_1)V_B}{8L_1 f^2 \Delta V_B} \tag{6.5}$$

where V_{PV}, V_{DC}, and R are the PV voltage, DC bus voltage, and output resistance.

6.3.3 Component Stress Analysis and Limitation of Port Voltages

The voltage and current stresses for all semiconductor devices are explained in Table. 6.3. The PV voltage range can be expressed as follows:

$$V_{PV} = V_{DC} + \frac{V_B}{d_1} \tag{6.6}$$

Since battery range is 22V – 29.4V and the DC bus is 24V with +/- 2V, the PV voltage range is therefore between 49V (at 0.9 max. duty cycle) and 82V (open circuit voltage or max S_1 breakdown voltage).

Table 6.3: Component stress of all power devices.

	S1	**S2**	**S3**	**D1**	**D2**
Voltage stress	$V_{C1} + V_{D2}$	$V_B + V_o$	$V_B + V_o$	$V_{PV} - V_{C1} - V_o$	$V_{C1} + V_{DS1}$
Current stress	$I_{C1} + I_{PV}$	$I_B + I_{L1}$	I_o	I_{PV}	I_B

6.4 Mode Selection and Control

The proposed TPC is constructed based on basic buck-boost and buck converters. S_2 and S_3 are working complementary during different modes. The control objectives comprise MPPT, battery protection and output voltage regulation. MPPT is achieved through the first switch S_1, while S_2 and S_3 are responsible for both battery regulation and output voltage regulation (PI controller). To control the proposed TPC, a DSP controller (TMS320F28379D) is used as shown in Fig. 6.10. Detailed working states of these switches can be briefly described in Table 6.2. In Mode 1, the buck converter is receiving PWM signals. However, in Modes 2 and 3, the buck-boost converter receives PWM signals as the PV power is under the threshold for a long time. from Mode 4 to Mode 7, all switches receive PWM signals. However, some switches are turned ON to ensure a single power processing stage for all

seven modes. Therefore, these modes are selected automatically depending upon the available power and load power demand [103].

There are several challenges, including switching requirements in different modes, to design a proper switching strategy. In this TPC, a smooth transition is achieved using a single switching pattern for all modes, so the transition between modes will occur based on the available power among the ports. For example, in the battery to DC bus mode, the power is transferred by S_2 and S_3 while no power is transferred by S_1 as there is no PV power. However, during nighttime or heavily shaded conditions, the PV power is not available for a long time. Therefore, the buck converter turns OFF until the PV power is above the threshold. This switching strategy must have the ability to optimise the conversion efficiency and manage the system delays and fulfil the control objectives. The flowchart of the proposed circuit with different conditions to implement all seven modes of operation is shown in Fig. 6.9. Referring to the flowchart, mode selection conditions are summarised as follows:

- **No PV power:** When there is no PV power, there are three scenarios. First, the battery can supply the required power at the DC bus. Second, the battery is unable to provide enough power to the DC bus. Therefore, the DC bus is charging the battery. Finally, the battery reaches the discharge limit, the DC bus cannot charge the battery, and the system will shut down.

- **No load (PV to battery):** There are three scenarios. First, the PV power under MPPT is less than the maximum battery′s power. Second, no MPPT is activated when the PV′s power is more than the battery. Finally, the battery reaches the charging limit, and the system will shut down to protect the battery.

- **PV power > DC power:** The PV power is sufficient to satisfy the DC bus demand, and the surplus power goes to the battery. There are two scenarios; first, MPPT is applied when the remaining power is less than the maximum

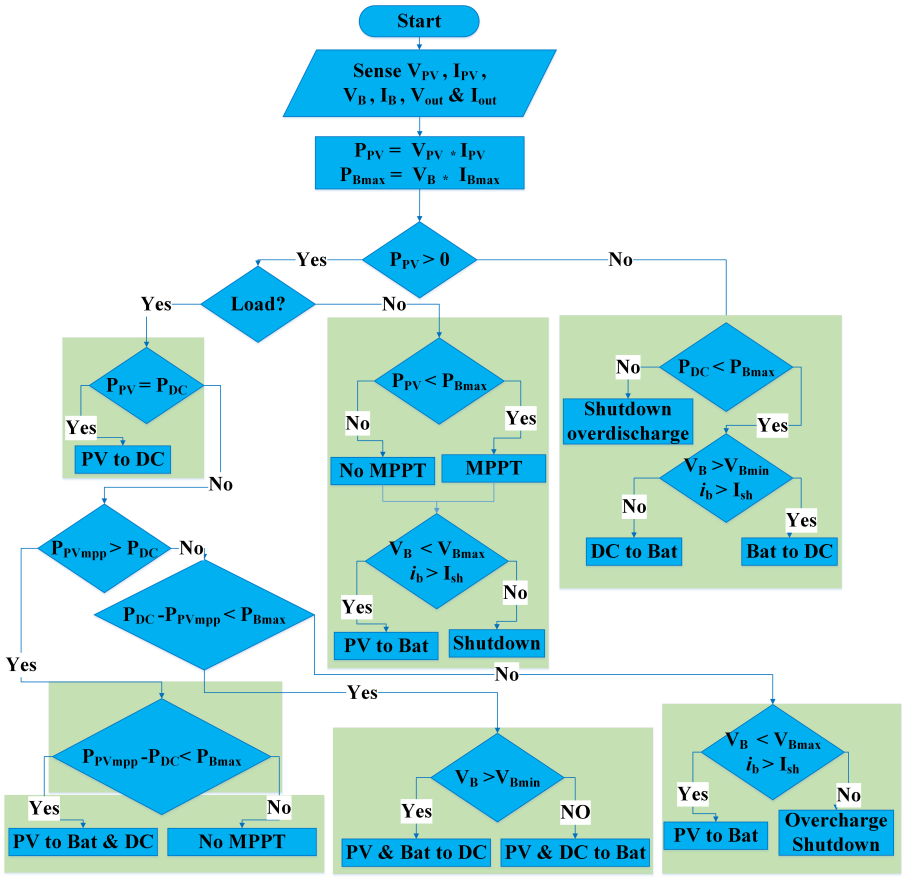

Fig 6.9: Flowchart of the proposed circuit with different conditions to implement all 7 modes of operation.

battery power; second, no MPPT is applied when the remaining power exceeds the maximum battery power.

- **PV power < DC power:** The PV power cannot satisfy the DC bus, and the deficit power comes from the battery. There are two scenarios. First, $P_{DC} - P_{PV} < P_{Bmax}$; second, the DC bus can supply the battery with the remaining power.

- **DC power − PV power > Maximum battery power:** The PV power cannot satisfy the DC bus, and the deficit power is more than the maximum available battery power. There are two scenarios; first, the PV power charges the battery as long as it is below the limit; second, the battery reaches the charging limit and the system shuts down to protect the battery.

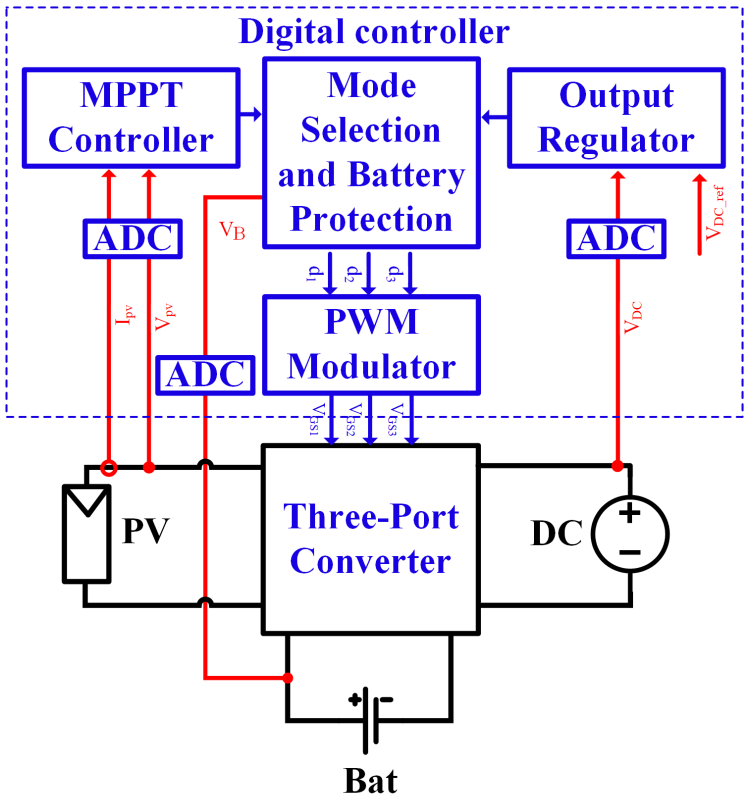

Fig 6.10: Control structure of the proposed TPC.

6.5 Experimental Results

The experimental setup of the proposed circuits is shown in Fig. 6.11(a). The hardware prototype of the proposed circuit is constructed as in Fig. 6.11(b). Table 6.4, shows a list of all components used in the proposed circuit and the schematic diagram of the proposed circuit is shown in Fig. 6.12. A laboratory prototype of 100W is designed to verify the presented concept. The experimental waveforms and transient responses during mode transition for the proposed converter are shown in Fig. 6.13.

A PV emulator is used to mimic the behaviour of the PV panel. Simple Perturb and Observe (P&O) algorithm is used to achieve MPPT where $V_{MPP} = 73$ V. The first bidirectional port is connected to the battery, and the second bidirectional port is connected to an electronic load which is programmed as a constant resistance (CR). In Fig. 6.13, each graph contains four waveforms, from channel 1 to channel 4 are PV current, output voltage, second inductor current and battery current.

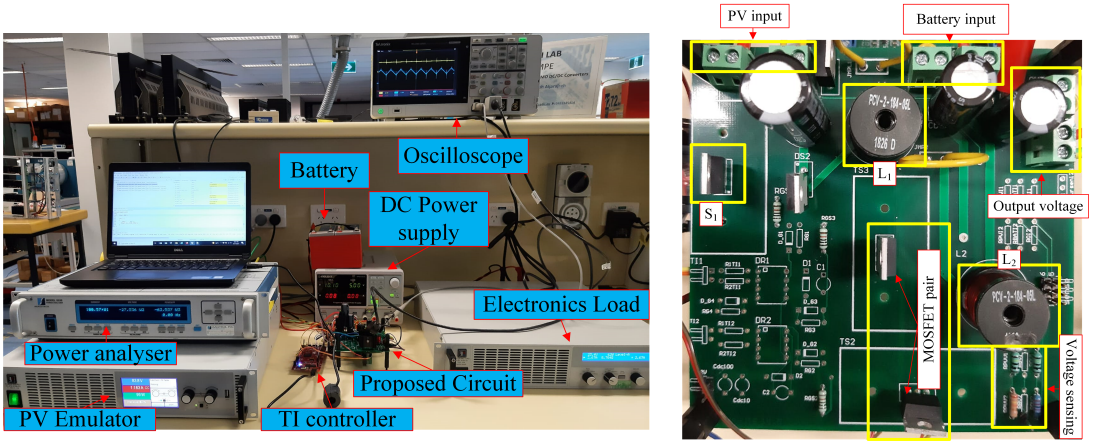

(a) Experimental setup (b) Prototype of TPC

Fig 6.11: Experimental prototype.

The transition response of the proposed converter is shown in Fig. 6.13. Fig. 6.13(a) shows a step response from the PV emulator with no load. As there is no load, the PV power is transferred to the battery, and if there is no power from the PV source, the system will shut down. Fig. 6.13(b) shows a step response in the load at no PV power. The battery will supply the DC bus. Fig. 6.13(c) shows a step-change in the PV power to zero while the load is constant. First, the PV power is enough to satisfy the DC bus. Then, the PV power is stepped to zero and the battery supplies current to the DC bus. Fig. 6.13(d) shows a step-change in the PV power to zero while the load is constant. First, the PV power is enough to supply the battery and the DC bus. Then, the PV power is stepped to zero and the battery supplies current to the DC bus. Finally, Fig. 6.13(e) shows a continuous change in the PV power

Table 6.4: Component specification

Parameter	Value
Controller	TMS320f28379D
Battery	24 V, 7.2 A
PV emulator	ELEKTRO-AUTOMATIK EA-PSI 9360-15 (30 W)
Output	ELEKTRO-AUTOMATIK EA-EL 9750-25
MOSFETs	IRFB5620
D_1	STPS10L25D
L_1 and L_2	184 uH
C_1 and C_2	100 uF
f_s	50 KHz
C_3	120 uF

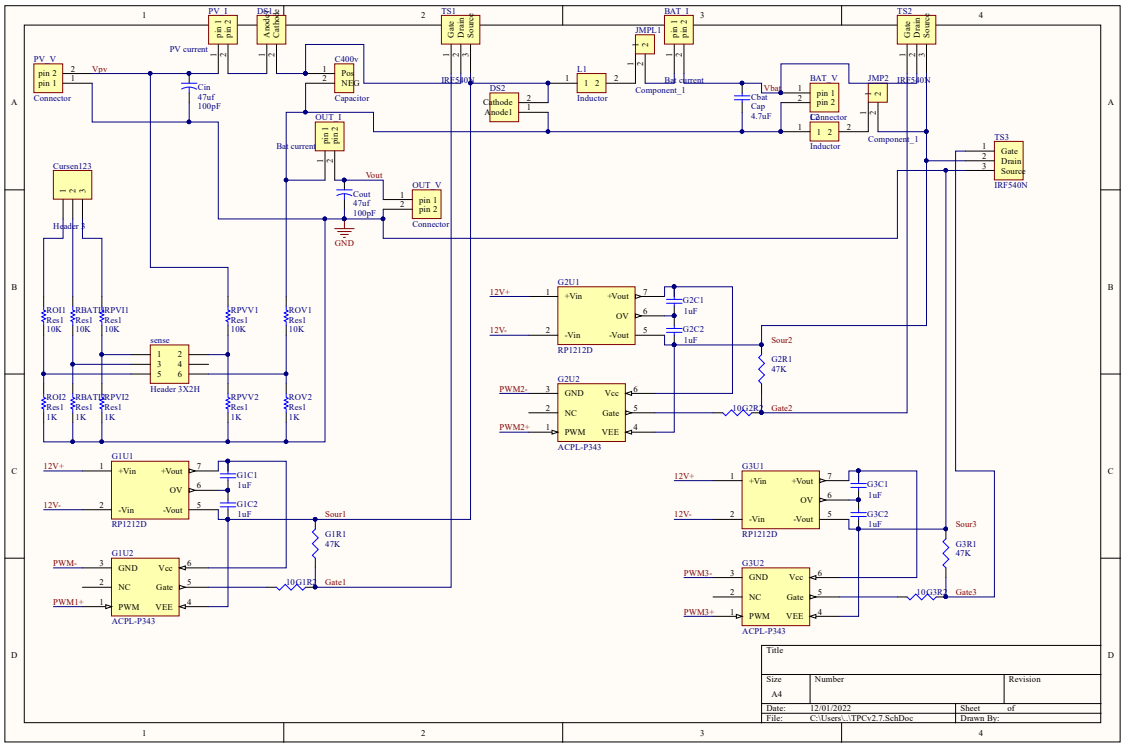

Fig 6.12: The schematic diagram of the proposed circuit.

to demonstrate the controllability of the converters in different modes. The power losses of each semiconductor device at different modes of operation is depicted in Fig. 6.14. The efficiency curves are plotted by measuring input/output power using a calibrated power analyser (MAGTROL 6530) for different modes of operation versus the rated power as shown in Fig. 6.15. An average of 93.4% efficiency at different modes of operation was achieved with a peak of 96.2% efficiency in battery to DC bus mode. It is worth noting that D_1 losses can be excluded from the efficiency graph in Fig. 6.15, as many PV panel consist a blocking diode internally. Furthermore, D_2 could be replaced with a MOSFET to improve the efficiency. Furthermore, a conventional Si MOSFETs are used in this circuit and due to the low dynamic performance of the intrinsic diode, the switching losses might increase significantly. In contrast, a snubber circuit or Silicon Carbide switch can improve the system efficiency.

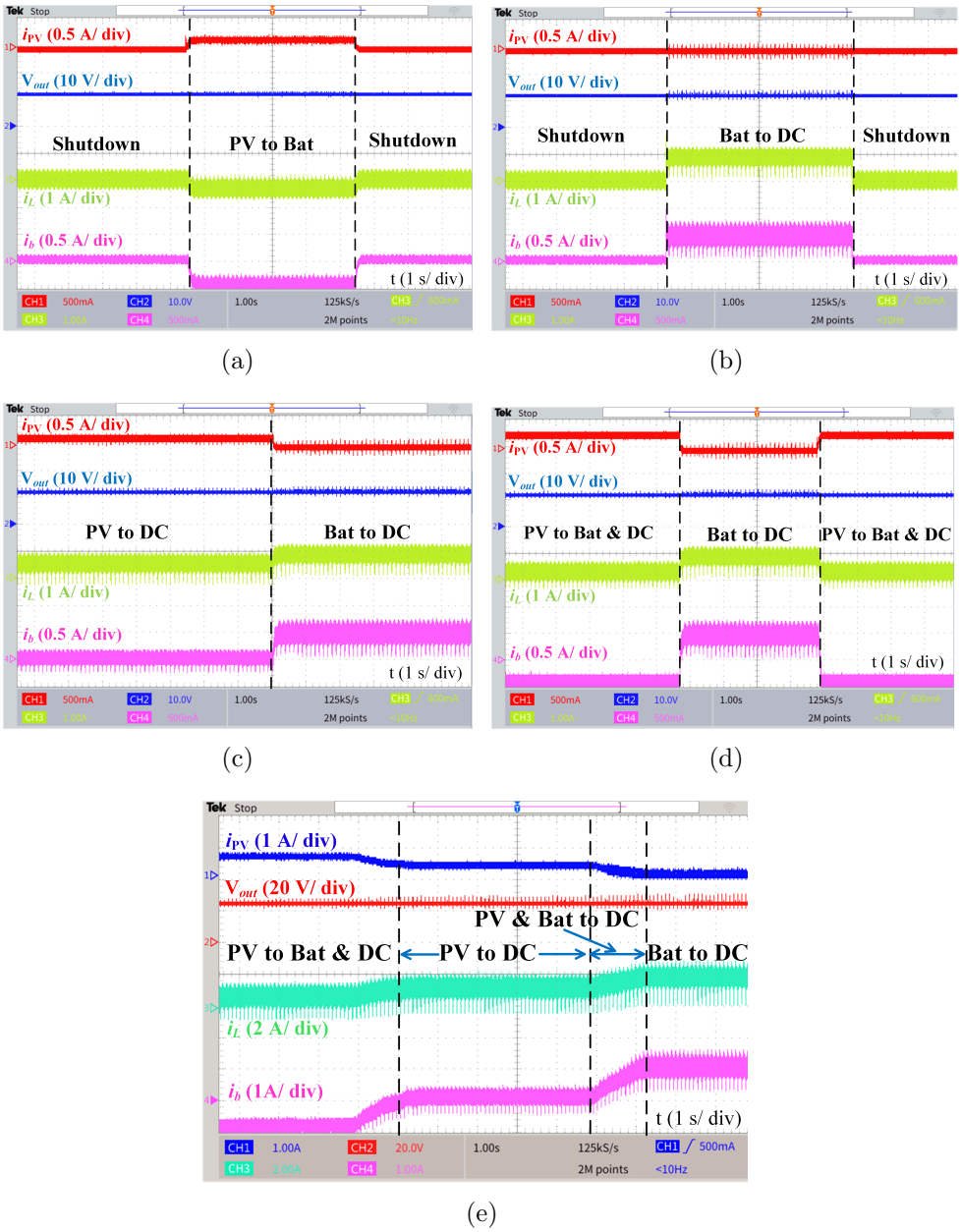

Fig 6.13: Waveforms of the transition between modes of the proposed converter.

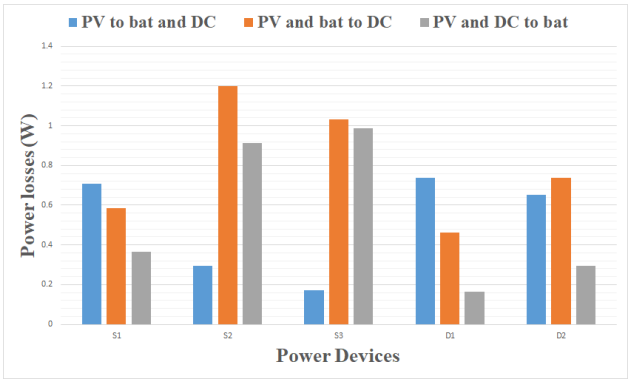

Fig 6.14: The power losses of different modes of operation.

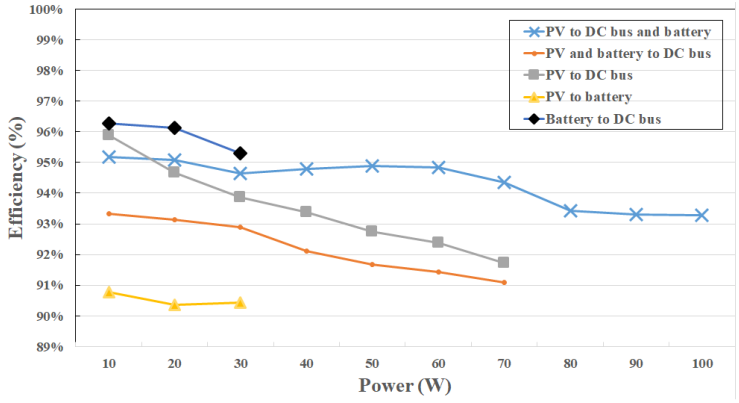

Fig 6.15: Conversion efficiency of different modes of operation.

6.6 Summary

A new non-isolated TPC with two bidirectional ports and a smaller number of components is presented. This configuration applies to both standalone and grid-connected applications; it works in seven different operational modes and allows MPPT, battery protection, and output voltage regulation to be achieved. Furthermore, smooth transitions (i.e., fast settling time and no obvious overshoot/undershoot) are achieved. Finally, experimental results in terms of steady-state operation and dynamic response are reported to verify the performance of the proposed TPC.

Chapter 7

Conclusion and Future Work

7.1 Conclusion

TPCs are widely employed in various applications and show better performance than traditional multiple SISO. TPCs are divided into isolated, partly-isolated and non-isolated types. These types of converters have been reviewed in Chapter 2. When galvanic isolation between any two ports is required, high-voltage gain and voltage matching can be achieved using isolated TPCs. However, using a multi-winding transformer and many active switches increases the cost and size of the converter. Partly-isolated TPCs can achieve a relatively higher voltage gain than non-isolated TPCs, and the isolation is set up between only two of the three available ports. In contrast, non-isolated TPCs are compact and cost-effective but can only be used where galvanic isolation is not required. However, designers should be aware of high power and safety requirements.

Chapter 3 presents a topological study to derive all possible TPCs by using power flow graphs. Based on two conventional DISO converters, TPC with a bidirectional output port are discussed in detail. Using power flow graphs minimises the number of possible converter candidates to select the best topology with the desired performance. The impractical configurations due to their indirect connection,

violating the circuit rules and multiple conversion stages have been eliminated.

In Chapter 4, a mechanism for ensuring fast and smooth transitions of operating modes for TPCs is presented. In addition, two bidirectional ports compared to only one bidirectional port in most reported topologies are considered. This configuration enables both standalone and grid-connected applications. MPPT, battery protection and output voltage regulation are achieved. In the proposed method, the number of switching patterns is significantly reduced, and decisions are simplified for all modes. The transitions between modes are achieved with fast settling time and minimal overshoot and undershoot. Based on the power availability and load demand, the mode is activated automatically. The proposed control strategy and mechanism for TPC have potential applications in the DC microgrid.

In Chapter 5, all possible power flow graphs are studied, specifically, those converters having three power subgraphs. Each of these configurations has been studied, and circuit realisation has been done. Additionally, a comparison is carried out for all these useful configurations.

In Chapter 6, a new non-isolated TPC with two bidirectional ports and a reduced number of components is presented. This configuration is applicable to both standalone and grid-connected applications and works in seven different modes of operation. MPPT, battery protection and output voltage regulation are achieved. Furthermore, smooth transitions (i.e., fast settling time and no apparent overshoot or undershoot) are achieved. Finally, experimental results in terms of steady-state operation and dynamic response are reported to verify the performance of the proposed TPC.

7.2 Future Work

In this thesis, TPCs with two bidirectional ports are investigated. Future work can be extended in several different directions. These directions include reducing

the number of switches in each topology, automating the derivation process, and extending the number and types of ports. The recommendations according to these directions are listed as follows:

- This work can be automated using a computer program not only to drive all possible topologies, but to also select the most viable topologies based on specific conditions.
- This thesis focuses on non-isolated TPCs, where this work can be further applied to cover all different TPCs.
- This work can be extended to converters where the number of input ports can be greater than 3. The reason behind this extension is the need for a system where more than one renewable energy source might be connected to more than one storage unit for any particular application.
- Furthermore, this work can also be extended to a mixture of DC and AC ports for grid-connected applications.
- This work can add some switches or energy storage units to each power flow, which will reduce the redundancy of more components where time sharing multiplexing is needed.

Bibliography

[1] A. M. Omer, "Energy, environment and sustainable development," *Renewable and sustainable energy reviews*, vol. 12, no. 9, pp. 2265–2300, 2008.

[2] Y. Mohammed, M. Mustafa, and N. Bashir, "Hybrid renewable energy systems for off-grid electric power: Review of substantial issues," *Renewable and Sustainable Energy Reviews*, vol. 35, pp. 527–539, 2014.

[3] H. Lund, "Renewable energy strategies for sustainable development," *Energy*, vol. 32, no. 6, pp. 912–919, 2007.

[4] "Power technology." http://www.power-technology.com/features/featurethe-worlds-most-used-renewable-power-sources-4160168/. Accessed: 2018-03-08.

[5] S. Sinha and S. Chandel, "Review of recent trends in optimization techniques for solar photovoltaic–wind based hybrid energy systems," *Renewable and Sustainable Energy Reviews*, vol. 50, pp. 755–769, 2015.

[6] R. Rajesh and M. C. Mabel, "A comprehensive review of photovoltaic systems," *Renewable and sustainable energy reviews*, vol. 51, pp. 231–248, 2015.

[7] Q. Mei, X. Zhen-Lin, and W.-Y. Wu, "A novel multi-port dc/dc converter for hybrid renewable energy distributed generation systems connected to power grid," in *2008 IEEE International Conference on Industrial Technology*, pp. 1–5, IEEE, 2008.

[8] H.-J. Chiu, C.-J. Yao, and Y.-K. Lo, "A dc/dc converter topology for renewable energy systems," *International journal of circuit theory and applications*, vol. 37, no. 3, pp. 485–495, 2009.

[9] L. An and D. D.-C. Lu, "Design of a single-switch dc/dc converter for a pv-battery-powered pump system with pfm+ pwm control," *IEEE Transactions on Industrial Electronics*, vol. 62, no. 2, pp. 910–921, 2015.

[10] H. Wang, M. Liserre, and F. Blaabjerg, "Toward reliable power electronics: Challenges, design tools, and opportunities," *IEEE Industrial Electronics Magazine*, vol. 7, no. 2, pp. 17–26, 2013.

[11] Y. Yang, H. Wang, A. Sangwongwanich, and F. Blaabjerg, "Design for reliability of power electronic systems," in *Power Electronics Handbook (Fourth Edition)*, pp. 1423–1440, Elsevier, 2018.

[12] S. Lu, K. Sun, H. Shi, S. Jiang, and Y. W. Li, "Comparison of high power dc-dc converters for photovoltaic generation integrated into medium voltage dc grids," in *2018 IEEE International Power Electronics and Application Conference and Exposition (PEAC)*, pp. 1–6, 2018.

[13] M. Vilathgamuwa, D. Nayanasiri, and S. Gamini. 2015.

[14] K. Mozaffari and M. Amirabadi, "A highly reliable and efficient class of single-stage high-frequency ac-link converters," *IEEE Transactions on Power Electronics*, vol. 34, no. 9, pp. 8435–8452, Sept 2019.

[15] A. K. Bhattacharjee, N. Kutkut, and I. Batarseh, "Review of multiport converters for solar and energy storage integration," *IEEE Transactions on Power Electronics*, vol. 34, no. 2, pp. 1431–1445, 2018.

[16] X. L. Li, Z. Dong, C. K. Tse, and D. D.-C. Lu, "Single-inductor multi-input multi-output dcdc converter with high flexibility and simple control," *IEEE Transactions on Power Electronics*, vol. 35, no. 12, pp. 13104–13114, Dec 2020.

[17] Z. Dong, Z. Li, X. L. Li, C. K. Tse, and Z. Zhang, "Single-inductor multiple-input multiple-output converter with common ground, high scalability, and no cross-regulation," *IEEE Transactions on Power Electronics*, vol. 36, no. 6, pp. 6750–6760, Jun 2021.

[18] K. Sun, L. Zhang, Y. Xing, and J. M. Guerrero, "A distributed control strategy based on dc bus signaling for modular photovoltaic generation systems with battery energy storage," *IEEE Transactions on Power Electronics*, vol. 26, no. 10, pp. 3032–3045, 2011.

[19] F. Locment, M. Sechilariu, and I. Houssamo, "Dc load and batteries control limitations for photovoltaic systems. experimental validation," *IEEE Transactions on Power Electronics*, vol. 27, no. 9, pp. 4030–4038, 2012.

[20] B. G. Dobbs and P. L. Chapman, "A multiple-input dc/dc converter topology," *IEEE Power Electronics Letters*, vol. 1, no. 1, pp. 6–9, 2003.

[21] H. Tao, A. Kotsopoulos, J. L. Duarte, and M. A. Hendrix, "Family of multiport bidirectional dc–dc converters," *IEE Proceedings-Electric Power Applications*, vol. 153, no. 3, pp. 451–458, 2006.

[22] Z. Zhou, H. Wu, X. Ma, and Y. Xing, "A non-isolated three-port converter for stand-alone renewable power system," in *IECON 2012-38th Annual Conference on IEEE Industrial Electronics Society*, pp. 3352–3357, IEEE, 2012.

[23] H. Wu, Y. Xing, Y. Xia, and K. Sun, "A family of non-isolated three-port converters for stand-alone renewable power system," in *IECON 2011-37th Annual Conference on IEEE Industrial Electronics Society*, pp. 1030–1035, IEEE, 2011.

[24] N. Zhang, D. Sutanto, and K. M. Muttaqi, "A review of topologies of three-port dc–dc converters for the integration of renewable energy and energy storage system," *Renewable and Sustainable Energy Reviews*, vol. 56, pp. 388–401, 2016.

[25] N. D. Dao, D. C. Lee, and Q. D. Phan, "High-efficiency sic-based isolated three-port dc/dc converters for hybrid charging stations," *IEEE Transactions on Power Electronics*, vol. 35, no. 10, pp. 10455 – 10465, Oct. 2020.

[26] G. R. C. Mouli, J. Schijffelen, M. van den Heuvel, M. Kardolus, and P. Bauer, "A 10 kw solar-powered bidirectional ev charger compatible with chademo and combo," *IEEE Transactions on Power Electronics*, vol. 34, no. 2, pp. 1082–1098, Feb. 2019.

[27] D.-D. Nguyen, G. Fujita, and M. C. Ta, "A new soft-switching strategy for three-port converter to be applied in ev application," in *2017 IEEE 3rd International Future Energy Electronics Conference and ECCE Asia (IFEEC 2017-ECCE Asia)*, pp. 1126–1131, IEEE, 2017.

[28] S.-K. Kim, J.-H. Jeon, C.-H. Cho, J.-B. Ahn, and S.-H. Kwon, "Dynamic modeling and control of a grid-connected hybrid generation system with versatile power transfer," *IEEE Transactions on Industrial Electronics*, vol. 55, no. 4, pp. 1677–1688, Apr. 2008.

[29] D. Li, Y. Xuan, Q. Li, and H. Hong, "Exergy and energy analysis of photovoltaic-thermoelectric hybrid systems," *Energy*, vol. 126, pp. 343–351, 2017.

[30] K. Jin, X. Ruan, M. Yang, and M. Xu, "A hybrid fuel cell power system," *IEEE Transactions on Industrial Electronics*, vol. 56, no. 4, pp. 1212–1222, Apr. 2009.

[31] K. R. Sree, A. K. Rathore, E. Breaz, and F. Gao, "Soft-switching non-isolated current-fed inverter for pv/fuel cell applications," *IEEE Transactions on Industry Applications*, vol. 52, no. 1, pp. 351–359, Feb 2016.

[32] Z. Wang, Q. Luo, Y. Wei, D. Mou, X. Lu, and P. Sun, "Topology analysis and review of three-port dcdc converters," *IEEE Transactions on Power Electronics*, vol. 35, no. 11, pp. 11783–11800, Nov, 2020.

[33] A. K. Bhattacharjee, N. Kutkut, and I. Batarseh, "Review of multiport converters for solar and energy storage integration," *IEEE Transactions on Power Electronics*, vol. 34, no. 2, pp. 1431–1445, 2019.

[34] V. N. S. R. Jakka, A. Shukla, and G. D. Demetriades, "Dual-transformer-based asymmetrical triple-port active bridge (dt-atab) isolated dcdc converter," *IEEE Transactions on Industrial Electronics*, vol. 64, no. 6, pp. 4549–4560, June. 2017.

[35] H. Zhu, D. Zhang, H. S. Athab, B. Wu, and Y. Gu, "Pv isolated three-port converter and energy-balancing control method for pv-battery power supply applications," *IEEE Transactions on Industrial Electronics*, vol. 62, no. 6, pp. 3595–3606, June. 2015.

[36] J. Zhang, W. Jiang, T. Jiang, S. Shao, Y. Sun, B. Hu, and J. Zhang, "A three-port llc resonant dc/dc converter," *IEEE Journal of Emerging and Selected Topics in Power Electronics*, vol. 7, no. 4, pp. 2513–2524, Dec. 2019.

[37] Y. Sato, M. Uno, and H. Nagata, "Nonisolated multiport converters based on integration of pwm converter and phase-shift-switched capacitor converter," *IEEE Transactions on Power Electronics*, vol. 35, no. 1, pp. 455–470, Jan. 2020.

[38] B. Chandrasekar, C. Nallaperumal, S. Padmanaban, M. S. Bhaskar, J. B. Holm-Nielsen, Z. Leonowicz, and S. O. Masebinu, "Non-isolated high-gain triple port dcdc buck-boost converter with positive output voltage for photovoltaic applications," *IEEE Access*, vol. 8, pp. 113649–113666, 2020.

[39] M. Sagar Bhaskar, V. K. Ramachandaramurthy, S. Padmanaban, F. Blaabjerg, D. M. Ionel, M. Mitolo, and D. Almakhles, "Survey of dc-dc non-isolated topologies for unidirectional power flow in fuel cell vehicles," *IEEE Access*, vol. 8, pp. 178130–178166, 2020.

[40] D. Liu and H. Li, "A zvs bi-directional dcdc converter for multiple energy storage elements," *IEEE Transactions on Power Electronics*, vol. 21, no. 5, pp. 1513–1517, Sept. 2006.

[41] C. Zhao, S. D. Round, and J. W. Kolar, "An isolated three-port bidirectional dc/dc converter with decoupled power flow management," *IEEE Transactions on Power Electronics*, vol. 23, no. 5, pp. 2443–2453, Sept. 2008.

[42] A. Alhatlani and I. Batarseh, "Review of partially isolated three-port converters for pv-battery systems that interface a pv, bidirectional battery, and load," in *IEEE Conference on Power Electronics and Renewable Energy (CPERE)*, pp. 465–472, 2019.

[43] W. Hu, H. Wu, Y. Xing, and K. Sun, "A full-bridge three-port converter for renewable energy application," in *IEEE Applied Power Electronics Conference and Exposition - APEC 2014*, pp. 57–62, 2014.

[44] M. C. Mira, Z. Zhang, A. Knott, and M. A. E. Andersen, "Analysis, design, modeling, and control of an interleaved-boost full-bridge three-port converter for hybrid renewable energy systems," *IEEE Transactions on Power Electronics*, vol. 32, no. 2, pp. 1138–1155, Feb. 2017.

[45] H. Wu, K. Sun, L. Zhu, and Y. Xing, "An interleaved half-bridge three-port converter with enhanced power transfer capability using three-leg rectifier for renewable energy applications," *IEEE Journal of Emerging and Selected Topics in Power Electronics*, vol. 4, no. 2, pp. 606–616, June. 2016.

[46] M. Uno, R. Oyama, and K. Sugiyama, "Partially isolated single-magnetic multiport converter based on integration of series-resonant converter and bidirectional pwm converter," *IEEE Transactions on Power Electronics*, vol. 33, no. 11, pp. 9575–9587, Nov. 2018.

[47] T.-J. Liang and K. Tseng, "Analysis of integrated boost-flyback step-up converter," *IEE Proceedings-Electric Power Applications*, vol. 152, no. 2, pp. 217–225, 2005.

[48] R. Faraji, E. Adib, and H. Farzanehfard, "Soft-switched non-isolated high step-up multi-port dc-dc converter for hybrid energy system with minimum number of switches," *International Journal of Electrical Power & Energy Systems*, vol. 106, pp. 511–519, 2019.

[49] D. D.-C. Lu and V. G. Agelidis, "Photovoltaic-battery-powered dc bus system for common portable electronic devices," *IEEE Transactions on Power Electronics*, vol. 24, no. 3, pp. 849–855, 2009.

[50] H. Wu, K. Sun, S. Ding, and Y. Xing, "Topology derivation of nonisolated three-port dc–dc converters from dic and doc," *IEEE Transactions on Power Electronics*, vol. 28, no. 7, pp. 3297–3307, 2013.

[51] G. Wen, Y. Chen, and Y. Kang, "A family of cost-efficient integrated single-switch three-port converters," in *Applied Power Electronics Conference and Exposition (APEC), 2013 Twenty-Eighth Annual IEEE*, pp. 1062–1067, IEEE, 2013.

[52] L. Chien, C. Chen, J. Chen, and Y. Hsieh, "Novel three-port converter with high-voltage gain," *IEEE Transactions on Power Electronics*, vol. 29, no. 9, pp. 4693–4703, Sept. 2014.

[53] F. Kardan, R. Alizadeh, and M. R. Banaei, "A new three input dc/dc converter for hybrid pv/fc/battery applications," *IEEE Journal of Emerging and Selected Topics in Power Electronics*, vol. 5, no. 4, pp. 1771–1778, 2017.

[54] P. Zhang, Y. Chen, and Y. Kang, "Nonisolated wide operation range three-port converters with variable structures," *IEEE Journal of Emerging and Selected Topics in Power Electronics*, vol. 5, no. 2, pp. 854–869, 2017.

[55] M. R. Al-Soeidat, H. Aljarajreh, H. A. Khawaldeh, D. D. C. Lu, and J. Zhu, "A reconfigurable three-port dcdc converter for integrated pv-battery system," *IEEE Journal of Emerging and Selected Topics in Power Electronics*, vol. 8, no. 4, pp. 3423–3433, Dec. 2020.

[56] T. Cheng and D. D.-C. Lu, "Three-port converters with a flexible power flow for integrating pv and energy storage into a dc bus," *Journal of Power Electronics*, vol. 17, no. 6, pp. 1433–1444, Jun. 2017.

[57] T. Cheng, D. D.-C. Lu, and L. Qin, "Non-isolated single-inductor dc/dc converter with fully reconfigurable structure for renewable energy applications," *IEEE Transactions on Circuits and Systems II: Express Briefs*, vol. 65, no. 3, pp. 351–355, 2018.

[58] H. Zhu, D. Zhang, Q. Liu, and Z. Zhou, "Three-port dc/dc converter with all ports current ripple cancellation using integrated magnetic technique," *IEEE Trans. Power Electron.*, vol. 31, no. 3, pp. 2174–2186, 2016.

[59] A. Ganjavi, H. Ghoreishy, A. A. Ahmad, and Z. Zhagn, "A three-level three-port bidirectional dc/dc converter," in *2018 IEEE International Power Electronics and Application Conference and Exposition (PEAC)*, pp. 1–4, IEEE, 2018.

[60] S. Gao, J. Shi, X. Dong, Y. Jia, H. Wu, and H. Hu, "Performance evaluation of a non-isolated three-port converter for pv-battery hybrid energy system," in *IECON 2018-44th Annual Conference of the IEEE Industrial Electronics Society*, pp. 1394–1399, IEEE, 2018.

[61] S. Wen, S. Wang, G. Liu, and R. Liu, "Energy management and coordinated control strategy of pv/hess ac microgrid during islanded operation," *IEEE Access*, vol. 7, pp. 4432–4441, 2019.

[62] P. Yang, C. K. Tse, J. Xu, and G. Zhou, "Synthesis and analysis of double-input single-output dc/dc converters," *IEEE Transactions on Industrial Electronics*, vol. 62, no. 10, pp. 6284–6295, Oct. 2015.

[63] Z. Wang, Q. Luo, Y. Wei, D. Mou, X. Lu, and P. Sun, "Topology analysis and review of three-port dcdc converters," *IEEE Transactions on Power Electronics*, vol. 35, no. 11, pp. 11783–11800, Nov. 2020.

[64] C. G. Zogogianni, E. C. Tatakis, and M. S. Vekic, "Non-isolated reduced redundant power processing dc/dc converters: A systematic study of topologies with wide voltage ratio for high-power applications," *IEEE Transactions on Power Electronics*, vol. 34, no. 9, pp. 8491–8502, Sep. 2019.

[65] C. K. Tse, M. H. Chow, and M. K. Cheung, "A family of pfc voltage regulator configurations with reduced redundant power processing," *IEEE Transactions on Power Electronics*, vol. 16, no. 6, pp. 794–802, 2001.

[66] C. K. Tse, "Circuit theory of power factor correction in switching converters," *International journal of circuit theory and applications*, vol. 31, no. 2, pp. 157–198, 2003.

[67] C. G. Zogogianni, E. C. Tatakis, and M. S. Vekic, "Non-isolated reduced redundant power processing dc/dc converters: A systematic study of topologies with wide voltage ratio for high-power applications," *IEEE Transactions on Power Electronics*, vol. 34, no. 9, pp. 8491–8502, Sept, 2019.

[68] M. Waseem, L. Saeed, M. Y. A. Khan, J. Saleem, and A. Majid, "A multi input multi output bidirectional dc/dc boost converter with backup battery port," in *2018 1st International Conference on Power, Energy and Smart Grid (ICPESG)*, pp. 1–6, IEEE, 2018.

[69] H. Moradisizkoohi, N. Elsayad, and O. A. Mohammed, "A family of three-port three-level converter based on asymmetrical bidirectional half-bridge topology

for fuel cell electric vehicle applications," *IEEE Transactions on Power Electronics*, vol. 34, no. 12, pp. 11706–11724, Dec. 2019.

[70] M. Al-Soeidat, H. Khawaldeh, D. D. . Lu, and J. Zhu, "A novel high step-up three-port bidirectional dc/dc converter for pv-battery integrated system," in *2020 IEEE Applied Power Electronics Conference and Exposition (APEC)*, pp. 3352–3357, 2020.

[71] B. Zhang, P. Wang, T. Bei, X. Li, Y. Che, and G. Wang, "Novel topology and control of a non-isolated three port dc/dc converter for pv-battery power system," in *2017 20th International Conference on Electrical Machines and Systems (ICEMS)*, pp. 1–6, IEEE, 2017.

[72] T. Cheng, D. D. Lu, and L. Qin, "Non-isolated single-inductor dc/dc converter with fully reconfigurable structure for renewable energy applications," *IEEE Transactions on Circuits and Systems II: Express Briefs*, vol. 65, no. 3, pp. 351–355, 2018.

[73] Q. Wang, D. Zha, M. Cheng, F. Deng, and G. Buja, "Energy management system for dc electric spring with parallel topology," *IEEE Transactions on Industry Applications*, vol. 56, no. 5, pp. 5385–5395, Oct. 2020.

[74] I. Askarian, M. Pahlevani, and A. M. Knight, "Three-port bidirectional dc/dc converter for dc nanogrids," *IEEE Transactions on Power Electronics*, vol. 36, no. 7, pp. 8000–8011, 2021.

[75] Y. Wu and I. Chen, "Novel integrated three-port bidirectional dc/dc converter for energy storage system," *IEEE Access*, vol. 7, pp. 104601–104612, July. 2019.

[76] D. Debnath and K. Chatterjee, "Two-stage solar photovoltaic-based standalone scheme having battery as energy storage element for rural deployment," *IEEE Transactions on Industrial Electronics*, vol. 62, no. 7, pp. 4148–4157, Jul. 2015.

[77] J. Hong, J. Yin, Y. Liu, J. Peng, and H. Jiang, "Energy management and control strategy of photovoltaic/battery hybrid distributed power generation systems with an integrated three-port power converter," *IEEE Access*, vol. 7, pp. 82838–82847, Jun. 2019.

[78] V. Monteiro, J. G. Pinto, and J. L. Afonso, "Experimental validation of a three-port integrated topology to interface electric vehicles and renewables with the electrical grid," *IEEE Transactions on Industrial Informatics*, vol. 14, no. 6, pp. 2364–2374, Jun. 2018.

[79] H. Khoramikia, M. Heydari, and S. M. Dehghan, "A new three-port non-isolated dc/dc converter for renewable energy sources application," in *Electrical Engineering (ICEE), Iranian Conference on*, pp. 1101–1106, IEEE, 2018.

[80] S. Bhattacharya and S. Samanta, "A novel non-isolated three port dc/dc converter for photovoltaic applications," in *2020 IEEE International Conference on Power Electronics, Smart Grid and Renewable Energy (PESGRE2020)*, pp. 1–6, IEEE, 2020.

[81] X. Qi, D. Zhang, X. Pan, and M. Fang, "A coupled inductors based high gain non-isolated three-port dc/dc converter," in *2018 IEEE International Power Electronics and Application Conference and Exposition (PEAC)*, pp. 1–6, IEEE, 2018.

[82] N. Zahedi, S. Salehi, and S. H. Hosseini, "Non-isolated three port dc/dc converter with soft switching technique," in *2019 10th International Power Electronics, Drive Systems and Technologies Conference (PEDSTC)*, pp. 401–406, IEEE, 2019.

[83] R. Faraji, H. Farzanehfard, M. Esteki, and S. A. Khajehoddin, "A lossless passive snubber circuit for three-port dc–dc converter," *IEEE Journal of Emerging and Selected Topics in Power Electronics*, vol. 9, no. 2, pp. 1905–1914, Aug 2020.

[84] R. Cheraghi, E. Adib, and M. S. Golsorkhi, "A non-isolated high step-up three-port soft-switched converter with minimum switches," *IEEE Transactions on Industrial Electronics*, pp. 1–1, Sep. 2020.

[85] B. Honarjoo, S. M. Madani, M. Niroomand, and E. Adib, "Non-isolated high step-up three-port converter with single magnetic element for photovoltaic systems," *IET Power Electronics*, vol. 11, no. 13, pp. 2151–2160, Jun. 2018.

[86] L. Chien, C. Chen, J. Chen, and Y. Hsieh, "Novel three-port converter with high-voltage gain," *IEEE Transactions on Power Electronics*, vol. 29, no. 9, pp. 4693–4703, 2014.

[87] J. Deng, H. Wang, and M. Shang, "A zvs three-port dc/dc converter for high-voltage bus-based photovoltaic systems," *IEEE Transactions on Power Electronics*, vol. 34, no. 11, pp. 10688–10699, 2019.

[88] H. Wu, K. Sun, S. Ding, and Y. Xing, "Topology derivation of nonisolated three-port dcdc converters from dic and doc," *IEEE Transactions on Power Electronics*, vol. 28, no. 7, pp. 3297–3307, 2013.

[89] X. Hong, J. Wu, and C. Wei, "98.1%-efficiency hysteretic-current-mode non-inverting buck-boost dc/dc converter with smooth mode transition," *IEEE Transactions on Power Electronics*, vol. 32, no. 3, pp. 2008–2017, Mar. 2017.

[90] M. M. Garg, Y. V. Hote, M. K. Pathak, and L. Behera, "An approach for buck converter pi controller design using stability boundary locus," in *2018 IEEE/PES Transmission and Distribution Conference and Exposition (T D)*, pp. 1–5, 2018.

[91] Q. Xu, C. Zhang, C. Wen, and P. Wang, "A novel composite nonlinear controller for stabilization of constant power load in dc microgrid," *IEEE Transactions on Smart Grid*, vol. 10, no. 1, pp. 752–761, 2019.

[92] X. Li, L. Guo, S. Zhang, C. Wang, Y. W. Li, A. Chen, and Y. Feng, "Observer-based dc voltage droop and current feed-forward control of a dc microgrid," *IEEE Transactions on Smart Grid*, vol. 9, no. 5, pp. 5207–5216, 2018.

[93] Y. Gui, R. Han, J. M. Guerrero, J. C. Vasquez, B. Wei, and W. Kim, "Large-signal stability improvement of dc/dc converters in dc microgrid," *IEEE Transactions on Energy Conversion*, pp. 1–1, 2021.

[94] X. Chen, P. Yang, and Y. Peng, "Synthesis and analysis of power management units for iot applications," in *2020 15th IEEE Conference on Industrial Electronics and Applications (ICIEA)*, pp. 1383–1388, Sept, 2020.

[95] G. Chen, Z. Jin, Y. Liu, Y. Hu, J. Zhang, and X. Qing, "Programmable topology derivation and analysis of integrated three-port dcdc converters with reduced switches for low-cost applications," *IEEE Transactions on Industrial Electronics*, vol. 66, no. 9, pp. 6649–6660, 2019.

[96] H. Zhu, D. Zhang, B. Zhang, and Z. Zhou, "A nonisolated three-port dcdc converter and three-domain control method for pv-battery power systems," *IEEE Transactions on Industrial Electronics*, vol. 62, no. 8, pp. 4937–4947, Aug 2015.

[97] B. Wang, L. Xian, V. R. K. Kanamarlapudi, K. J. Tseng, A. Ukil, and H. B. Gooi, "A digital method of power-sharing and cross-regulation suppression for single-inductor multiple-input multiple-output dcdc converter," *IEEE Transactions on Industrial Electronics*, vol. 64, no. 4, pp. 2836–2847, April 2017.

[98] B. Wang, X. Zhang, J. Ye, and H. B. Gooi, "Deadbeat control for a single-inductor multiple-input multiple-output dcdc converter," *IEEE Transactions on Power Electronics*, vol. 34, no. 2, pp. 1914–1924, Feb 2019.

[99] P. Tseng, J. Chen, T. Liang, and H. Liang, "A novel high step-up three-port converter," in *2014 International Power Electronics and Application Conference and Exposition*, pp. 21–25, 2014.

[100] S. S. Dobakhshari, S. H. Fathi, and J. Milimonfared, "A new soft-switched three-port dc/dc converter with high voltage gain and reduced number of semiconductors for hybrid energy applications," *IEEE Transactions on Power Electronics*, vol. 35, no. 4, pp. 3590–3600, April. 2020.

[101] G. Zhou, Q. Tian, and L. Wang, "Soft-switching high gain three-port converter based on coupled inductor for renewable energy system applications," *IEEE Transactions on Industrial Electronics*, pp. 1–1, 2021.

[102] T. Cheng, D. D. Lu, and L. Qin, "Non-isolated single-inductor dc/dc converter with fully reconfigurable structure for renewable energy applications," *IEEE Transactions on Circuits and Systems II: Express Briefs*, vol. 65, no. 3, pp. 351–355, Mar. 2018.

[103] H. Aljarajreh, D. D.-C. Lu, Y. P. Siwakoti, R. P. Aguilera, and C. K. Tse, "A method of seamless transitions between different operating modes for three-port dc/dc converters," *IEEE Access*, vol. 9, pp. 59184–59195, 2021.